# ANNEALING AND DEVICE CHARACTERIZATION OF HGCDTE GROWN ON CDTE/SI SUBSTRATES

by

Sina Simingalam
A Dissertation
Submitted to the
Graduate Faculty
of
George Mason University
in Partial Fulfillment of
The Requirements for the Degree
of
Doctor of Philosophy
Physics

Committee:

| | |
|---|---|
| ___________________________ | Dr. Rao V. Mulpuri, Dissertation Director |
| ___________________________ | Dr. Yuri Mishin, Committee Member |
| ___________________________ | Dr. Estela Blaisten-Barojas, Committee Member |
| ___________________________ | Dr. John A. Schreifels, Committee Member |
| ___________________________ | Dr. Maria Dworzecka, Acting Department Chair |
| ___________________________ | Dr. Donna M. Fox, Associate Dean, Office of Student Affairs & Special Programs, College of Science |
| ___________________________ | Dr. Peggy Agouris, Dean, College of Science |
| Date: ______________________ | Fall Semester 2015<br>George Mason University<br>Fairfax, VA |

Annealing And Device Characterization Of Hgcdte Grown On Cdte/Si Substrates

A dissertation submitted in partial fulfillment of the requirements for the degree of Doctor of Philosophy at George Mason University

By

Sina Simingalam
Master of Science
George Mason University, 2012
Bachelor of Science
George Mason University, 2010

Director: Rao V. Mulpuri, Professor
Department of Electrical and Computer Engineering

Fall Semester 2015
George Mason University
Fairfax, VA

Copyright: 2015 Sina Simingalam
All Rights Reserved

Dedication

I would like to dedicate this dissertation to my parents, Alireza Simingalamavval and Tahereh Sedghizadeh, and my fiancé, Veronique Alexis Loren Bonhomme, for their patience and support throughout the past several years. Thank you. I love you all.

## Acknowledgements

I would like to acknowledge and thank all of those who helped me through this process. To my advisor, Dr. Mulpuri, for all of his support and the many late nights, working on papers and my dissertation. It is because of his detailed review that my work made it as far as it did. I would like to thank my other committee members, Dr. Mishin, Dr. Blaisten-Barojas, and Dr. Schreifels for their help and comments.

I would also like to thank all of the people at the U.S. Army Research Laboratory for their help with my research. I'd like to thank the entire II-VI Materials and Devices team under the Sensors and Electron Devices Directorate as a whole for the countless discussions in meetings running hours beyond their set time. I'd like to thank Dr. Wijewarnasuriya for helping point my research efforts in the right direction. I'd like to thank Dr. DeCuir for his honest review and feedback on my work. I've become a much better presenter due to his feedback (although I still have a way to go). I'd like to thank Greg Meissner and Kim Olver for their assistance in processing. I'd like to thank Dr. VanMil and Dr. Doyle for their assistance in material growth and characterization.

I would like to thank the U.S. Army Research Office (ARO) who supported my work at George Mason University under grant no. W911NF-11-2-0049.

Without the support of all these people, this work would have never been possible.

Table of Contents

Page
List of Tables ........ vii
List of Figures ........ viii
Abstract ........ xi
Chapter 1. Introduction ........ 1
Chapter 2. Background ........ 7
2. 2. Point Defects ........ 8
2. 3. Dislocation Types ........ 10
2. 4. Dislocation Motion ........ 14
2. 5. Dislocation Forces ........ 16
2. 6. Dislocation Strain, Stresses, and Energy ........ 19
Chapter 3. Thermal Cycle Annealing ........ 25
3. 1. TCA: Theory ........ 25
3. 2. TCA: Experiment ........ 28
3. 3. TCA: Results & Discussion ........ 32
3. 4. TCA: Conclusion of Planar TCA Experiment ........ 42
Chapter 4. Etched Mesa Structures ........ 44
4. 1. Mesa: Theory ........ 46
4. 2. Mesa: Experiment ........ 49
4. 3. Mesa: Results and Analysis ........ 50
4. 4. Mesa: Conclusion ........ 60
Chapter 5. Devices ........ 61
5. 1. Devices: Theoretical Background ........ 61
5.1.1. Generation-Recombination Current ........ 67
5.1.2. Shunt Current ........ 69

5.1.3. Tunneling ........ 70
5. 2. Devices: Modeling ........ 72
5. 3. Devices: Experiment ........ 77
5. 4. Devices: Results ........ 79
5. 5. Devices: Effect of TCA ........ 90
5. 6. Comparison to the Competition ........ 92
5. 7. Application of Mesa Architecture ........ 97
5. 8. Device: Conclusion ........ 101
Chapter 6. Conclusion & Future Work ........ 102
List of References ........ 104
Biography ........ 108

List of Tables

Table Page

Table 1. Lattice constants of layers from substrate to absorber material [3]. .................... 2
Table 2. Critical thickness determination from numerical analysis [3] ........................... 14
Table 3. Anneal Conditions. vac refers to vacancy anneal with Hg held at 30°C below sample and iso refers to isothermal anneal. ...................................................................... 42
Table 4. Device material characteristics ........................................................................... 81

List of Figures

Figure Page

Figure 1. Variation in EPD versus number of cycles at 494°C. Total time at high temperature for all tests is 20 minutes [7]. 5
Figure 2. Simple cubic unit cell. 7
Figure 3. FCC unit cell. 7
Figure 4. Zincblende unit cell. Red atoms are metal atoms and blue are non-metal atoms. If all atoms are the same, then this is a diamond lattice. 8
Figure 5. First principles calculation of native defect densities in MCT [10]. 10
Figure 6. Native vacancy concentration annealed under various Hg partial pressures [11]. 10
Figure 7. Dislocations in the simple cubic lattice with their respective burgers vectors, b, edge dislocation (top), and screw dislocation (bottom). [12] 12
Figure 8. Graphics displaying a) glide motion and b) climb motion of edge dislocations. The dislocation is represented by the symbol "⊥". 15
Figure 9. Dislocation density for various anneal schedules and cycles. 28
Figure 10. Quartz ampoule showing sample positions and Hg placement. 30
Figure 11. Graphite tube setup as placed inside furnace. 30
Figure 12. Restults of annealing with 32 2-minute cycles and the various high temperatures. 33
Figure 13. TCA with varied number of cycles between 350°C and 250°C. 33
Figure 14. SIMS profile of the as-grown structures and two different anneal schedules. 35
Figure 15. EPD vs. number of cycles comparing thin and thick samples 36
Figure 16. Structure of sample with a) EPD vs Depth showing the impact of interfaces and, b) the full layer structure from the substrate. 37
Figure 17. One minute cycle calibration 40
Figure 18. Expected saturation overpressure based on cold point temperature and saturation pressure for sample temperature. 40
Figure 19. Area of interaction for a dislocation travelling in the [0-11] direction. 48
Figure 20. Dislocation density with variation in long bar mesa orientation. 4 cyc refers to 4 5-minute cycles at the high temperature. "Deep" refers to 8 μm etch depth. 51

Figure 21. Figures representing dislocations with arrows giving direction of travel. a) Planar dislocation interactions with type $\boldsymbol{\alpha}$ and $\boldsymbol{\beta}$ dislocations. b) Mesa being defined and cutting the dislocation line. c) Dislocation motion after mesa is etched. ......................... 54
Figure 22. 20 µm long bar mesa EPD variation with angle away from [0-11] orientation ........................................................................................................................ 55
Figure 23. Variation in EPD with mesa thickness. Mesa oriented along [0-11] direction. ........................................................................................................................ 55
Figure 24. Effect of TCA with various conditions. ....................................................... 57
Figure 25. Mesa structure showing bins for dislocation categorizing ............................. 58
Figure 26. 45 degree angled view of sidewall of 25um mesa along [0-11] orientation. Right shows a cross-section with the field of view of the picture. .................................. 58
Figure 27. Dislocation density along sidewall for various angles from [0-11] orientation of 20 µm wide mesa structures. ........................................................................... 59
Figure 28. Dislocation density along sidewall of [0-11] long bar mesa structures with varying widths.............................................................................................................. 59
Figure 29. Diode formed by joining a p-type and n-type semiconductors. The depletion width is shown as represented by W. ........................................................................ 63
Figure 30. Shockley-Read, Auger, and Radiative recombination methods. ..................... 65
Figure 31. Diode cross section showing the methods of shunt curren path through devices ........................................................................................................................ 70
Figure 32. Tunneling current mechanisms displaying band-to-band and trap-assisted tunneling. ....................................................................................................................... 71
Figure 33. As Grown Device Structure. Growth Height of 0 corresponds to substrate surface. .......................................................................................................................... 73
Figure 34. Junction location. Blue vertical line shows center of depletion width. Red line represents device structure. Horizontal blue line is the indium doping level. Green line is the arsenic doping profile.................................................................................. 74
Figure 35. Device Cross Section.................................................................................... 74
Figure 36. Quantum efficiency as a function of thickness.............................................. 75
Figure 37. QE vs absorber layer thickness...................................................................... 76
Figure 38. Variation in QE with doping density............................................................ 77
Figure 39. Current-Voltage measurements of various diameter circular diodes on MC0074 ........................................................................................................................ 80
Figure 40. Impedance area-Voltage measurements of various diameter circular diodes on MC0074 ........................................................................................................................ 80
Figure 41. Modeling of current components of 250µm diameter diode .......................... 81
Figure 42. Modeling of current components of 80µm diameter diode ............................ 82
Figure 43. Modeling of current components of 20µm diameter diode ............................ 82

Figure 44. Dark current variation with time heated at 80°C. Minimum achieved at 108 minutes with factor of ~2 reduction. ........ 84
Figure 45. Perimeter over Area plot of dark current density at -0.2V and room temperature to determine shunt current contribution. ........ 84
Figure 46. $\boldsymbol{\eta}$ vs. $1/R_j$ to determine $\eta_{1D}$ and collection length, $L_c$. ........ 85
Figure 47. Device cross section displaying the influence of collection length on the active device volume. ........ 86
Figure 48. QE and Responsivity for 250μm diode ........ 87
Figure 49. Zero-bias resistance-junction area product of various diameter circular diodes on MC0074 ........ 88
Figure 50. Zero-bias resistance-optical area product of various diameter circular diodes on MC0074 ........ 89
Figure 51. Dark current with representative theoretical currents of Diffusion with and without SRH affecting lifetime ........ 89
Figure 52. Dark Current Density vs. temperature for MC86, SWIR MCT layer subjected to TCA processing. Models are shown with their respective minority carrier lifetimes. . 91
Figure 53. RoA measurements vs device diameter of MCT devices subjected to TCA. . 92
Figure 54. 1mm InGaAs diode dark current vs. temperature ........ 95
Figure 55. Activation energy for 1mm InGaAs diode above and below 200K ........ 95
Figure 56. Comparison of extended InGaAs and MCT SWIR device QE and Responsivity ........ 96
Figure 57. Left) Device structure of mesa devices. Right) Zoomed in image of mesa diode ........ 98
Figure 59. Dark current density comparison of mesa and planar devices under 100mV reverse bias conditions. ........ 99
Figure 58. Dark currents of planar (top) and mesa (bottom) devices at varying temperatures. ........ 100

Abstract

ANNEALING AND DEVICE CHARACTERIZATION OF HGCDTE GROWN ON CDTE/SI SUBSTRATES

Sina Simingalam, PhD

George Mason University, 2015

Dissertation Director: Dr. Rao V. Mulpuri

Infrared sensors have long been utilized for personal, commercial, and government applications. Mercury cadmium telluride (MCT) is the highest quality material for infrared detection. Its limitation comes in the substrate that it is grown on. Cadmium zinc telluride (CZT) is the substrate of choice for its ability to be lattice matched to the MCT epilayer grown on it, but its limited size of less than 7x7 $cm^2$ and high cost of \$200 $cm^{-2}$ has led to a push for alternative substrates. Silicon has been utilized as a potential alternative substrate due to its cost of less than \$1 $cm^{-2}$ and size of greater than 8" in diameter. However, it has a lattice mismatch of 19% with MCT, leading to an as-grown dislocation density of $1x10^7$ $cm^{-2}$ in the MCT epilayer. This is more than two orders of magnitude greater than the dislocation density of $1x10^5$ $cm^{-2}$ for MCT grown on CZT. The work presented in this dissertation looks at various ways of reducing the dislocation density and its impact on devices.

Thermal cycle annealing (TCA) is the heating and cooling of a sample over a specified period of time. TCA has been applied to MCT in the past, but has had limited application due to interdiffusion of the as-grown layer structures. This was due to the high annealing temperature of 500°C and four cycles of 5 minutes at the high temperature. A new annealing setup has been made that allows dislocation reduction at high annealing temperatures as low as 350°C and 128 cycles of less than 5 seconds each at the high temperature. This results in a dislocation density reduction to $1 \times 10^6$ $cm^{-2}$ with minimal diffusion for MCT grown on silicon-based substrates. Conducting 512 cycles at a high annealing temperature of 400°C did not result in further dislocation density reduction. This pushed the focus of the work onto other methods of dislocation reduction.

To reduce the dislocation density further, etched mesa bar structures have been utilized to enhance dislocation reduction during thermal annealing. The dislocation density of mesa structures was studied for their dependence on anneal time, temperature, and etch depth. It was found that a single, 5-minute thermal anneal at 400°C can induce dislocation reduction with a dependence on mesa bar angle relative to the $[0\bar{1}1]$ orientation. It is also found that dislocation density reduction is proportional to etched mesa bar width. A minimum dislocation density of $1 \times 10^5$ $cm^{-2}$ is observed with a 10 μm wide mesa bar, which is on par with the dislocation density of MCT grown on CZT. With this result, the etched mesa bar structure is applied to device layers and devices are fabricated and tested. The dark current density of devices on mesa bars is lower than that of planar devices. Therefore, the application of these results to large arrays can bridge the gap in device performance between MCT grown on CZT and MCT grown on CdTe/Si.

# Chapter 1. Introduction

Sensors have long been utilized in applications for personal, commercial, and governmental uses like cameras on phones and security systems. Infrared sensors are of particular interest to several different markets, especially for defense and security applications. Infrared applications include allowing the detection of rocket or jet flame plumes and the ability to observe thermal sources through walls or in complete visible darkness. The ability to maintain an advantage with regard to infrared sensor performance is a critical need for the military.

Different types of sensors are available and are classified by their group in the periodic table, which denotes the number of valence electrons. There are several options for infrared detectors including group IV devices like silicon, III-V devices like InGaAs, and II-VI devices like $Hg_{1-x}Cd_xTe$ (MCT). There are several wavebands of interest for ground-based sensors due to their atmospheric transparency, which include the visible (0.4-0.7 μm), near-infrared(NIR, 0.7-1.1 μm), short-wavelength infrared (SWIR, 1.0-2.5 μm), mid-wavelength infrared (MWIR, 3-5 μm), long-wavelength infrared (LWIR, 8-14 μm) and very-long-wavelength infrared (VLWIR, >15 μm) wavebands. Due to its tunability between 1 and 30 μm wavelength cutoff, small variation in lattice constant with

composition, high electron mobility, long minority carrier lifetime and well researched diode formation technology, MCT is a dominant material for infrared detection [1].

$Cd_{1-x}Zn_xTe$ (CZT) with a (211) crystallographic surface orientation is the optimal substrate of choice for MCT growth by molecular beam epitaxy (MBE) for its ability to match the lattice constant of MCT [2]. The high cost of \$200 $cm^{-2}$, limited size of 7x7 $cm^2$ and thermal expansion coefficient mismatch between CZT and silicon read out integrated circuit (ROIC) are significant drawbacks that have pushed the search for alternative substrates. Because of its lattice and thermal expansion coefficient match to the ROIC, its low cost of <\$1 $cm^{-2}$ and large format size of greater than 8" diameter wafers, silicon is the alternative substrate of choice in MCT growth [3]. But, this doesn't come without issues. Silicon has a 19% lattice mismatch between MCT and silicon. The lattice constant of all the materials of interest in this work are shown in Table 1. This mismatch causes the presence of misfit dislocations to relieve lattice mismatch strain. Typically, an 8-10 μm thick CdTe buffer layer is grown between MCT and silicon to allow dislocations to annihilate in the CdTe layer without significantly affecting the main MCT device structure [4].

Table 1. Lattice constants of layers from substrate to absorber material **[3]**.

| Material | Lattice Constant (Å) |
|---|---|
| Silicon | 5.14 |
| ZnTe | 6.101 |
| CdTe | 6.484 |
| $Hg_{1-x}Cd_xTe$ | 6.4615+0.01998x |

Dislocations have a significant impact on device properties. The sensor diode is formed by joining electron-rich (n-type) and hole-rich (p-type) pieces of MCT material, which causes current to freely flow from p- to n-type regions under forward bias, but greatly limits current from n- to p-type material under reverse bias. Dislocations can provide shunt paths and generation-recombination centers within the bandgap. Shunt paths are low resistance pathways for current transport. Generation-recombination centers are semi-stable positions within the bandgap that can cause extended charge carrier lifetimes and degraded device performance. the two important characteristics of the device are the dark current density, $J_d$, and quantum efficiency, $\eta$. $J_d$ is the current density of a photovoltaic sensor under no illumination. Increased $J_d$ leads to increased noise in the sensor therefore degrading performance and requiring greater cooling to maintain sensitivity. Quantum efficiency is the number of electron-hole pairs generated per photon incident on the sample. Greater quantum efficiency allows for better signal to noise ratio [5]. The effect of dislocations on device function will be discussed in later chapters.

Thermal cycle annealing (TCA) has been employed to lower the density of dislocations and has achieved a minimum density of $1 \times 10^6$ $cm^{-2}$ in MCT [6]. The procedure involves isothermal, radiative annealing of MCT grown on CdTe/Si substrates in an evacuated, sealed ampoule. In this procedure, for one anneal cycle, the ampoule is heated to a temperature of 500°C over 5 minutes, held for 5 minutes, then radiatively cooled to 250°C over 20 minutes. The application of this TCA method to devices is severely limited due to its use of a high temperature of 500°C and long time at this high temperature. This causes significant interdiffusion of constituent components in the as-grown layer and

from the CdTe/Si substrate. A typical high temperature anneal for device processing, known as a p-type activation anneal, is between 10 and 20 minutes at 400°C. This creates a serious limitation to the use of TCA for dislocation reduction as maintaining sharp interfaces is necessary for specific device designs and an advantage of growth by MBE. Without sharp interfaces, the benefit of using MBE decreases and the device performance suffers.

Further work has shown that certain characteristics are more important than others during cycle annealing. Farrell, et. al. showed that the number of cycles was the critical variable for reducing dislocations, not the time spent at temperature, as shown in Figure 1. A comparison of 2 minute versus 5 minute high temperature anneal times confirmed that the difference in final dislocation density was similar for both annealing durations.With the total anneal time kept the same, the samples had decreasing dislocation densities with increasing number of cycles. In another experiment, 1, 2, 4, 8, 16 and 32 cycles of 5-minute high temperature anneals were conducted and achieved negligible reduction after 4 cycles. Farrell, et. al, postulated that the dislocation density does not reduce below this minimum dislocation density of $1x10^6$ $cm^{-2}$ due to the formation of immobile, sessile dislocations after dislocation-dislocation interaction. [6].

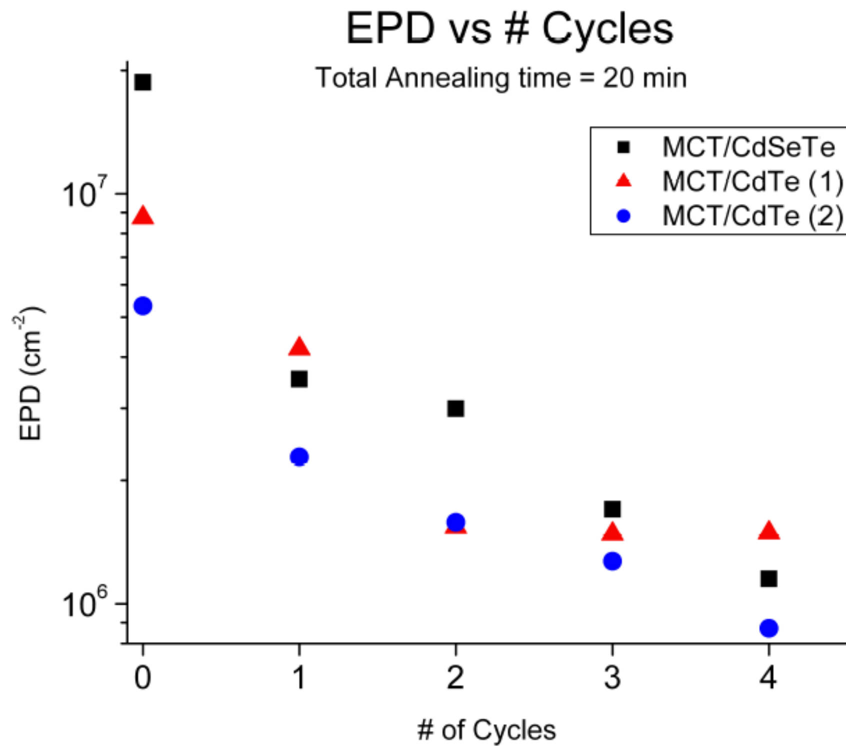


Figure 1. Variation in EPD versus number of cycles at 494°C. Total time at high temperature for all tests is 20 minutes **[7]**.

Another aspect of annealing comes in the analysis of etching mesa structures into MCT and the dislocation reduction observed after annealing in these structures. Stoltz, et. al. had shown dislocation reduction in samples etched down to their substrate and subjected to 4 5-minute cycles between 500°C and 250°C. They were able to achieve dislocation reduction below the planar saturation limit to mid-$10^5$ $cm^{-2}$ in 25 μm wide, long bar mesa structures oriented along the [0-11] direction. Stoltz, et. al. postulated that image forces induced glide along certain orientations forcing dislocations with [-111] orientations to the

sidewall and [0-11] dislocations away from the sidewalls, but did not have any further analysis to support this [8]. This technique of etching mesa structures can prove to be very significant with growth on lattice mismatched substrates.

There are several problems that remain due to gaps in knowledge, including designing a TCA scheme that minimizes dislocation density while also minimizing inter-diffusion of Cd and Hg, understanding the cause and limitations to mesa etched MCT annealing for dislocation reduction and the impact of TCA on device performance. The TCA results by Farrell, et. al. indicate that the anneal time can be minimized without significant variation in dislocation density reduction, which can further reduce diffusion in the sample. In the first part of this study, a new experimental setup is used to minimize the anneal temperature, while maximizing the number of cycles to reduce the defect density. In the second part of this study, determining the effect of annealing conditions and mesa orientation on the dislocation density of mesa etched MCT structures is carried out. In the third part of this study, the influence of dislocations on dark current and quantum efficiency of the MCT p-n junction diode has been carried out.

# Chapter 2. Background

## 2. 1. Crystal Lattice

To understand dislocations, there must be an understanding of crystals. An ideal crystal is a periodic array of unit cells. Unit cells are the smallest cubic structures that describe the macroscopic crystal symmetry and structure. There are various different crystal structures and those relevant to this analysis include the simple cubic cell, face-centered cubic (FCC), and zinc-blende lattice, as shown in Figures Figure 2, Figure 3 and Figure 4 [9]. In this chapter, the types of crystals, point defects and dislocations will be described.

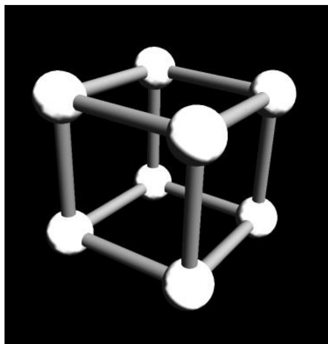

Figure 2. Simple cubic unit cell.

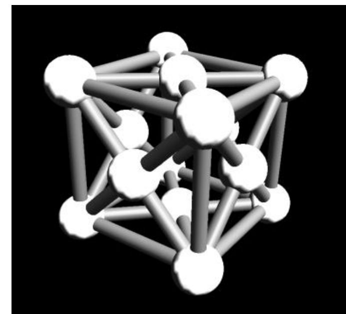

Figure 3. FCC unit cell.

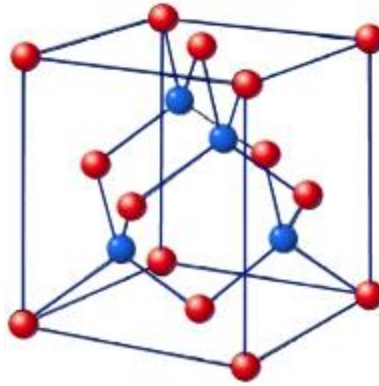

Figure 4. Zincblende unit cell. Red atoms are metal atoms and blue are non-metal atoms. If all atoms are the same, then this is a diamond lattice.

The atoms of a simple cubic lattice are positioned at the corners of a cube. Repeating this arrangement along the three cardinal axes gives a macroscopic crystal lattice that is a perfect crystal. The lattice constant, denoted as a, is the length of the side of the unit cell. The FCC structure is like the simple cubic cell with additional atoms on each face of the unit cell. The diamond lattice is two interlaced FCC structures with the second FCC structure in a starting position of $\left[\frac{a}{4}, \frac{a}{4}, \frac{a}{4}\right]$ relative to the origin. MCT is a variation of the diamond lattice called a zincblende lattice, where Hg or Cd are on one FCC lattice known as the metal lattice and Te is on the other FCC lattice. Each Te atom is bonded to four metal atoms with the Hg-Cd ratio determining the bandgap [9].

### *2. 2. Point Defects*

The simplest defect in a lattice is a point defect. Point defects are atomic displacements or misplacements on the crystal lattice. There are several various point

defects in a crystal lattice including interstitials, vacancies, anti-site and impurities. These are typically written using Kröger-Vink notation, where atom A in site B is written as $A_B$. Interstitial defects are defects where an atom within the crystal lattice does not sit on a lattice site, but rather, resides in the volume between lattice sites and are written as $A_i$, where i represents an interstitial position. Vacancy defects are vacant sites on the atomic lattice, written as $V_A$, denoting a vacancy, V, in site A. Vacancies and interstitials are often created in pairs, as the movement of an atom off a lattice site becomes an interstitial and leaves a vacancy behind. Anti-site defects are improper placements of atoms where a metal, Hg or Cd, sits on a non-metal lattice site, Te, or Te sits on the metal lattice site, which are not likely to occur due to the ionic nature of bonds in MCT. Impurities, as the name suggests, are atoms within the lattice that are not Hg, Cd, or Te, and are typically used to dope the material by adding excess charge to the material [9]. In MCT, the most important defects are $V_{Hg}$ and $Hg_i$. Due to the volatile nature of Hg and its weak bond to Te, these are the easiest to form within the crystal and have significant impacts on device performance. Berding, et. al. published simulations of point defect densities in MCT at 77K and is shown in Figure 5 [10]. It is quite apparent that the vacancy concentration is the largest defect density. An experimentally determined equilibrium pressure-temperature diagram by Vydyanath and Hiner, shown in Figure 6, displays the isohole concentrations in MCT at various temperatures and can be used to approximate the mercury vacancy defect density in MCT at a specific temperature and Hg overpressure.

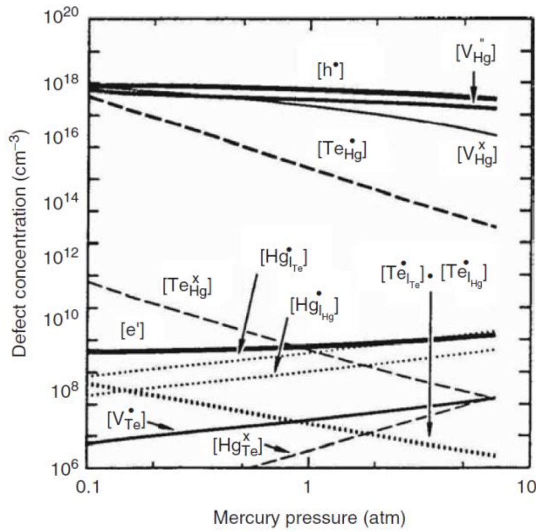


Figure 5. First principles calculation of native defect densities in MCT **[10]**.

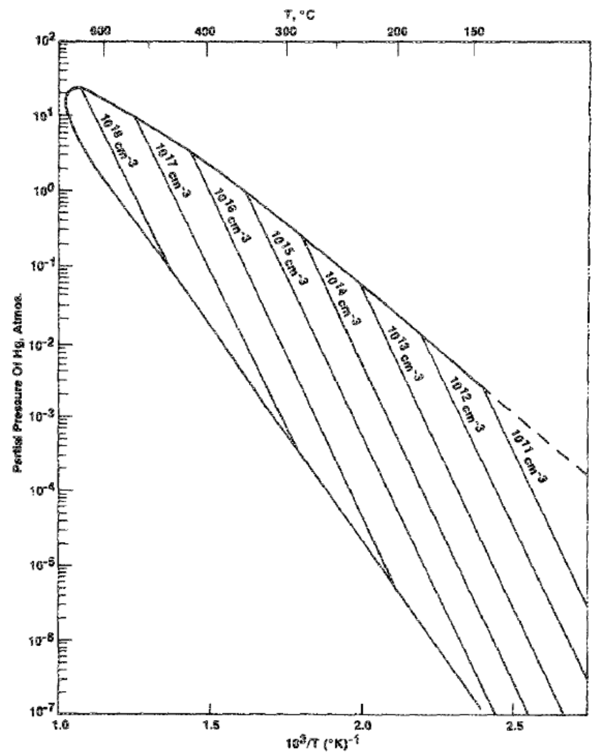


FIG. 11. *P-T* curve and isohole concentration lines for $Hg_{0.8}Cd_{0.2}Te$ from *T* = 150 to 655 °C.

Figure 6. Native vacancy concentration annealed under various Hg partial pressures **[11]**.

### *2. 3. Dislocation Types*

Dislocations are line defects due to stress relief and plastic deformation in a crystal. Dislocations are characterized by their Burgers vector, b, and line direction, t. The Burgers vector describes the magnitude and direction of distortion in the lattice and is the vector difference between a perfect crystal lattice and the lattice formed with a dislocation. This

is determined by creating a closed loop in the perfect crystal and comparing it to a closed loop of the same atomic steps around the dislocation. The additional step necessary to close the loop around the dislocation is b. There are three main types of dislocations: edge, screw and mixed. For an edge dislocation, the bonds are broken along one half-plane of a perfect crystal and the faces of this broken crystal plane are separated to insert a new half-plane. This is shown for a simple cubic cell in Figure 7a. The line direction is perpendicular to the Burgers vector with polarity described by the traditional right hand rule. The second dislocation is the screw dislocation. For a screw dislocation, the bonds along one half-plane of a perfect crystal are broken, the faces of the crystal are shifted by a lattice relative to each other and re-bonded. This is shown for a simple cubic cell in Figure 7b. The line direction is parallel to the Burgers vector. The third type is a mixed dislocation. The mixed dislocation is a combination of edge and screw, where the dislocation plane of atoms is neither exactly perpendicular, nor parallel to the line direction. The mixed dislocation is typically described by the angle between the Burgers vector and line direction [9].

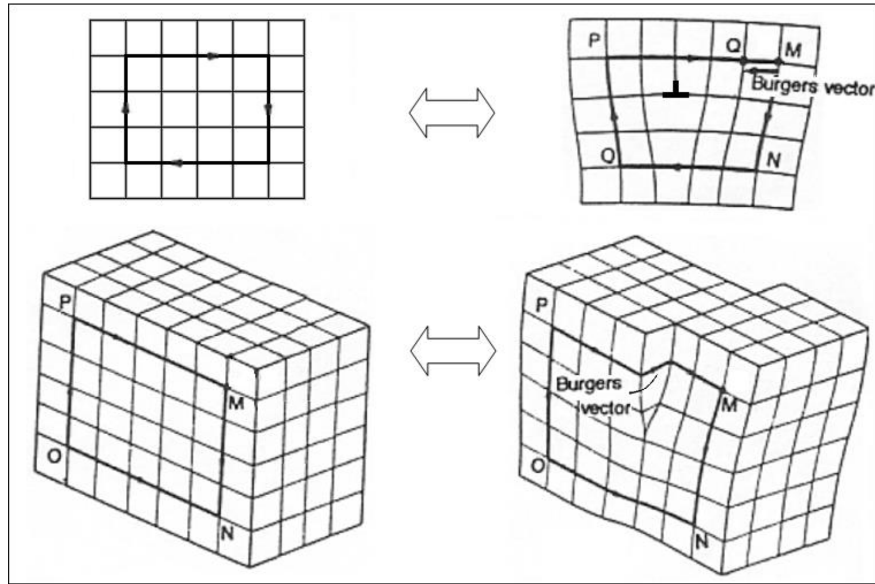


Figure 7. Dislocations in the simple cubic lattice with their respective burgers vectors, b, edge dislocation (top), and screw dislocation (bottom). **[12]**

Dislocations tend to form as misfit dislocations that turn up to create threading dislocations. During thin film growth, the growing epilayer will be stressed due to lattice mismatch to the substrate. The lattice spacing of the unit cell of the thin film will closely match the lattice spacing of the substrate and slowly relax with increasing epilayer thickness. At a certain thickness, the crystal will relax the misfit stress as it becomes energetically favorable to form misfit dislocations, which occur at a critical thickness known as the Matthews-Blakeslee critical thickness: [13]

$$d_c = \frac{b}{4\pi f_0 \cos(\theta)}\left(\frac{1 - v\cos^2\theta}{1 + v}\right)\ln\left(\frac{d_c}{b} + 1\right) \qquad 2.1$$

Where b is the length of the burgers vector, $\nu$ is the Poisson ratio, $f_0$ is the lattice misfit, and $\theta$ is the angle defining the orientation of the dislocation to the lattice. The lattice misfit strain, given by:

$$f_0 = \frac{a_{epi} - a_{sub}}{a_{sub}} \qquad 2.2$$

Where $a_{epi(sub)}$ is the epilayer(substrate) lattice constant. Table 2 gives lattice constants, misfit stress and critical thickness values for various sample and substrate compositions. Typical device designs of MCT require several microns of material so it is impossible to avoid misfit dislocations in lattice-mismatched systems.

Threading dislocations (TDs) are dislocations that “thread” through the crystal layer and can occur as either a continuation of a threading dislocation from the substrate or due to a misfit dislocation turning upwards to become a TD. Every misfit dislocation that does not end at a free surface is accompanied by a threading dislocation that turns upwards and can end at the top surface of the crystal, or form a dislocation loop with another threading dislocation. It is these dislocations that can impact device performance by threading through the device junction. Since dislocations can be detrimental to device performance, they must be minimized prior to device fabrication [5].

Table 2. Critical thickness determination from numerical analysis **[3]**

| Substrate | X | $a_{sub}$ (Angstroms) | X | $a_{epi}$ (Angstroms) | $f_0$ | $d_c$ (Angstroms) |
|---|---|---|---|---|---|---|
| CdTe | 1.00 | 6.4815 | 0.22 | 6.4659 | -2.44E-03 | 1207 |
| MCT | 0.45 | 6.4705 | 0.22 | 6.4659 | -7.41E-04 | 4986 |
| MCT | 0.30 | 6.4675 | 0.22 | 6.4659 | -2.78E-04 | 15458 |

### *2. 4. Dislocation Motion*

Dislocations in the zincblende lattice have been studied and analyzed in significant detail in previously published papers [14, 15]. Dislocation motion occurs by two methods: conservative and non-conservative motion. Conservative motion is the shifting of the atomic planes by dislocation glide, as can be seen in Figure 8a. Glide occurs along slip planes in the crystal. Slip planes are planes with the highest density of atoms and in FCC and zincblende crystals is {111} planes. The direction of the slip plane is the plane of the shortest lattice translation vectors and is <110> in FCC and zincblende crystals. Therefore, the slip system is the <110>{111} system and glide can occur when b and t both lie on the slip plane. Glide occurs by deforming a crystal enough to reform the bonds of the atoms of the dislocation to the next site. Dislocation glide is typically considered a low temperature or temperature-independent form of dislocation motion [9].

Non-conservative motion is known as dislocation climb, where dislocations will move perpendicular to the applied stress due to point defects like vacancies allowing the dislocation plane to be shifted. This is shown in the Figure 8b. Dislocations can be moved by climb by having vacancies move to the dislocation line and shift the dislocation planes up, known as positive climb, or interstitials move to the dislocation line and shift the plane down, known as negative climb. This can occur through mechanical force or chemical force. Due to the temperature dependence of vacancy formation and vacancy and interstitial motion, dislocation climb is highly temperature dependent [9].

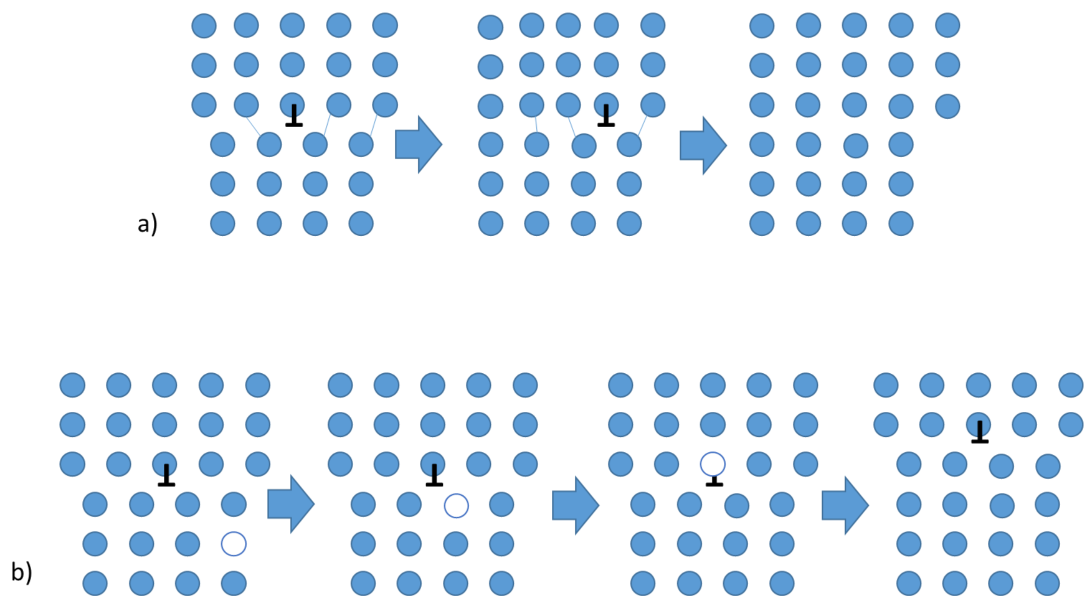


Figure 8. Graphics displaying a) glide motion and b) climb motion of edge dislocations. The dislocation is represented by the symbol "⊥".

*2. 5. Dislocation Forces*

To determine the reason for dislocation reduction due to annealing, the forces involved in the various forms of stresses can be analyzed. The two major forces acting on dislocations are the chemical force due to point defects and thermal stress due to coefficient of thermal expansion difference between the substrate and MCT epilayer.

If there is a significant nonequilibrium of vacancies or interstitials, dislocations can climb, where the dislocation half-plane will move perpendicular to the slip plane. The climb force per unit length, $f$, resulting from normal stress, $\sigma_{xx}$, of an edge dislocation is given as

$$f = \sigma_{xx} b \qquad 2.3$$

The work done, W, to move a dislocation of a line segment, l, over a distance, d, is:

$$W = fld \qquad 2.4$$

and the number of vacancies absorbed is $bdl/\Omega$, where $\Omega$ is the vacancy volume. The vacancy formation energy, $E^v$, is then changed by $f\Omega/b$. Finally, the equilibrium vacancy concentration is given by

$$\begin{aligned} c &= \exp(-(E^v + f\Omega/b)/kT) \\ &= c_0 \exp(-(f\Omega/b)/kT) \end{aligned} \qquad 2.5$$

where $c_0$ is the equilibrium concentration in a stress-free crystal, k is the Boltzmann constant and T is the temperature in Kelvin. Rewriting and solving for the force per unit length gives:

$$f = \frac{bkT}{\Omega} \ln\left(\frac{c}{c_0}\right) \quad 2.6$$

The shear stress is given by $\tau = f/b$ [9]. To induce dislocation motion in MCT, the necessary stress to apply to the material is the critically resolved shear stress, $\tau_c$, of ~1.5-2MPa at 300°C. At room temperature, the shear stress required is greater than 15MPa [3]. From isohole lines from the published graph of Vydyanath & Hiner, the equilibrium vacancy concentration and vacancy concentration with specific overpressures can be used to determine the stress acting on dislocations [11]. A 0.5% deviation from the equilibrium is enough to induce stress greater than the critical shear stress at temperatures above 300°C.

Significant thermal stress can induce glide. The difference in the coefficient of thermal expansion between a thin epilayer and thick substrate causes a significant stress in the epilayer during the heating and cooling of TCA. Thermal stress is described by Hooke's Law for expansion:

$$F = -kx \quad 2.7$$

where k is a spring constant and x is the distance traveled. The analogue to this system is:

$$\sigma = -E\epsilon \quad 2.8$$

where $\sigma$ is the stress, E is the Young's modulus, and $\epsilon$ is the strain. For thermal effects, an expansion term is added to the strain. Assuming a one-dimensional bimetallic thin film/substrate strip, the strain is given by:

$$\epsilon_i = \frac{1}{E}\sigma_i + \alpha_i \Delta T \qquad 2.9$$

where $\alpha$ is the coefficient of thermal expansion, ΔT is the change in temperature from the as-grown temperature and $i = 1\ or\ 2$ for substrate or epilayer, respectively. Assuming that there is no bending and no interfacial sliding, the strains in each layer are equivalent,

$$\epsilon_1 = \epsilon_2 \qquad 2.10$$

Plugging 2.9 into 2.10 gives:

$$\frac{\sigma_1}{E_1} + \alpha_1 \Delta T - \frac{\sigma_2}{E_2} - \alpha_2 \Delta T = 0 \qquad 2.11$$

Also, there is no net force on the sample, giving:

$$\sigma_1 A_1 + \sigma_2 A_2 = 0 \qquad 2.12$$

where $A_1$ and $A_2$ are the substrate and epilayer cross-sectional areas, respectively. This can be rewritten as:

$$\sigma_1 = -\frac{\sigma_2 A_2}{A_1} \qquad 2.13$$

.Substituting 2.13 into 2.11 gives:

$$-\frac{\sigma_2 A_2}{A_1 E_1} - \frac{\sigma_2}{E_2} + \Delta T(\alpha_1 - \alpha_2)$$

$$\rightarrow -\sigma_2 \left(\frac{A_2}{A_1 E_1} + \frac{1}{E_2}\right) + \Delta T(\alpha_1 - \alpha_2)$$

$$= 0 \rightarrow \sigma_2 = \frac{\Delta T(\alpha_1 - \alpha_2)}{\left(\frac{1}{E_2} + \frac{A_2}{A_1 E_1}\right)} \qquad 2.14$$

The ratio $A_2/A_1$ is equivalent to $t_2/t_1$, since the length under consideration is the same with no interfacial sliding and with such a small epilayer thickness, the second term in the denominator of 2.14 can be ignored, giving:

$$\sigma_2 = E_2 \Delta T(\alpha_1 - \alpha_2) \qquad 2.15$$

The coefficient of thermal expansion for MCT is given by [3]:

$$\alpha_2 = 4 \times 10^{-6} + 4 \times 10^{-9} \times T \qquad 2.16$$

Measured Young's modulus values vary between 31 and 56 GPa for MCT and a value of 43GPa is used in this analysis. The $\alpha_1$ is given as $2.5\text{x}10^{-6}$ $K^{-1}$ for Silicon [3]. The stresses at annealing temperatures of greater than 350°C are on the order of tens of MPa, enough to induce dislocation motion. In this study, experiments are carried out to determine the major effects of chemical and thermal stress for added benefit in applications to material quality improvement and device applications.

### *2. 6. Dislocation Strain, Stresses, and Energy*

Energy minimization is dependent on the self-energy of the dislocation. To understand the energy considerations, the physical shift in position, stress, strain and work

must be understood. On a basic atomistic level, a dislocation is simply a misplacement of a line of atoms on a crystal. Each dislocation causes a shift, or displacement, in the crystal structure. The displacement of a screw dislocation is only in one direction, given as [9]:

$$u_z = \frac{b}{2\pi}\tan^{-1}\frac{y}{x} \qquad 2.17$$

The strains due to this displacement are given by the equation:

$$\epsilon_{ii} = \partial u_i/\partial x_i, \text{ and} \qquad 2.18$$

$$\epsilon_{ij} = \frac{1}{2}\left(\frac{\partial u_i}{\partial x_j} + \frac{\partial u_j}{\partial x_i}\right) \qquad 2.19$$

With $i, j = x, y, z$. The strain due to a screw dislocation only in the z direction is given as:

$$\epsilon_{xx} = \epsilon_{yy} = \epsilon_{yx} = \epsilon_{xy} = \epsilon_{zz} = 0 \qquad 2.20$$

$$\epsilon_{zy} = \epsilon_{yz} = -\frac{b}{4\pi}\frac{x}{x^2+y^2} \qquad 2.21$$

$$\epsilon_{zx} = \epsilon_{xz} = -\frac{b}{4\pi}\frac{y}{x^2+y^2} \qquad 2.22$$

The linear stresses can be determined from the strain using the equation $\epsilon_i = (\sigma_i - \nu\sum\sigma_j)/E$ for $i \neq j, i, j = x, y, z$. The shear stresses can be determined by $\epsilon_{ij} = \sigma_{ij}/\mu$ for the respective *ij* components, where $\mu$ is the shear modulus. For $i \neq j, \sigma_{ij}$ is called shear stress, $\tau_{ij}$. For a screw dislocation, the nonzero stresses are:

$$\sigma_{xz} = \sigma_{zx} = -\frac{\mu b}{4\pi}\frac{y}{x^2+y^2} \qquad 2.23$$

$$\sigma_{yz} = \sigma_{zy} = -\frac{\mu b}{4\pi}\frac{x}{x^2+y^2} \quad 2.24$$

The displacement of an edge dislocation is quite a bit more complex and is given as:

$$u_x = -\frac{b}{2\pi}\left[\tan^{-1}\frac{y}{x} + \frac{1}{2(1-\nu)}\frac{xy}{x^2+y^2}\right] \quad 2.25$$

$$u_y = -\frac{b}{2\pi}\left[(1-2\nu)\ln(x^2+y^2) + \frac{(x^2-y^2)}{x^2+y^2}\right] \quad 2.26$$

The stresses are given as:

$$\epsilon_{xx} = \frac{yb}{2\pi}\frac{(\mu y^2 + (2\lambda+3\mu)x^2)}{(\lambda+2\mu)(x^2+y^2)^2} \quad 2.27$$

$$\epsilon_{yy} = \frac{yb}{2\pi}\frac{(2\lambda+\mu)x^2 - \mu y^2}{(\lambda+2\mu)(x^2+y^2)^2} \quad 2.28$$

$$\epsilon_{xy} = \epsilon_{yx} = \frac{b}{2\pi(1-\nu)}\frac{x(x^2-y^2)}{x^2+y^2} \quad 2.29$$

$$\epsilon_{zz} = \epsilon_{yz} = \epsilon_{zy} = \epsilon_{zx} = \epsilon_{xz} = 0 \quad 2.30$$

Where $\lambda$ is the Lame constant and $\nu$ is Poisson's ratio. The stresses derived from these strains are:

$$\sigma_{xx} = \tau_0\frac{y(3x^2+y^2)}{(x^2+y^2)^2} \quad 2.31$$

$$\sigma_{yy} = -\tau_0\frac{y(x^2-y^2)}{(x^2+y^2)^2} \quad 2.32$$

$$\sigma_{zz} = \frac{2\tau_0 \nu y}{x^2+y^2} \quad 2.33$$

$$\tau_{xy} = -\tau_0 \frac{x(x^2 - y^2)}{x^2 + y^2} \quad 2.34$$

Where $\tau_0 = \frac{\mu b}{2\pi(1-\nu)}$. A mixed dislocation is a combination of edge and screw dislocations and its displacement cannot be easily described due to its complexity.

Due to the strain caused by the dislocation, there is an associated self-energy contained by the dislocation. The elastic strain energy for a two dimensional strain is given as:

$$W = \frac{1}{2}\sum(\sigma_{ij}\epsilon_{ij}), i, j = x, y, z \quad 2.35$$

Inputting all of the stress and strain components, the following result is obtained:

$$W = \frac{1}{2\mu}\left[\frac{\lambda + \mu}{3\lambda + 2\mu}\left(\sigma_{xx}^2 + \sigma_{yy}^2 + \sigma_{zz}^2\right) + \left(\sigma_{xy}^2 + \sigma_{xz}^2 + \sigma_{yz}^2\right) - \frac{\lambda}{3\lambda + 2\mu}\left(\sigma_{xx}\sigma_{yy} + \sigma_{yy}\sigma_{zz} + \sigma_{zz}\sigma_{xx}\right)\right] \quad 2.36$$

With this, the energy per unit length, U, due to the dislocation can be determined with:

$$U = \iint W dx dy = \iint W r\, dr\, d\theta \quad 2.37$$

For ease of calculation, integrals are typically done in spherical coordinates. Due to the singularity of taking the integral to the core of the dislocation and the breakdown of continuum elastic theory near the core, the energy is broken into two integrals:

$$U = \int_0^{r_0} W\ 2\pi r\ dr + \int_{r_0}^{R} W\ 2\pi r\ dr = U_{core} + U_{elastic} \qquad 2.38$$

Where the R is the limit of the crystal, or the strain field, $r_0$ is a cutoff radius that shall be set as 5b in these calculations. The limit of the strain field, R, is set as half of the average distance between dislocations. The core energy per unit length, $U_{core}$, is approximated as $0.1\mu b^2$ [9]. The energy per unit length for a screw dislocation is given as:

$$U_{elastic,screw} = \frac{\mu b^2}{4\pi} \ln\left(\frac{R}{5b}\right) \qquad 2.39$$

And for an edge dislocation is:

$$U_{elastic,edge} = \frac{\mu b^2}{4\pi(1-\nu)} \ln\left(\frac{R}{5b}\right) = \frac{U_{elastic,screw}}{(1-\nu)} \qquad 2.40$$

And for a mixed dislocation is:

$$U_{elastic,mixed} = U_{elastic,edge}\,(1 - \nu \cos^2\theta) \qquad 2.41$$

Where $\theta$ is the angle between the dislocation line and Burgers vector with $\theta = 90°$ for an edge dislocation and $\theta = 0°$ for screw dislocation. As can be seen, the difference in energy between screw and edge dislocation is only a small factor of 1.5 for MCT. The energy is proportional to $b^2$. For two dislocations, with Burgers' vectors $b_1$ and $b_2$, to coalesce into a

new dislocation with a new burgers vector, $b_3$, it must have a self-energy less than or equal to the component dislocations energies, or, equivalently, $b_3^2 \leq b_1^2 + b_2^2$.

## Chapter 3. Thermal Cycle Annealing

### *3. 1. TCA: Theory*

The goal in this work on thermal cycle annealing (TCA) of MCT grown on CdTe/Si substrates is to reduce the dislocation density while minimizing diffusion. This requires an understanding of dislocation interactions. The basis for the current understanding follows the model by Yamaguchi, et al. (1988) where GaAs on Si was annealed cyclically, showing decreased dislocation density, and expanded to MCT by Farrell, et al. Dislocations can be removed by spontaneous annihilation or coalescence described by the following rate equations:

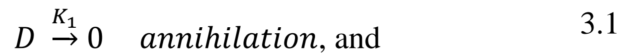

$$D \overset{K_1}{\rightarrow} 0 \quad annihilation\text{, and} \qquad 3.1$$

$$D + D \overset{K_2}{\rightarrow} D_2, coalescence \qquad 3.2$$

Where D and $D_2$ are the densities of dislocations and coalesced dislocations, respectively. $K_1$ and $K_2$ are rate constants. In dislocation interactions, coalescence leading to annihilation or fusion occurs based on the combined Burgers vector of two interacting dislocations. If the burgers vectors are opposite, then the dislocation will coalesce and annihilate. If they are not exactly opposite, they may coalesce as fusion and re-emit as a dislocation with a different burgers vector. This occurs due to energy minimization.

Dislocations on the same slip plane will be repulsive if their burgers vectors are in the same direction and attractive if their burgers vectors are in opposite directions. As dislocations move throughout the material along their respective slip planes, the minimum distance to invoking dislocation-dislocation interactions is the annihilation radius, given approximately as [16]:

$$r_A \cong \frac{\mu b}{2\pi\sigma_p} \cong 0.7\ \mu m \qquad 3.3$$

where μ is the shear modulus, b is the Burgers vector, and $\sigma_p$ is the Peierls' stress of the material. This reaction radius is the distance the interaction forces between TDs is sufficient to overcome the Peierls' energy barrier (2.5 eV in MCT). The coalescence and annihilation reactions are represented by the equations [17]:

$$\frac{dD}{dt} = -K_1 D - K_2 D^2 \qquad 3.4$$

$$\frac{dD_2}{dt} = \frac{nK_2 D^2}{2} \qquad 3.5$$

Where n is the fraction of dislocations taking part in coalescence interaction. The initial conditions include: $D = D_0$, the initial defect density, and $D_2 = 0$. The solutions to these equations are:

$$D = \frac{1}{\left(\frac{1}{D_0} + \frac{K_2}{K_1}\right)\exp(K_1 t) - \frac{K_2}{K_1}} \qquad 3.6$$

$$D_2 = \left(\frac{D_0^2 K_2}{K_1}\right)\{1 - (\exp(-K_1 t))^2\} \qquad 3.7$$

The main method of dislocation annihilation is the coalescence mechanism, allowing the approximation of $K_1 D_0 \ll K_2 D_0^2$. Under this approximation, the solutions become:

$$D = \frac{D_0}{1 + D_0 K_2 t} \tag{3.8}$$

$$D_2 = 2nD_0^2 K_2 t \tag{3.9}$$

The total dislocation density per cycle is then a sum given by:

$$D_{tot}(cycle\ N) = D(cycle\ N) + D_2(cycle\ 1) + \ \dots + D_2(cycle\ N) \tag{3.10}$$

for N cycles. With this information, the number of cycles can be used to optimize cycle annealing parameters towards the goal of minimal thermal impact while sufficiently reducing dislocation density. The $K_2$ constant is determined by using the equation:

$$\frac{1}{D_0} - \frac{1}{D_1} = K_2 t = K_2 t_a N \tag{3.11}$$

Where $t_a$ is the time spent at the annealing temperature and N is the number of cycles. The rate constant $K_2$ is the slope obtained by modeling $\left(\frac{1}{D_0} - \frac{1}{D_1}\right)\ vs.\ t_a N$. The $K_2$ rate constant is proportional to the average dislocation velocity, expressed as: $v = v_0 e^{-\frac{E_a}{kT}}$, where $E_a$ is the activation energy to begin dislocation movement. Therefore, conducting anneals at various temperatures and obtaining the slope from the dislocation density reduction, the activation energy can be determined. For MCT, this activation energy is 0.93 +/- 0.1 eV [6]. From all of this information, the dislocation reduction behavior of the planar MCT material after TCA can be modeled, as shown in Figure 9 for various temperatures and

anneal cycles. As expected, the higher the temperature, the faster the dislocation density reduces, but all anneal conditions approach the limit of $1\text{x}10^6$ $\text{cm}^{-2}$.

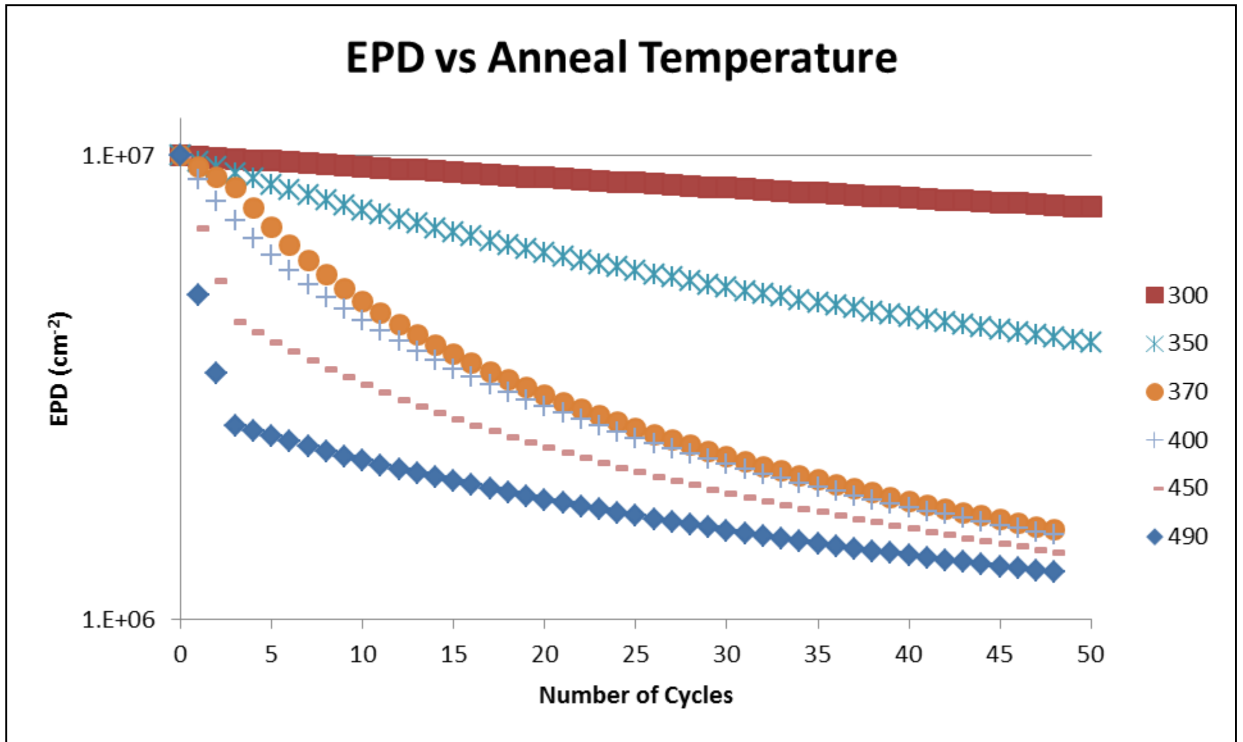


Figure 9. Dislocation density for various anneal schedules and cycles.

### *3. 2. TCA: Experiment*

Samples of MCT are grown on $2 \times 2$ $\text{cm}^2$ CdTe/Si substrates by MBE in a DCA ultra high vacuum MBE growth chamber. The MCT is grown using CdTe and Te effusion cells and Hg beam flux with a substrate temperature of ~180°C, as determined by a pyrometer. The growth rate is nominally 2 μm/hr. Further details of MBE growth have

been described elsewhere [1]. The MCT absorber layer composition is determined by post-growth Fourier-transform infrared (FTIR) spectroscopy using a Nicolet 8700 FTIR spectrometer. The as-grown MCT absorber layer has a typical x-ray diffraction (XRD) full-width at half-maximum (FWHM) of 100-200 arc-seconds and etch pit density (EPD) of around $1 \times 10^7$ cm$^{-2}$ as decorated with the Benson etch [18]. The typical device structure is grown with a high x buffer layer of approximately 0.5 μm, an absorber layer of 6-10 μm (optimally designed depending on composition), another high x cap layer of approximately 0.3 μm and a ~30 nm CdTe cap layer. High x denotes 13% higher Cd concentration than the absorber layer. The device design will be discussed further in the device chapter.

A quartz ampoule, plug and sample holder, or insert, are rinsed with acetone and methanol and baked at 450°C. For additional cleanliness, the glassware is subjected to a flameout procedure where they are placed under vacuum of $10^{-6}$ Torr and heated with an oxygen-hydrogen torch to further remove any contaminants. After the flameout, the ampoule, plug and insert are allowed to cool to room temperature under vacuum.

Pieces of the as-grown MCT ($5 \times 5$ mm$^2$) are cleaved from a $2 \times 2$ cm$^2$ wafer and cleaned with solvents. The samples are then dipped for 10 seconds in a 10% HCl solution to remove any surface oxide and rinsed under running de-ionized water. Samples are placed on the quartz insert inside the quartz ampoule, as shown in Figure 10. Mercury is placed in a cavity of the sample holder intended for holding Hg away from samples. The quartz plug is placed ~15 cm from the closed end of the ampoule. The ampoule is pumped down to low $10^{-5}$ Torr and sealed around the quartz plug with an oxygen-hydrogen torch. To prevent

heating of the samples during sealing, a wet cloth is wrapped around the ampoule in the region where the samples are placed.

Figure 10. Quartz ampoule showing sample positions and Hg placement.

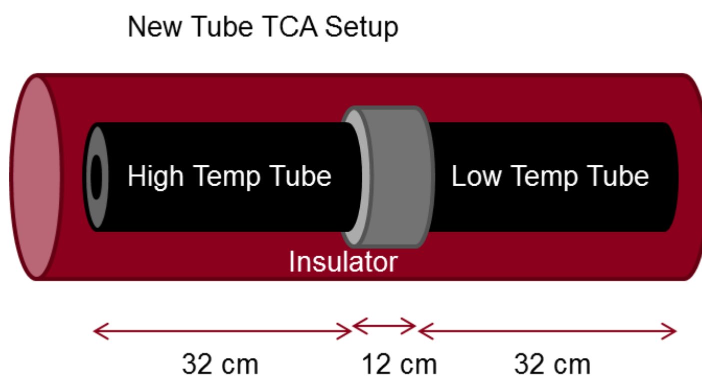


Figure 11. Graphite tube setup as placed inside furnace.

TCA is conducted by mechanically moving the ampoule between a high temperature tube and a low temperature tube, as seen in Figure 11. To prevent mercury condensation on the sample surface at the start of annealing, the ampoule is placed inside the low temperature tube while the tubes are at room temperature, and the tubes are heated slowly. Graphite tubes have a high thermal mass allowing little variation in temperature

through the length of the tube. Due to the conductive heating of the samples, the temperature inside the ampoule changes at a rate greater than 100°C per minute when the ampoule is moved from one temperature zone to another. After completing all cycles, the ampoule is moved into the low temperature graphite tube and cooled to room temperature over several hours. This slow, controlled cooling process is necessary to prevent condensation of mercury on the surface and to prevent the creation of Hg vacancies in the MCT material.

After cooling to room temperature, the samples are removed from the ampoule and etched for 30 seconds in 0.1% Bromine-Methanol to remove the cadmium rich layer on the surface, twice rinsed in methanol and blown dry with nitrogen. To reveal the dislocations, the samples are etched with the Benson etch solution for 50 seconds, rinsed under running de-ionized water and blown dry [2]. The dislocations are observed under bright field microscopy using a Leica IN20 microscope and counted using D.E. Omega .

Before and after annealing, the MCT layer crystallinity is characterized using high resolution x-ray diffraction (XRD) full-width, half-maximum (FWHM) measurements. This is accomplished through the use of an X'pert Pro Analytical system using a Cu-$K_\alpha$ source. The samples are characterized by $\omega$-$2\theta$ scans. Due to the 4° tilt off the (211) direction of the sample, the XRD measurement is done at two different $\omega$ angles and the FWHM is taken as an average between the two XRD FWHM measurements.

To look at the compositional integrity of the layers, secondary ion mass spectroscopy (SIMS) is used to determine the Cd composition throughout the material.

SIMS is conducted using a Cs+ atom that strikes the surface with enough energy to eject the surface atom from the sample and measure the secondary ion with a mass spectrometer. Analyzing the SIMS of the as-grown and annealed samples determines the influence of annealing conditions on the compositional integrity of the annealed material.

### *3. 3. TCA: Results & Discussion*

To begin this analysis, 32 60-second cycles of TCA were conducted at 450°C, 400°C, 370°C, 350°C and 320°C to compare against the "standard" 4 5-minute cycles at 500°C developed by Farrell, et. al [7]. As shown in Figure 12, a significant reduction in EPD at temperatures as low as 350°C is observed, but the EPD reduces exponentially with increasing temperature. The EPD approaches the minimum of $1x10^6$ $cm^{-2}$ for 32 cycles of annealing at 450°C. To examine the correlation between number of cycles and final EPD of the sample, the effect of 32, 64, 128, and 256 annealing cycles was analyzed with the anneal temperature held constant at 350°C for several different samples. The dislocation density reduction is exponentially dependent on the number of cycles and again saturates near $1x10^6$ $cm^{-2}$, as seen in Figure 13. To determine if this is an absolute limit, a few samples of MCT are annealed at an elevated anneal temperature of 400°C with 512 annealing cycles, but was still subject to the EPD limit of $1x10^6$ $cm^{-2}$. The $1x10^6$ $cm^{-2}$ EPD is considered low enough for short-wavelength and mid-wavelength infrared device applications, but is not suitable for the narrow band gap, long wavelength infrared MCT detectors due to a high reverse bias dark current at this dislocation density [4]. This indicates a fundamental limitation to the use of silicon-based substrates for fabricating planar MCT devices.

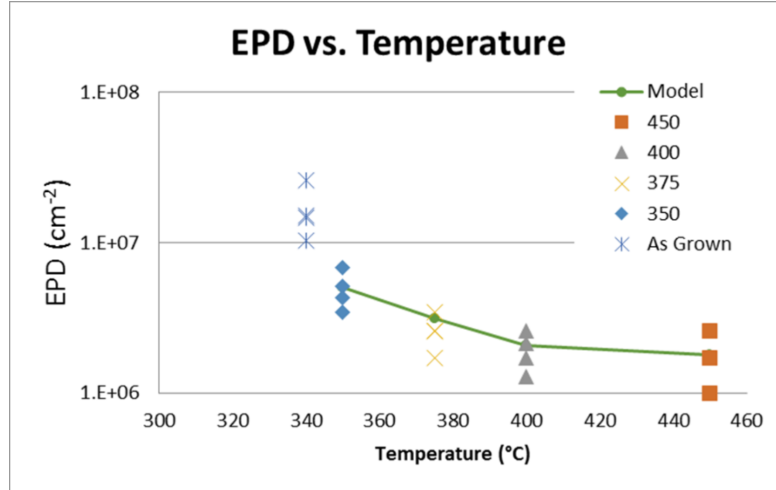


Figure 12. Restults of annealing with 32 2-minute cycles and the various high temperatures.

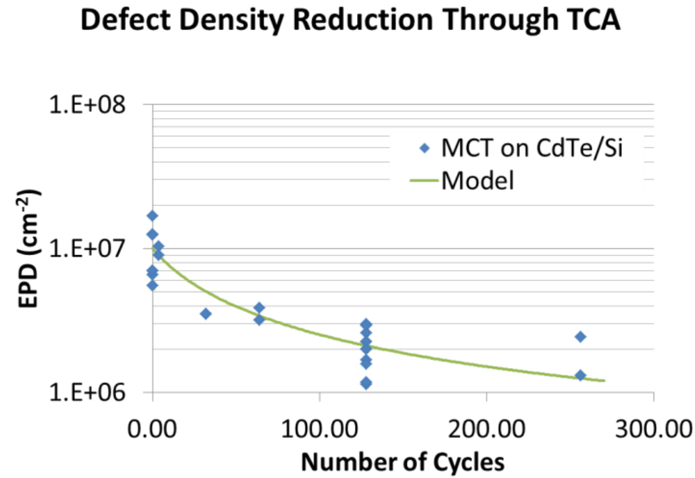


Figure 13. TCA with varied number of cycles between 350°C and 250°C.

The annealed samples are characterized by XRD measurements. The effect of TCA on crystallinity of the sample is shown in Fig. 6. The pre-annealed, as-grown FWHM is 126” and reduces to 85” after being treated with 128 60-second anneals at anneal temperature of 350°C. Final FWHM of samples subjected to various anneal schedules ranged from 65” to 85”. This value is similar to XRD FWHM measurements by Farrell, et al. Farrell et al. achieved minimum dislocation density of $1x10^6$ $cm^{-2}$ after four 5-minute, 494°C anneals with FWHM varying between 65” to 80” [7]. The total anneal time of the samples is about 2 hours and total time at temperature is approximately 20 minutes for both TCA schedules, but in the present study a significantly reduced annealing temperature is used to achieve similar final material properties.

The cadmium depth profiles, as measured by SIMS, on the samples before and after 128 cycle TCA are shown in Figure 14. As stated before, the surface layer was grown as a cadmium rich layer with a typical composition of x = 0.33. The results show that the interdiffusion of cadmium from the surface to the MCT bulk is very sensitive to the annealing temperature. The diffusion is minimal for annealing at 350°C. The use of an anneal temperature of only 20°C higher, at 370°C, shows a significantly higher degree of diffusion due to the mercury diffusion coefficient increasing by an order of magnitude from 350°C to 370°C. Therefore, minimum dislocation density can be achieved while maintaining the as-grown Cd profile in the device structure at annealing temperatures as low as 350°C.

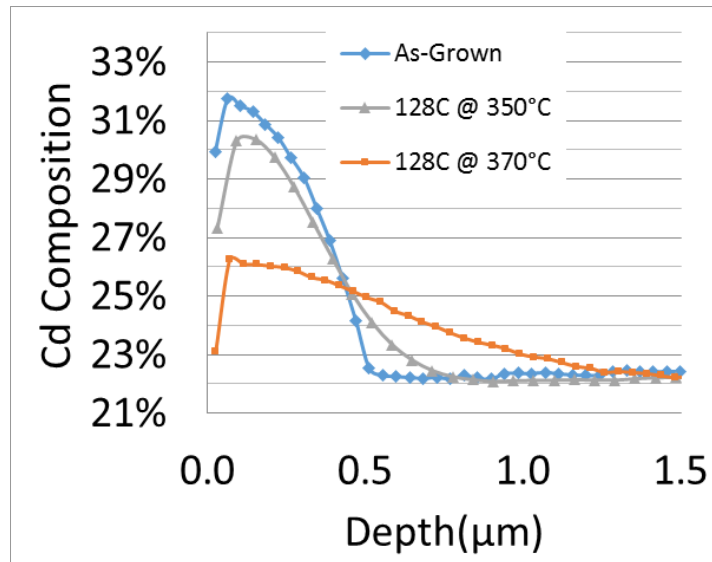


Figure 14. SIMS profile of the as-grown structures and two different anneal schedules.

Although a significant reduction in EPD with number of cycles was observed in some samples, others show very little variation in EPD with TCA. Understanding these differences is necessary for applying the results of this work to devices. There are several factors that can limit the utility of TCA. The device structure, initial (as-grown) EPD of the material, and the thickness of the MCT layer are some of the factors limiting the final EPD of annealed samples.

To determine the influence of MCT layer thickness, TCA was performed on MCT layers that are 4 μm thick, which is significantly thinner than the 8-10 μm thickness of the rest of the samples in this work. As shown in Figure 15, the TCA did not reduce the dislocation density in a 4 μm thick MCT layer, whereas, in MCT layers that are thicker, there is a reduced dislocation density, as expected by the model. Previously published depth

based EPD measurements by Farrell, et al [6] for 4 cycle TCA at 494°C showed a reduction in defect density near the surface of the sample, but the defect density began increasing with increasing depth from the MCT surface. This increase starts at ~5 μm away from the MCT/CdTe substrate interface. At the location which is 4 μm away from the MCT/CdTe interface the EPD was ~$1x10^7$ $cm^{-2}$. This implies there is no reduction in defect density at distances less than 4 μm from the MCT/CdTe substrate interface and indicates that the benefits of TCA can be realized only in samples much thicker than 4 μm. This limit is most likely due to dislocation pile-up limiting dislocation motion near the CdTe/MCT interface.

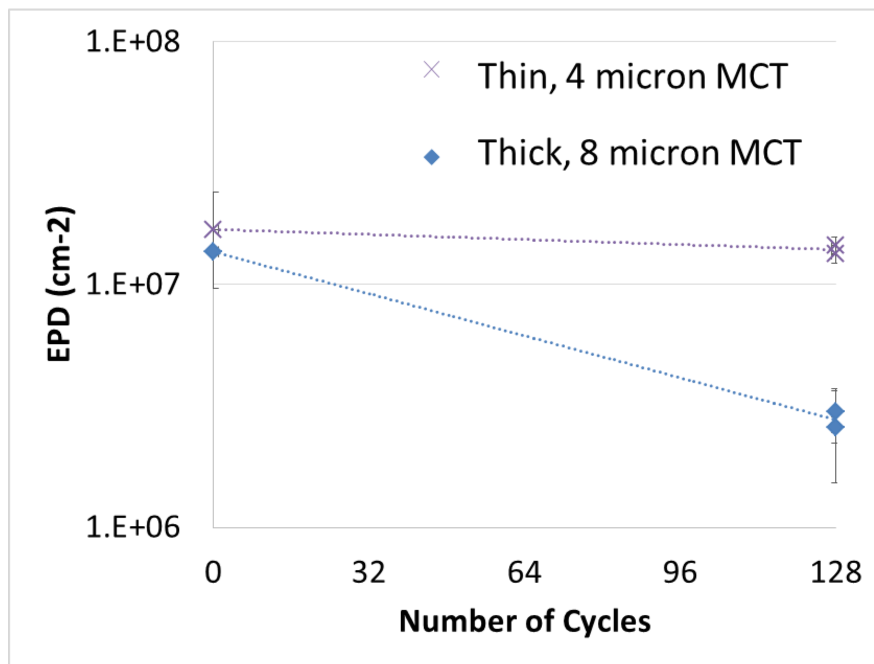


Figure 15. EPD vs. number of cycles comparing thin and thick samples

a)

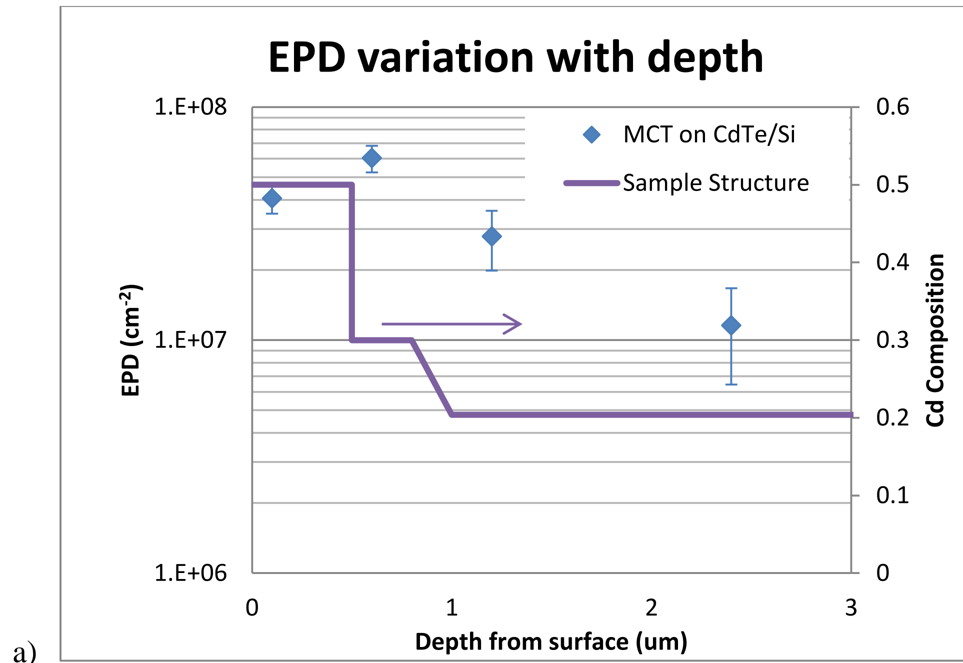


b)

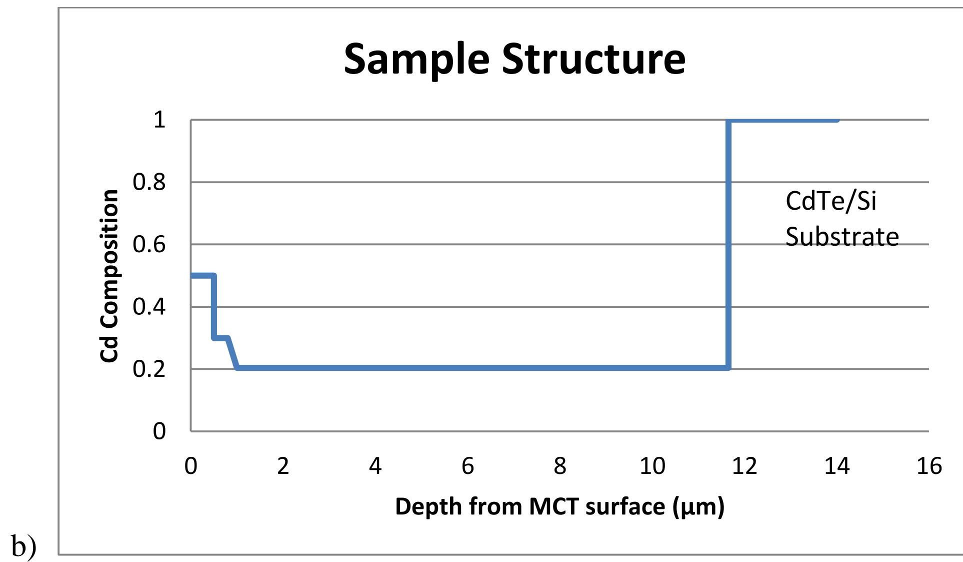


Figure 16. Structure of sample with a) EPD vs Depth showing the impact of interfaces and, b) the full layer structure from the substrate.

To study the applicability of TCA to varied device structures some samples were designed with varying Cd composition cap layers. One such sample had a high cadmium composition layer at the surface of the MCT layer, as shown in Figure 16, alongside the EPD variation with depth. Sister samples were also analyzed in which the high Cd composition layer was removed by a 30s Bromine-Methanol (0.1%) etch. This experiment was designed to study the limiting nature of having a high stress interface on dislocation density. In the depth based measurements, an increase in EPD near the cap layer interface and decreasing EPD moving away from this interface is observed. When anneals are performed after removing the surface layer, the EPD of the sample reduced as is normally expected. This presents a potential issue with the applicability of TCA to complex device structures. The stress due to the interface pins the threading dislocations due to the higher Peierls' barrier in CdTe, leading to a higher resistance to dislocation motion.

The TCA improves material quality depending on the MCT layer thickness, but the effect of initial (as-grown) MCT sample quality was uncertain. Increasing sample yield is important in industrial applications for minimizing cost and downtime. If a sample is grown with a high dislocation defect density, but can be salvaged by the TCA dislocation reduction, the yield of the manufacturing process can be improved. Poor growth conditions can lead to dislocation densities of greater than $5x10^7$ $cm^{-2}$. Several anneals were conducted with several different samples that had a high initial EPD of greater than $5x10^7$ $cm^{-2}$, but showed no improvement with any TCA schedule, even at high anneal temperatures of 500°C and a significant number of anneal cycles. This is due to an increased energy barrier

to dislocation motion which is due to the high strain field created by various, repulsive dislocations within close proximity of each other.

Although the EPD is reduced significantly by the TCA, the main limitation remains the inability to decrease the defect densities below $1x10^6$ $cm^{-2}$. This seems to be an inherent limitation to planar MCT grown on silicon based substrates. This dislocation density reduction limitation can be problematic for long-wavelength infrared, narrow band-gap devices and requires further study on TCA or alternate methods to achieve EPD of $<5x10^5$ $cm^{-2}$, as it is in MCT grown on lattice matched CdZnTe substrates. There are a few possible explanations for this limit. One possibility is the formation of sessile dislocations that cannot move. Another possibility is simply that the dislocations cannot get within the annihilation radius of each other, not allowing further dislocation reduction, as exhibited by the annealing with large number of cycles of 256 and 512 that do not go below $1x10^6$ $cm^{-2}$.

To understand the physics of what is occurring, the temperature variation in the ampoule was measured. The round bottom of the ampoule and the temperature at the location of the sample is analyzed to approximate the mercury overpressure. The calibration of the samples is shown in the Figure 17. There is a very significant temperature difference between these two locations. It is assumed that the overpressure of mercury in the sample will be controlled by the coldest point in the ampoule. In Figure 17, the temperature of the end of the ampoule is T_rb and the sample location is T_in.

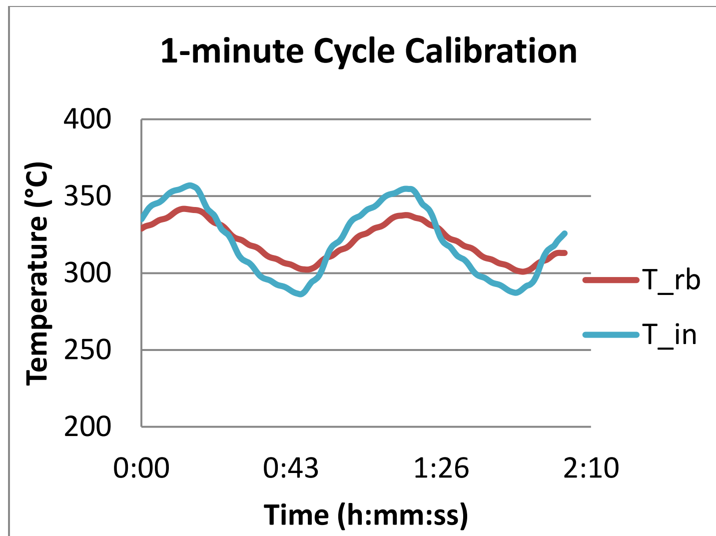


Figure 17. One minute cycle calibration

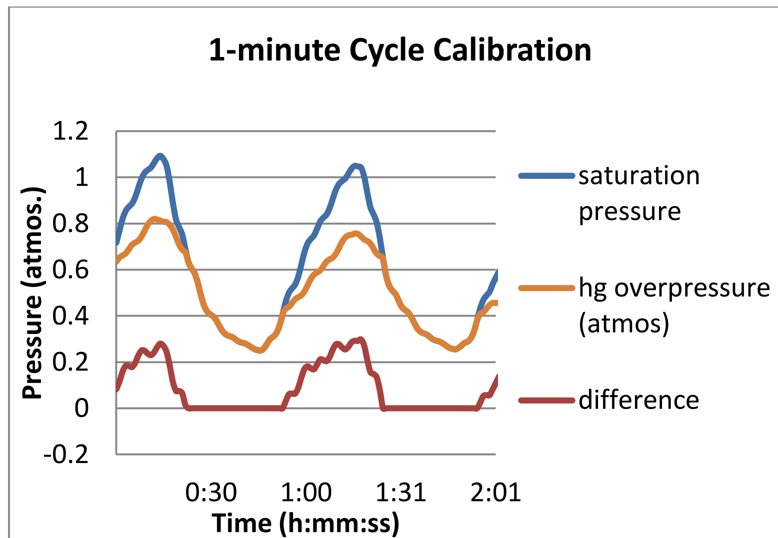


Figure 18. Expected saturation overpressure based on cold point temperature and saturation pressure for sample temperature.

Based on isohole concentrations by Vydyanath & Hiner, the equilibrium vacancy concentration and the vacancy concentration in the MCT epilayer can be determined. A maximum temperature difference of 18°C is observed between the ampoule's round bottom temperature and sample temperature, with the sample temperature at 350°C for a few seconds per cycle, as can be seen in Figure 18. From this, the difference in vacancy concentration can be as much as 20%, that is, $c/c_0 = 0.8$ for the chemical climb force calculation. Therefore, if vacancies are creating a significant force on the dislocations, simply controlling the Hg overpressure should reproduce the dislocation density reduction and simulate the process without the need or complication of cycling. For 128 cycles, there is only a few hundred seconds, or about 5 minutes, of deficient Hg overpressure acting on the sample. To determine the effect of chemical force on dislocation motion, the Hg temperature was held at various temperatures of 350°C, 370°C, and 390°C and the sample temperature was raised up to 400°C and held for 20 minutes. The time of 20 minutes is used to exaggerate the dislocation climb, if it had occurred. In all three anneals, the dislocation density remained similar to the as-grown material, but with noticeable roughening of the surface with decreasing Hg overpressure, as is expected. Therefore, diffusion-controlled processes inducing dislocation climb are not believed to be a major factor in the dislocation reduction observed in MCT during TCA.

As another test to determine the source of dislocation reduction during TCA, trials were conducted under isothermal and Hg-deficient conditions with the Hg temperature held at 30°C below the sample temperature. The results can be seen in the table. There is some additional dislocation reduction under Hg-deficient conditions, but cycling has a greater

impact on all samples. The results indicate that the thermal stress plays a greater role in dislocation reduction than the chemical stress from vacancies.

Table 3. Anneal Conditions. vac refers to vacancy anneal with Hg held at 30°C below sample and iso refers to isothermal anneal.

| Anneal # | Anneal condition | MCT091707 EPD ($cm^{-2}$) | MCT320 EPD ($cm^{-2}$) |
|---|---|---|---|
| 1 | As-grown | 5.98E+06 | 1.37E+07 |
| 2 | 20m vac | 3.40E+06 | 9.65E+06 |
| 3 | 20m iso | 4.57E+06 | 1.01E+07 |
| 4 | 2 cycles at 10 min. each, vac | 3.26E+06 | 6.77E+06 |
| 5 | 2 cycles at 10 min. each, iso | 2.49E+06 | 7.62E+06 |

### *3. 4. TCA: Conclusion of Planar TCA Experiment*

The dislocation density in samples of MCT grown on CdTe/Si has been reduced to low $10^6$ $cm^{-2}$ while minimizing Cd diffusion. The new, graphite tube TCA setup has allowed faster heating and cooling rates to optimize defect reduction at lower temperatures. It also resulted in a better sample surface morphology with desirable results. The use of a high anneal temperature of 350°C and anneal cycle duration of less than 1 minute,

significantly limits Cd diffusion while obtaining a lower EPD. It has been shown that the EPD does not reduce as significantly in the absorber layer of the MCT structure when there is a sharp interface or when the MCT layer is relatively thin (< 4 μm). Therefore, dislocation reduction is maximized with minimal diffusion in samples of thickness greater than 4 μm with TCA between 350°C and 250°C for 128 cycles. The main limitation of TCA remains to be the inability to reduce defect density below $1x10^6$ $cm^{-2}$ for MCT grown on silicon-based substrates.

# Chapter 4. Etched Mesa Structures

Thermal cycle annealing (TCA) has been shown to reduce the dislocation density in planar MCT grown on CdTe/Si substrates down to a saturation limit of $1x10^6$ $cm^{-2}$. This dislocation density may be acceptable for applications to mid-wavelength and short-wavelength infrared, but is limited for application to the narrower bandgap, long-wavelength infrared MCT devices [5]. The saturation at $1x10^6$ $cm^{-2}$ is believed to be due to the formation of sessile dislocations from the fusion of glissile dislocations [19].

Mesa structures on mismatched substrates have shown dislocation reduction with several different material systems. This is typically explained with the use of image forces. For a dislocation near a free surface, there is force acting on the dislocation due to the sidewall surface stress being zero, equivalent to a negative dislocation equal in magnitude and opposite in Burgers vector across the free surface known as an image force. The effect of image forces has been observed in various systems, including GaN grown on SiC mesa surfaces that showed as grown reduced defect density, and SiGe-on-insulator or ZnSe on GaAs mesa structures where post-growth annealing showed significant dislocation gettering near mesa sidewalls [20, 21, 22]. In these and similar papers, the influence of mesa structures on dislocation density has been explained by image-force-induced dislocation density reduction.

The application of mesa structures to MCT grown on CdTe/Si has been reported previously. Stoltz, et al. (2011) showed dislocation reduction using 8-10 μm etched cylindrical mesa structures, annealed for 5 minutes at 494°C [23]. They observed significant dislocation reduction and displayed the benefit that reduced dislocation density has on device zero bias resistance-junction area measurements. They postulated that annealing allowed relief of strain and dislocation glide to the sidewall of circular mesa structures. In another study, significant dislocation reduction was observed along the $[0\bar{1}1]$ direction for 20 μm wide mesa bars with lengths greater than 50 μm [8]. Mesa bars along the $[0\bar{1}1]$ orientation produced the lowest dislocation density of $<5 \times 10^5$ $cm^{-2}$ after subjecting the sample to 4 5-minute cycles between 494°C and 250°C, while dislocations along $[\bar{1}11]$ produced very little dislocation reduction. The reasoning for this was that dislocations with orientations of $[0\bar{1}1]$ are repulsed by the sidewalls while $[\bar{1}11]$ dislocations are attracted to the sidewalls and fall off the edge of the mesa sidewall along $[0\bar{1}1]$ direction. The $[0\bar{1}1]$ dislocations will then travel to the end of the mesas until they are influenced by the sidewall at the end of the mesa. This also explains why dislocation reduction is not observed in square mesas of appropriate dimensions.

The problem with using TCA is the elevated temperatures necessary to induce dislocation motion and annihilation. This study looks at determining maximum dislocation reduction with minimal diffusion and further understanding these phenomena. In this paper, the findings of dislocation reduction through the use of mesas on MCT grown on CdTe/Si are studied.

### *4. 1. Mesa: Theory*

The model to develop allows limited dislocation motion in the $[\bar{1}11]$ direction, while allowing significant dislocation motion in the $[0\bar{1}1]$ direction. Dislocation motion in this sense also requires mesa bars with width less than 20 µm and greater than 50 µm in total length oriented along $[0\bar{1}1]$ direction. Letting the mesa edge be approximated as a free surface and the dislocations are screw type a distance, d, along the x-axis from the free surface along the y-axis. For a free surface, the surface stress is zero giving, $\sigma_{xx} = \sigma_{yx} = \sigma_{zx} = 0$ at x = 0. This is satisfied by creating an imaginary screw dislocation at a distance, -d, from the free surface. Then the traditional stress equations for this system are:

$$\sigma_{zx} = -\frac{Ay}{x_-^2 + y^2} + \frac{Ay}{x_+^2 + y^2} \quad 4.1$$

$$\sigma_{zy} = \frac{Ax_-}{x_-^2 + y^2} - \frac{Ax_+}{x_+^2 + y^2} \quad 4.2$$

Where $x_- = x - d$, $x_+ = x + d$, and A = Gb/2$\pi$. The force per unit length in the x direction is given by:

$$F_x = \sigma_{zy} b \quad \rightarrow \quad F_x(x = d, y = 0) = 0 - \frac{A2d}{(2d)^2} b$$
$$= -\frac{Ab}{2d} = -\frac{Gb^2}{4\pi d} \quad 4.3$$

The shear modulus is 31 GPa and Burger's vector is 4.853Å. The stress induced is on the order of tenths of MPa to 2 MPa for a distance between 12 µm to 1 µm. With the critical shear stress for dislocation motion being ~3MPa, the dislocation will not be significantly influenced by image forces until it is within a couple microns from the sidewall. The fact

that there is an angular dependence and that the dislocation reduction is only observed in long bar mesas also rules out the dislocation reduction due to image forces. Therefore, the reduction observed is not induced by attractive image forces from the sidewall acting on dislocations and there must be another factor that causes the angular dependence on dislocation reduction.

Assuming that the reduction in dislocation density is only due to dislocation-dislocation interaction and that the dislocations are repelled by the sidewall, then there is a specific area of interaction that the dislocation will clear out. A single dislocation moving towards another dislocation on a parallel slip plane will interact if they come within an annihilation radius, $r_A$, of one-another, which is approximately 0.7 μm [16]. Therefore, a single dislocation can clear out a parallelogram area of width $r_A$, and will interact with all dislocations along the $[0\bar{1}1]$ direction. This can be seen in Figure 19 for an arbitrary angle, long bar mesa structure.

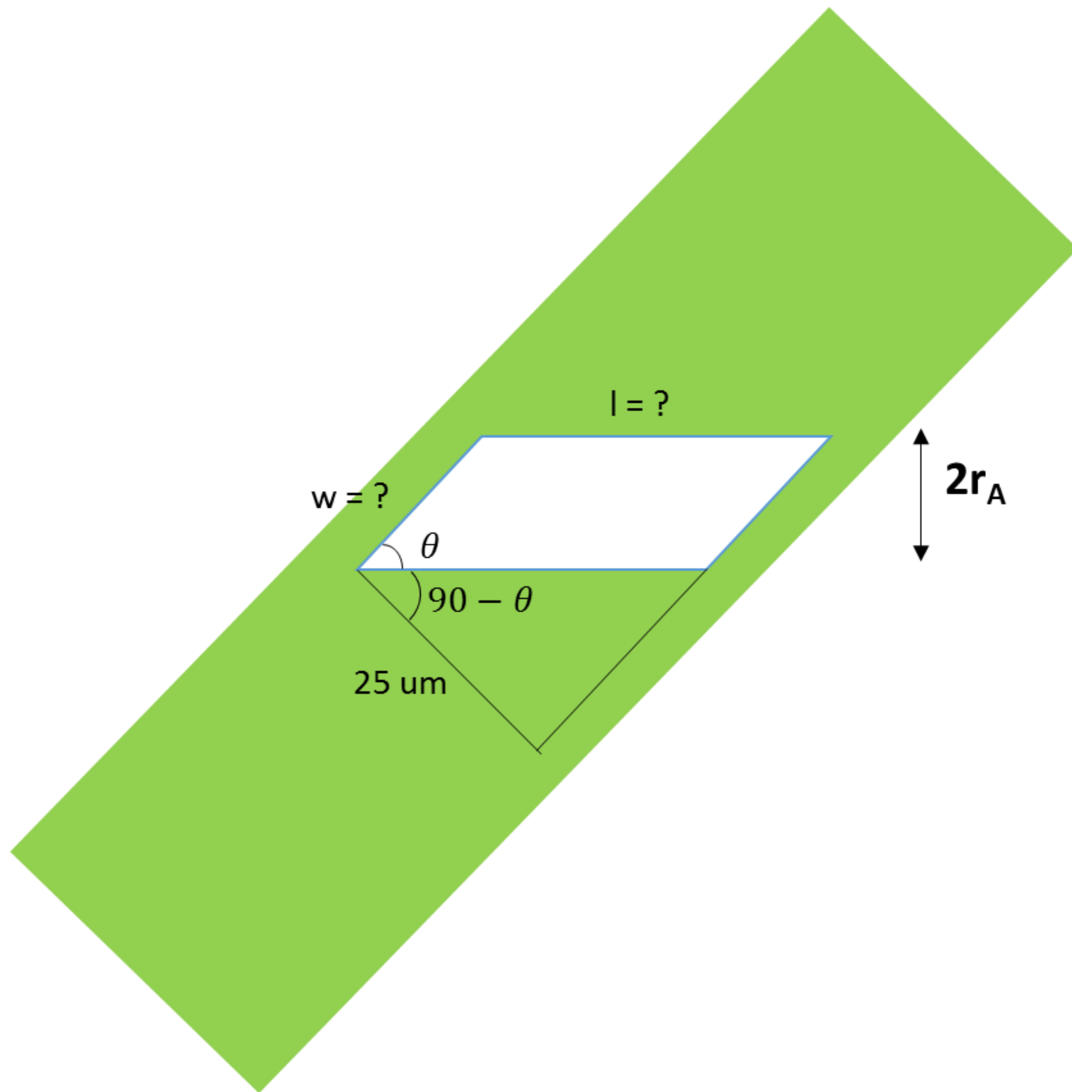


Figure 19. Area of interaction for a dislocation travelling in the [0-11] direction.

The angle of the mesa structure is known and the width of the mesa bar is known, so the length of the parallelogram can easily be determined. From this basic geometry, the length, l, can be determined by:

$$\cos(90-\theta) = \frac{t}{l} \rightarrow l = \frac{t}{\cos(90-\theta)} = \frac{t}{\sin(\theta)} \qquad 4.4$$

The width of the parallelogram is always $r_A$. Therefore, the total area, A, is given by:

$$A = l \times w = t \times \frac{r_A}{[\sin(\theta)]} \qquad 4.5$$

This equation gives the area a single dislocation clears out. The dislocation density is the inverse of A, or:

$$EPD = \frac{1}{A} = \frac{\sin(\theta)}{t \times r_A} = \sin(\theta) \times 2.857 \times 10^7\ cm^{-2} \qquad 4.6$$

This provides a good theoretical explanation for the angular dependence of dislocation density observed in etched mesa annealing of MCT.

### *4. 2. Mesa: Experiment*

Samples of various compositions of MCT were grown in a 3” DCA ultra high vacuum molecular beam epitaxy chamber on CdTe/Si substrates. The MCT samples were processed using a mask containing various structures and orientations including diamonds, squares, rectangles and circles [23]. Samples were etched with an Oxford 100 inductively coupled plasma (ICP) system utilizing a 10% Hydrogen/balance Argon gas plasma mixture etching the sample at a rate of 0.25 μm/min. Etch depths were varied between 4 and 8 μm. After etching, the resist was stripped and the samples solvent cleaned. The samples were then annealed in a sealed, evacuated quartz ampoule under mercury ambient. The samples were slowly heated from room temperature and annealed for 5 minutes at their respective set point temperatures in a Lindbergh 3-zone furnace with computer controlled recipes.

Dislocation decoration was conducted by etching the samples for 10s in 0.1% Bromine-Methanol and the Schaake etchant for 15s [24]. Dislocations were counted manually using a Leica INC20 microscope under bright field mode and confirmed using a scanning electron microscope.

### *4. 3. Mesa: Results and Analysis*

The first annealing attempt was to repeat the previous result by Farrell et al. of four 5-minute cycles between 500°C and 250°C with mesas of MCT on CdTe/Si etched to the substrate (~8 μm). This was successful in reproducing the angular dependence of dislocation density along 20 μm wide, long bar mesas to a minimum dislocation density of $2x10^5$ $cm^{-2}$. The next attempt was to reduce the number of cycles by conducting a single anneal of 5 minutes at 500°C. This was also successful in producing dislocation reduction dependent on mesa bar angle, but only to a minimum dislocation density of ~$1x10^6$ $cm^{-2}$ in 20 μm wide, long bar mesas along the $[0\bar{1}1]$ orientation. With this result, the goal shifted to minimize the temperature under one 5-minute anneal and very similar results were observed at 400°C. A 5-minute anneal at 370°C was unsuccessful at producing the dislocation reduction on mesa bars. The resulting dislocation density is well matched to the model presented in section 4. 1. as seen in Figure 20.

To determine the absolute limit to dislocation reduction, a sample was annealed for 3 hours at 500°C then for 18 hours at 250°C. The model fits well to the measured EPD at large angles away from the $[0\bar{1}1]$ orientation. The deviation from the model at low angles is assumed to be due to more complex interactions like fusion rather than annihilation

interactions. The dislocation density of the perpendicular, $[\bar{1}11]$ orientation is limited due to the apparent formation of grain boundaries along the center of the bar, where dislocations form a line.

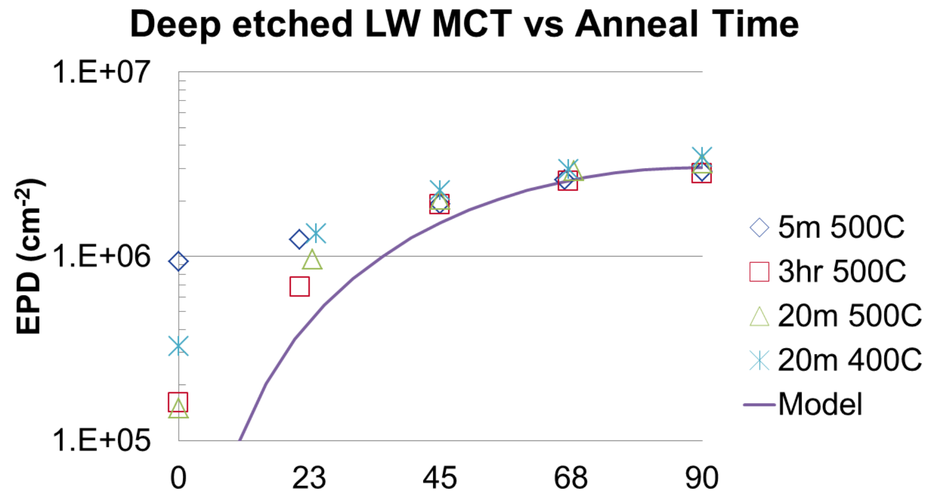


Figure 20. Dislocation density with variation in long bar mesa orientation. 4 cyc refers to 4 5-minute cycles at the high temperature. “Deep” refers to 8 µm etch depth.

The 400°C result is odd, because it indicates that the dislocation activation energy is very low. Extracting the rate constant from equation 3.11, the activation energy calculated from 400°C to 500°C to be only 0.16 eV! This is quite a deviation from the observed dislocation activation energy in planar MCT of 0.93 eV. Also, this is not limited by a saturation dislocation density as is seen in annealing of planar MCT on CdTe/Si since

longer time and higher temperatures produce lower dislocation densities than is seen in the annealing of planar MCT.

Varying the etched depth of the mesa structures was also found to have a significant effect on dislocation density reduction. The attempts were repeated with the MCT layer only etched to a depth of 4 μm to determine its effect on the annealing results as compared to 8 μm etch depth. Anneals of 5 minutes at 500°C reproduced the same results as deeply etched mesas, but anneals of 5 minutes at 400°C and 450°C did not produce any reduction in dislocation density. Therefore, the energy necessary to induce dislocation motion in [0-11] orientation mesa bars varies with etched depth. This provides an intriguing issue regarding image forces. If image forces were the reason for dislocation motion, then the depth should not be of significant consequence.

An additional model must be formulated to determine the influence of mesa height on dislocation reduction. Consider the simplistic case of two types of dislocations with Burgers vector and line direction of $[0\bar{1}1]$ and $[\bar{1}11]$, which shall be refered to as $\alpha$ and $\beta$ dislocations, respectively. The etching of mesa structures cuts the dislocation line. This causes a significant force on $\beta$ dislocations to getter to the sidewalls and annihilate. This leaves $\alpha$ dislocations free to move without other oriented dislocations blocking their paths. This can be used to explain the dislocation density reduction observed in 8 μm etched mesa structures along the $[0\bar{1}1]$ direction. Now, if the etched depth is less, as in the case of 4 μm etch depth, the threading dislocation line will not be cut short and the image force exerted on the dislocation will not overcome the line tension. This will cause the activation energy

to increase and not allow dislocation reduction at lower temperatures. Figure 21 provides a model for explaining this process. Dislocation reduction with bar angle away from the $[0\bar{1}1]$ direction is shown in Figure 22. In the figures, shallow refers to 4 μm and deep refers to 8 μm etch depth.

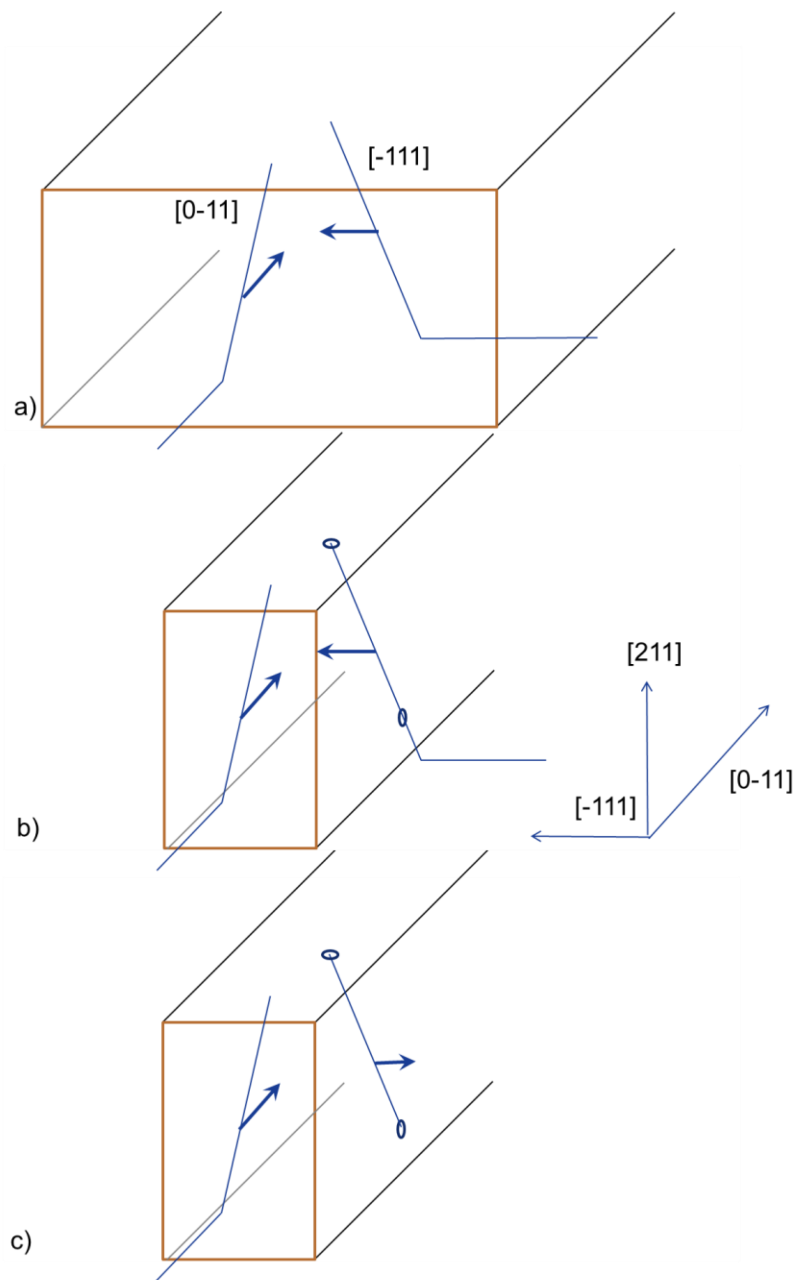


Figure 21. Figures representing dislocations with arrows giving direction of travel. a) Planar dislocation interactions with type $\boldsymbol{\alpha}$ and $\boldsymbol{\beta}$ dislocations. b) Mesa being defined and cutting the dislocation line. c) Dislocation motion after mesa is etched.

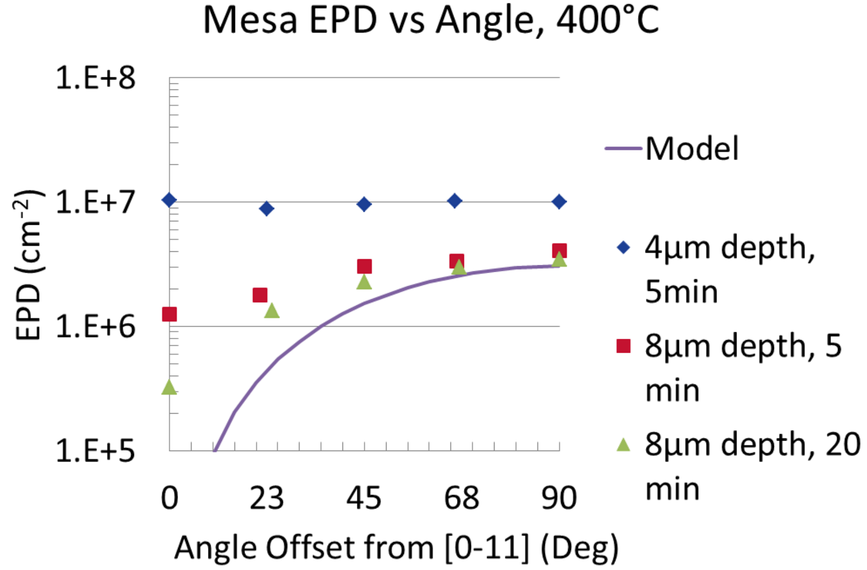


Figure 22. 20 µm long bar mesa EPD variation with angle away from [0-11] orientation

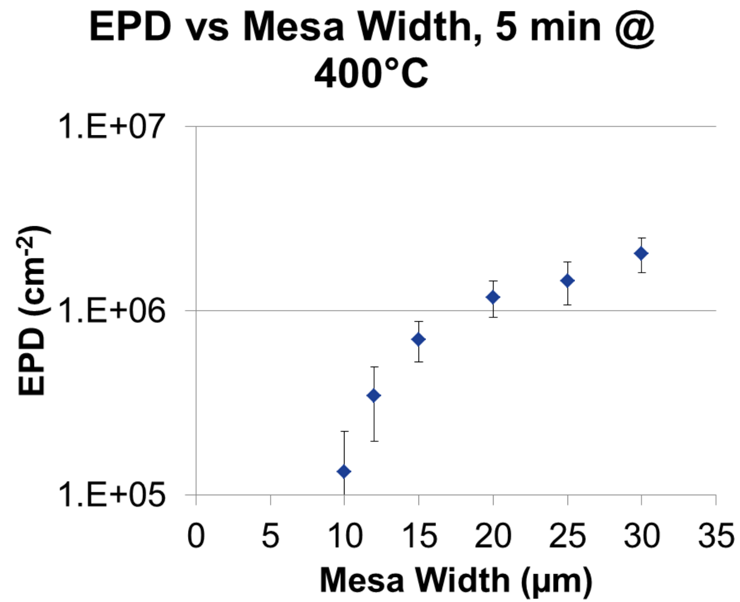


Figure 23. Variation in EPD with mesa thickness. Mesa oriented along [0-11] direction.

There is also a dislocation density reduction relative to the mesa width. With decreasing mesa width, there is decreasing dislocation density in mesa bars along the $[0\bar{1}1]$ orientation, as the image force acting on dislocations is much greater with increasing proximity to the free surface. This can be seen in Figure 23. The dislocation density of the smallest width, 10 μm, bars achieved dislocation densities less than $3x10^5$ $cm^{-2}$ for MCT mesa etched to the substrate and annealed for only 5 minutes at 400C! This can be due to a greater number of non-$\alpha$ dislocation lines being cut and inducing them to getter to the sidewall.

The comparison of 4 5-minute cycles to 1 20-minute anneal showed that cycling does improve crystalline quality slightly beyond a single anneal, but not to the same degree of variance as is seen in planar TCA. A comparison between 5 1-minute cycles and one 5-minute cycle was also analyzed with an anneal temperature of 400°C, but cycling did not provide a noticeable enhancement in dislocation density reduction. Therefore, the application of TCA to long bar mesa structures is limited and likely not useful due to the added time and complication TCA provides.

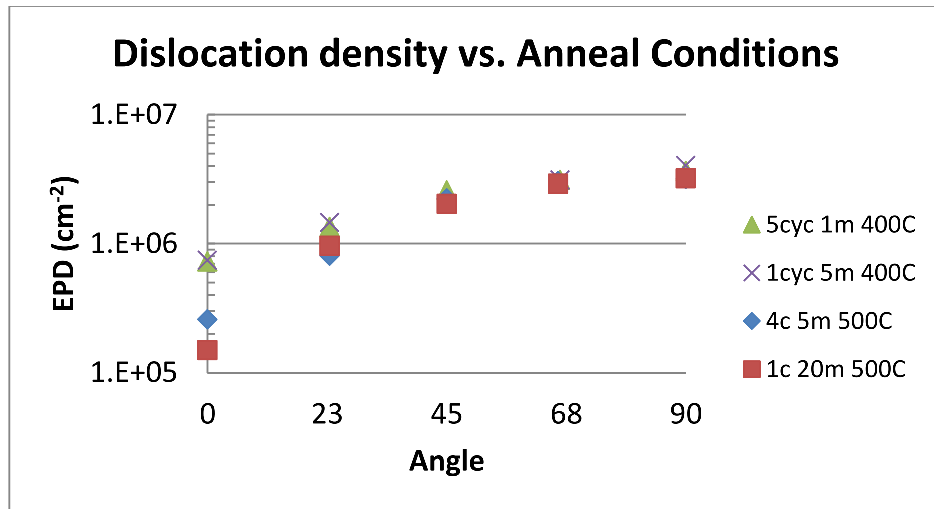


Figure 24. Effect of TCA with various conditions.

With these results, the next analysis is to determine where the dislocations end. The goal is to get the dislocation away from the device p-n junction that will be formed and as far down the sidewall as possible. The sidewall is binned into 3 sections to determine the final position of dislocations as outlined in Figure 25 and pictured in Figure 26. The expectation is that the dislocations that end on the sidewall fall off the edge of the sidewall and this is confirmed in Figure 26, where the dislocations may have dropped off the edge of the mesa and moved to the bottom corner of the mesa structure. Figure 27 shows the density within the three bins and there is a correlation of this trend for the orientation of mesa structures at low angles from the $[0\bar{1}1]$ direction. In Figure 28, we looked at the various mesa bar width sidewalls and observe the same trend in dislocation density among the different widths for 10, 12, 15 and 20 μm wide bars. These results make the application of mesa bar structures to devices for enhanced dislocation reduction very appealing.

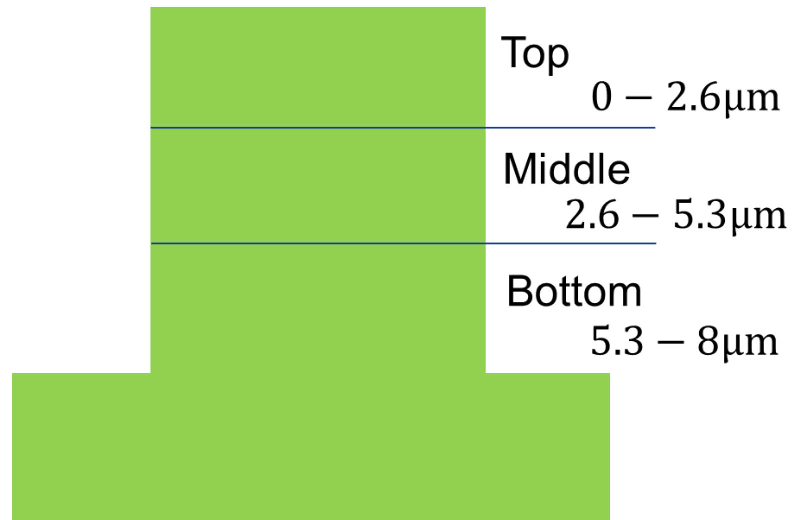


Figure 25. Mesa structure showing bins for dislocation categorizing

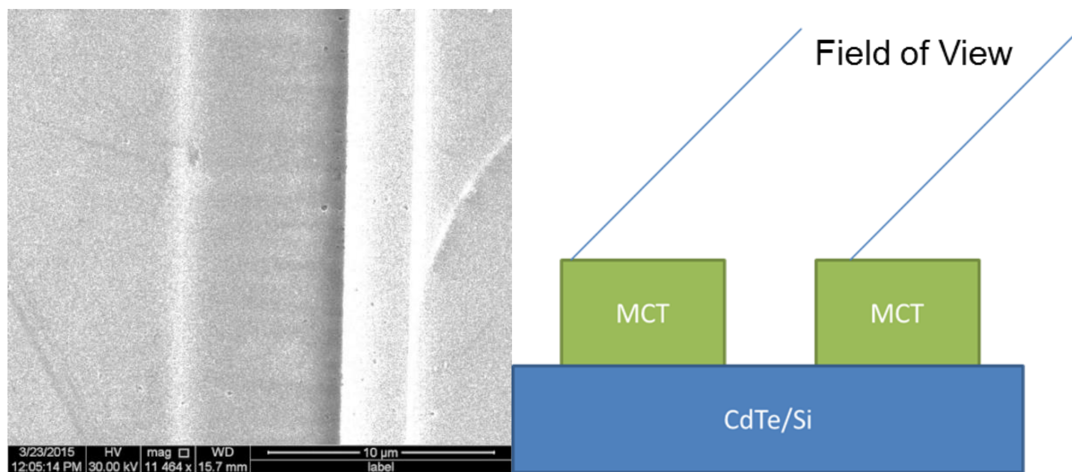


Figure 26. 45 degree angled view of sidewall of 25um mesa along [0-11] orientation.

Right shows a cross-section with the field of view of the picture.

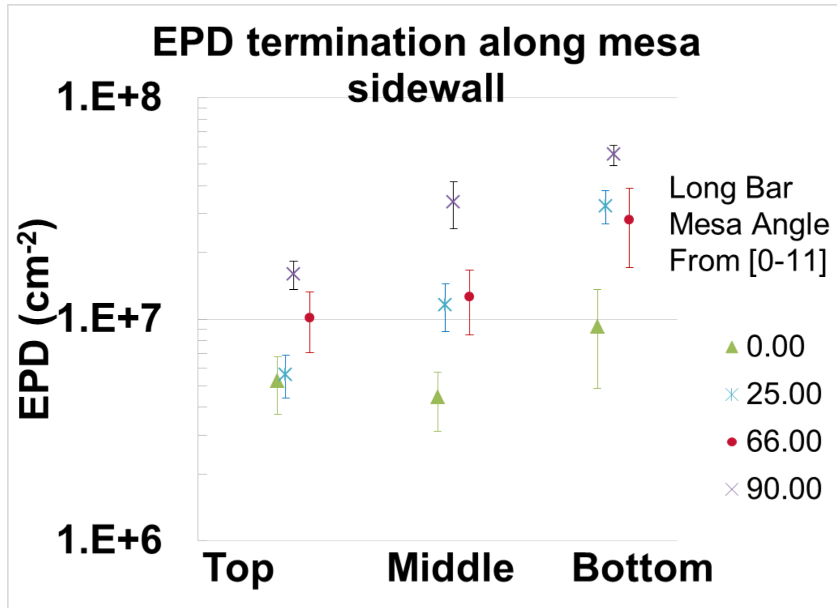


Figure 27. Dislocation density along sidewall for various angles from [0-11] orientation of 20 µm wide mesa structures.

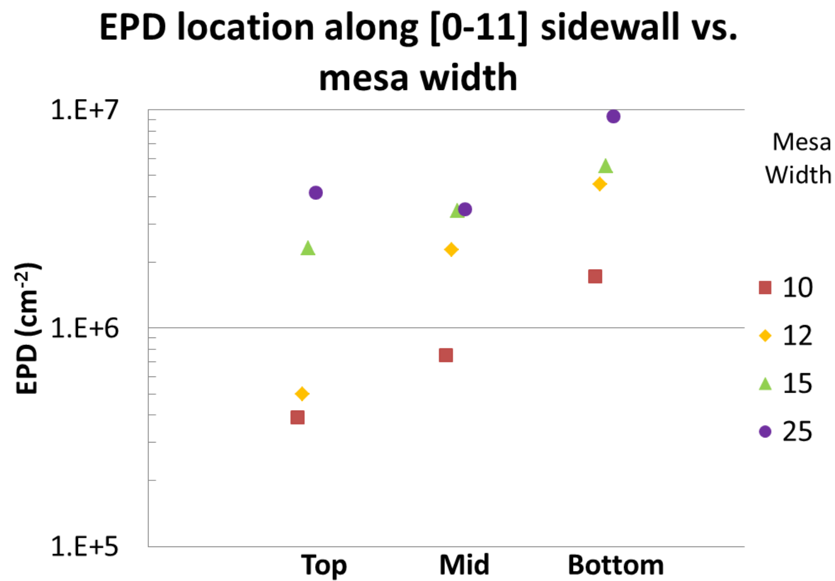


Figure 28. Dislocation density along sidewall of [0-11] long bar mesa structures with varying widths.

### *4. 4. Mesa: Conclusion*

In conclusion, dislocation reduction by the use of long bar mesas has been studied. The dependences on etch depth, mesa width and orientation were also analyzed. The results show that dislocation density is slightly proportional to etch depth. There is a great dependence on mesa width and orientation. The orientation seems to be proportional to a sinusoidal function of the angle away from the $[0\bar{1}1]$ direction. The mesa width allows for greater image force interaction and thinner mesa bars experience significant dislocation reduction while thicker mesa bars have little impact due to dislocation reduction.

# Chapter 5. Devices

The initial goal of this work was to obtain 2.5 μm cutoff with a current density of 1nA/cm$^2$ at 200K. The device analysis campaigns looked at the standard device processing and the effect of incorporating the planar TCA and mesa annealing within processing. Dark current vs. voltage (I-V), quantum efficiency (QE) and spectral response (SR) are used to characterize the diodes. The diode performance is compared to the ideal diode model.

## *5. 1. Devices: Theoretical Background*

Diodes function by limiting current in one direction and allowing current to flow in another direction, referred to as reverse-bias and forward-bias voltage conditions, respectively. Diodes are created by joining p-type, hole rich, and n-type, electron rich, sections of a semiconductor. Due to the electric field created by the electron- and hole-rich semiconductor sections, electrons and holes diffuse into the p- and n-type sections until the electric field is canceled out. This creates a neutral area called the depletion width, W, and is described by the formula:

$$W = \sqrt{\left(\frac{2\epsilon}{q}\right)\frac{N_a + N_d}{N_a N_d}\left(V_{bi} - V_{app}\right)} \qquad 5.1$$

where $\epsilon$ is the permittivity of the semiconductor, q is the electron charge, $N_a$ is the acceptor concentration in the p-type region, $N_d$ is the donor concentration in the n-type region, $V_{bi}$ is the built-in potential and $V_{app}$ is the applied bias. This can be seen in Figure 29. For MCT, the dielectric constant is determined by the equation [3]:

$$\epsilon = 20 - 9.4x \tag{5.2}$$

The built-in potential is given by:

$$V_{bi} = \frac{kT}{q}\ln(\frac{N_d N_a}{n_i^2}) \tag{5.3}$$

where k is the Boltzmann constant, T is the sample temperature, and $n_i$ is the intrinsic carrier concentration. The intrinsic carrier concentration for MCT is given by [3]:

$$\begin{aligned} n_i(T,x) = \ & (5.585 - 3.82x \ + \ (1.7531 * 10^{-3})T \\ & - 1.36411 * 10^{-3}Tx) * 10^{14} \\ & * \ E_g(T,x)^{\frac{3}{4}} * \ T^{\frac{3}{2}} * \ e^{-E_g(T,x)*\frac{q}{2kT}} \end{aligned} \tag{5.4}$$

The measured current under no illumination is known as dark current, $I_{dark}$, and it is a combination of several different current components, as follows:

$$I_{dark} = I_{diff} + I_{g-r} + I_{sh} + I_{tunn} \tag{5.5}$$

Where $I_{diff}$ is diffusion current, $I_{g-r}$ is generation-recombination current, $I_{sh}$ is shunt current and $I_{tunn}$ is tunneling current. The contributions of these currents to the measured dark current allow the determination of the limitations to diffusion-limited performance.

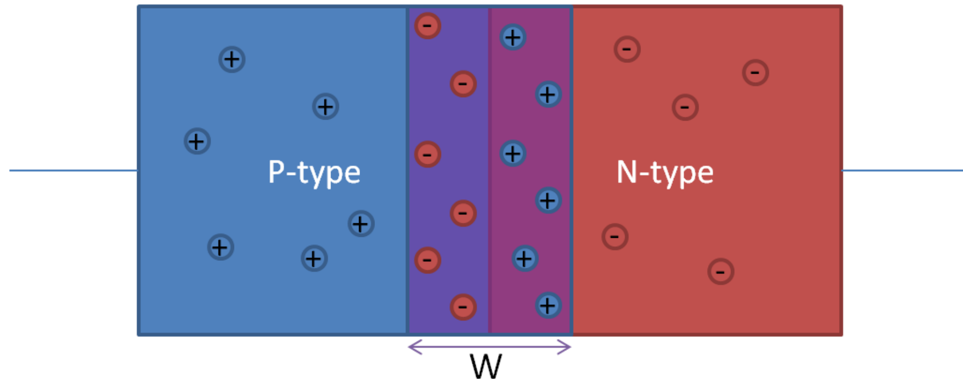


Figure 29. Diode formed by joining a p-type and n-type semiconductors. The depletion width is shown as represented by W.

The I-V characteristic for an ideal diffusion-limited diode with no incident light is given by:

$$\mathrm{I_{diff}} = \mathrm{I_{diff,sat}}\left(\mathrm{e}^{\frac{\mathrm{qV_{app}}}{\mathrm{kT}}} - 1\right) \qquad 5.6$$

where $I_{diff,sat}$ is the saturation diffusion current. For area independent analysis of the diode, the dark current density, $J_{diff}$, is analyzed, $J_{diff} = I_{diff}/A_{junc}$, where $A_{junc}$ is the diode junction area. The standard diffusion current density is described by the equation [25]:

$$J_{diff,sat} = qn_i^2\left[\frac{L_p}{N_d\tau_p} + \frac{L_n}{N_a\tau_n}\right], \qquad 5.7$$

where $J_{diff,sat}$ is the saturation diffusion current density, $L_{p(n)}$ and $\tau_{p(n)}$ is the minority carrier diffusion length and lifetime on the n- and p-side, respectively. The minority carrier

diffusion length and lifetime are the average distance and time an excess charge travels before recombining. The current contribution from the p-side can be neglected since it is a very thin layer with high doping and a wider bandgap. The minority carrier diffusion length, $L_p$, is typically much longer than the absorber layer thickness, d, and can be replaced in the diffusion equation under the short diode approximation, making the equation:

$$J_{diff,sat} = \frac{qn_i^2 d}{N_d \tau_p}, \quad 5.8$$

The minority carrier lifetime has several components that affect the performance of the diode and is given by:

$$\frac{1}{\tau_p} = \frac{1}{\tau_R} + \frac{1}{\tau_A} + \frac{1}{\tau_{SRH}} \quad 5.9$$

Where $\tau_R, \tau_A, and\ \tau_{SR}$ are the radiative, Auger and Shockley-Read-Hall (SRH) lifetimes, respectively. The methods of recombination are depicted in Figure 30. Radiative and Auger recombination are intrinsic properties of the material, whereas SRH recombination is due to defects in the material.

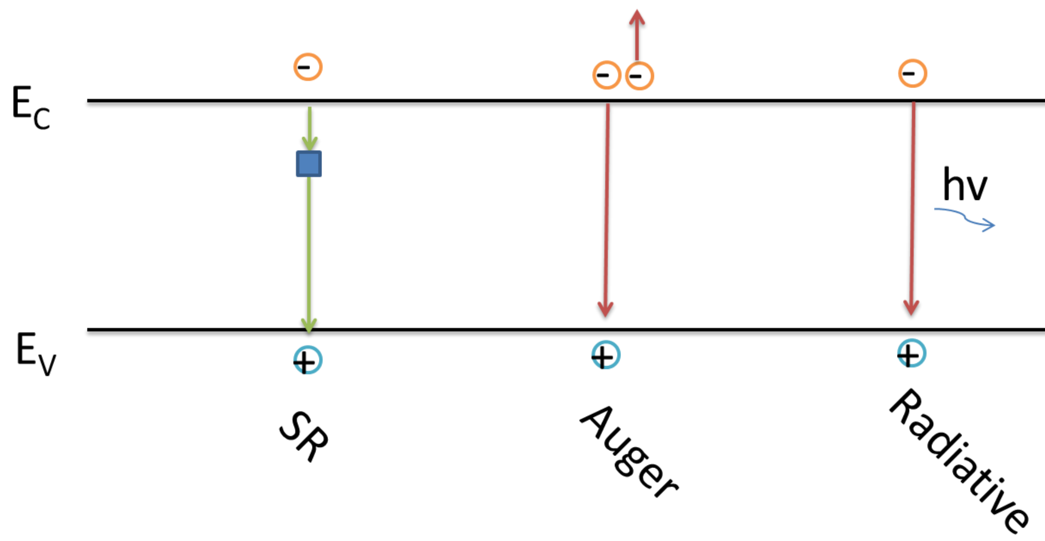


Figure 30. Shockley-Read, Auger, and Radiative recombination methods.

Radiative recombination occurs due to electron from the conduction band combining with a hole from the valence band and giving off a photon. It is described by the equation [25]:

$$\frac{1}{\tau_R} = \frac{1}{B(n_0 + p_0)} \qquad 5.10$$

Where B is a recombination coefficient, and $n_0$ and $p_0$ are the equilibrium electron and hole concentrations. In n-type material, $n_0 + p_0 \approx n_0 = N_d$ when $n_0 \gg p_0$. Therefore, the equation can be reduced to:

$$\frac{1}{\tau_R} = \frac{1}{BN_d} \qquad 5.11$$

For MCT, B is given by [25]:

$$B = 5.8 \times 10^{-13}\sqrt{\epsilon}\left(\frac{m_0}{m_e^* + m_h^*}\right)\left(1 + \frac{m_0}{m_e^*} + \frac{m_0}{m_h^*}\right)\left(\frac{300}{T}\right)^{\frac{3}{2}}\left(E_g^2 + 3kTE_g + 3.75k^2T^2\right) \quad 5.12$$

Where $m_e^*$ and $m_h^*$ are the effective masses of electrons and holes, and $m_0$ is the electron rest mass. The effective electron mass is described by:

$$m_e^* = m_0\left[-0.6 + 6.33\left(\frac{2}{E_g} + \frac{1}{E_g + 1}\right)\right]^{-1} \quad 5.13$$

For MCT with a cutoff of 2.5 µm, the effective electron mass is $0.035m_o$. The effective hole mass is assumed to be $0.55m_o$.

Auger recombination is recombination and transfer of energy to a secondary particle. There are several different Auger processes and the two that dominate in n-type and p-type MCT are Auger-1 and Auger-7 processes, respectively [3]. The Auger-1 process involves an excited electron in the conduction band recombining with a hole in the valence band and transferring the excess energy to a second electron in the conduction band. The Auger-1 recombination lifetime is given as [25]:

$$\tau_{A1} = \frac{2n_i^2\tau_{Ai}}{(n_0 + p_0)(n_0 + \zeta p_0)} \quad 5.14$$

Where $\zeta$ is the hole-hole collision term, which is assumed to be negligible in this analysis, and $\tau_{Ai}$ is the intrinsic lifetime for MCT given by [25]:

$$\tau_{Ai} = \frac{3.81 \times 10^{-18} \epsilon^2 (1+\eta)^{\frac{3}{2}}}{\left(\frac{m_e^*}{m_0}\right) |F_1 F_2|^2 \left(\frac{kT}{E_g}\right)^{\frac{3}{2}}} \times \exp\left(\frac{1+2\eta}{1+\eta}\frac{E_g}{kT}\right) \qquad 5.15$$

Where $|F_1F_2|$ is an overlap integral of the electron orbits with a typical value between 0.1 and 0.3. There are conflicting values to use for this integral. For this analysis, the overlap integral is set to 0.22. The Auger-7 process occurs in the same way but with the excess energy of the electron transferred to a hole. Since Auger-7 processes dominates in p-type material, it is not considered here.

SRH recombination occurs due to a trap level within the bandgap. The trap level allows recombination of electrons and holes with an energy barrier less than the material bandgap. For the case where the number of SRH recombination centers is less than the carrier concentration, the SRH recombination lifetime is given as [25]:

$$\tau_{SRH} = \frac{\tau_{p0}(n_0 + n_1)}{n_0 + p_0} + \frac{\tau_{n0}(p_0 + p_1)}{n_0 + p_0} \qquad 5.16$$

Where $\tau_{n0}$ and $\tau_{p0}$ denote the shortest-time constant values for electron and hole capture and $n_1 = n_0 \exp\left(\frac{E_t - E_F}{kT}\right)$ and $p_1 = p_0 \exp\left(\frac{E_F - E_t}{kT}\right)$ with $E_F$ being the Fermi level. With this information, diffusion-limited behavior can be modeled.

### 5.1.1. Generation-Recombination Current

Generation-recombination (g-r) current arises from several different issues mainly from material defects and surface passivation problems. This gives rise to trap states within the band gap that lead to degraded minority carrier lifetime and increased dark current

density. Following the analysis of Sah, Noyce and Shockley, the current density of g-r is given as [26]:

$$J_{g-r} = \frac{qn_iW}{\sqrt{\tau_{n0}\tau_{p0}}} \frac{Sinh\left(\frac{qV}{2kT}\right)}{\frac{q(V_{bi}-V)}{2kT}} f(b) \qquad 5.17$$

Where

$$f(b) = \begin{cases} \frac{1}{\sqrt{1-b^2}}\left[\operatorname{atan}\left(\frac{z_2+b}{\sqrt{1-b^2}}\right) - \operatorname{atan}\left(\frac{z_1+b}{\sqrt{1-b^2}}\right)\right], b < 1 \\ \frac{1}{z_1+b} - \frac{1}{z_2+b}, \qquad b = 1 \\ \frac{1}{2\sqrt{b^2-1}}[\ln\left(\frac{z_2+b-\sqrt{b^2-1}}{z_2+b+\sqrt{b^2-1}}\right) - \ln\left(\frac{z_1+b-\sqrt{b^2-1}}{z_1+b+\sqrt{b^2-1}}\right), b > 1 \end{cases} \qquad 5.18$$

$$b = \exp\left(-\frac{qV}{2kT}\right)\cosh\left(\frac{E_t-E_i}{kT} + \left(\frac{1}{2}\right)ln\left(\frac{\tau_{p0}}{\tau_{n0}}\right)\right) \qquad 5.19$$

$$z_{1,2} = \sqrt{\frac{\tau_{p0}}{\tau_{n0}}}\exp\left(\mp\frac{(V_{bi}-V)q}{2kT}\right) \qquad 5.20$$

Where $E_t$ is the trap level within the bandgap and $E_{Fi}$ is the intrinsic Fermi level. The intrinsic Fermi level is the average density of states for electrons within the band structure.

To simplify this, we will assume that the trap level, $E_t$, is at the intrinsic Fermi level, $E_{Fi}$, therefore setting $E_t - E_{Fi} = 0$. This is an acceptable approximation since trap levels are most influential when they are at the intrinsic Fermi level. This gives:

$$b = \exp\left(-\frac{qV}{2kT}\right)\cosh\left(\frac{1}{2}ln\left(\frac{\tau_{p0}}{\tau_{n0}}\right)\right) \qquad 5.21$$

After some algebra, the total g-r current at a specific bias can be rewritten as: [2]

$$I_{g-r} = I_{g-r,sat}\sqrt{V_{bi} - V}\left(e^{\frac{qV}{2kT}} - 1\right) \quad 5.22$$

Where $I_{g-r,sat}$ is the saturation g-r current.

5.1.2.Shunt Current

In electronic devices, a shunt is a pathway allowing current to bypass the specified circuitry. In the diodes, the shunt current, $I_{sh}$, is determined by the shunt resistance, $R_{sh}$, with the equations:

$$I_{sh} = \frac{V}{R_{sh}} \quad 5.23$$

Shunt currents can be due to several factors including improper passivation allowing current to pass along the interface and dislocations intersecting the depletion region allowing current to pass through the device. Therefore, the shunt current is the sum of an area dependent current and a perimeter area current giving:

$$I_{sh} = I_1 A_{junc} + I_2 P_{junc} \quad 5.24$$

The shunt current density is then given by:

$$J_{sh} = I_1 + I_2 \frac{P_{junc}}{A_{junc}} \quad 5.25$$

Shunt paths through the passivation occur due to dangling bonds that remain unpassivated at the CdTe passivant/MCT surface and are believed to be a limiting factor in wide bandgap, SWIR MCT. The influence of shunt current is tested through analysis of the dark current against device perimeter/area ratio, as will be shown.

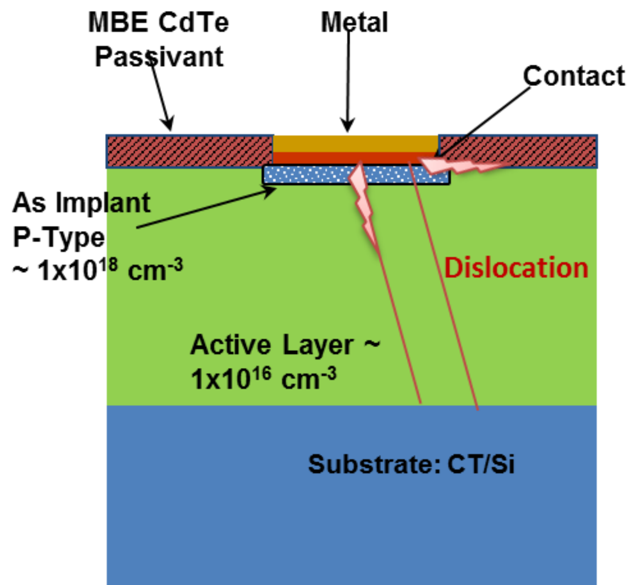


Figure 31. Diode cross section showing the methods of shunt curren path through devices

5.1.3.Tunneling

Tunneling in devices can occur through single step processes known as band-to-band tunneling or tunneling promoted by traps occurring within the band gap known as trap-assisted tunneling. Tunneling components have a smaller impact on SWIR devices due to its inherent wide band-gap, but their effects can creep in at larger reverse bias. Direct band-to-band tunneling at the same energy is interband tunneling. This can be mitigated in designing the diode by using low-doping on one side of the junction to increase the depletion width. Trap-assisted tunneling is caused by an energy trap level with a capture coefficient for minority carriers several times greater than that of majority carriers. Trap-

assisted tunneling can occur through thermal-tunnel, tunnel-thermal or tunnel-tunnel processes [27]. These are shown in Figure 32.

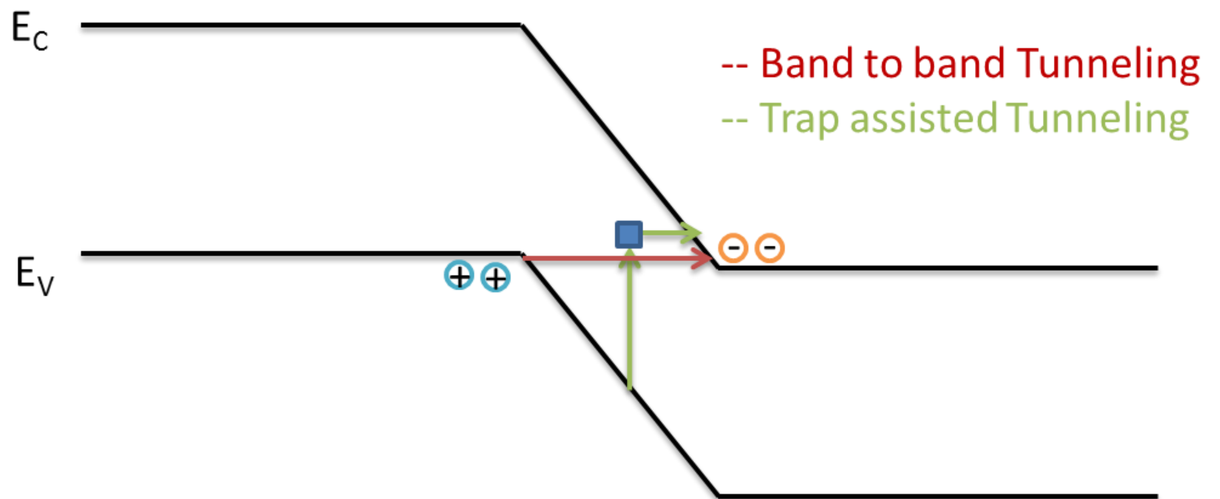


Figure 32. Tunneling current mechanisms displaying band-to-band and trap-assisted tunneling.

Band-to-band (BTB) tunneling is a source of dark current caused by single step tunneling. This is directly influenced by the size of the depletion width. It is described by the following equation:

$$I_{BTB} = \frac{Aq^3EV}{4\,\pi^2\hbar^2}\sqrt{\frac{2m^*}{E_g}}\,e^{-\frac{4\sqrt{2m^*}E_g^{1.5}}{3qE\hbar}}\left(1 - e^{\frac{qV}{kT}}\right) \qquad 5.26$$

Where A is the device area, E is the electric field, V is the applied bias, m* is the effective electron rest mass, $\hbar$ is the reduced Planck constant, and $E_g$ is the bandgap.

Trap-assisted tunneling is described by the equation:

$$I_{TAT} = \frac{A\pi^2 q^2 m^* E M^2 N_t W}{h^3(E_g - E_t)} \sqrt{\frac{2m^*}{E_g}} \left[ e^{-\frac{\pi\sqrt{\frac{m^*}{2}} E_g^{1.5} F(a)}{qEh}} \right] \times \left(1 - e^{\frac{qV}{kT}}\right) \quad 5.27$$

Where $N_t$ is the trap density, F(a) is a function of $E_t/E_g$, M is the transition matrix element, E is the electric field, and $\hbar$ is the reduced Planck constant. For an abrupt junction of the p-n diode, the electric field is approximately given by:

$$E = \frac{V_{bi} - V}{W} \quad 5.28$$

The function F(a) is given by:

$$F(a) = \frac{\pi}{2} + \sin^{-1}(1 - 2a) + 2(1 - 2a)\sqrt{a(1 - a)}, \quad with\ a = \frac{E_t}{E_g} \quad 5.29$$

. The value of $M^2\left(\frac{m^*}{m_0}\right)$ is approximated as $10^{-23}$ V cm$^3$ for MCT modeling and fitting.

## *5. 2. Devices: Modeling*

The design of the device is critical for device performance. The absorber layer thickness and carrier concentration have an especially significant impact on device

characteristics. Below, the variations and impacts over several different device parameters are analyzed to determine the optimal device properties. The device design goal is to minimize the dark current while maximizing quantum efficiency.

The standard device structure for MCT photovoltaic diodes begins with the formation of an intentionally doped n-type MCT layer grown by molecular beam epitaxy with indium and a p-type layer formed by ion implantation with $As^+$ ions. The device structure is shown in Figure 33. In Figure 34, the green line shows the arsenic doping profile from the implant and the blue line shows the indium doping that is held constant throughout the growth. Figure 35 shows a cross section of the ideal device design.

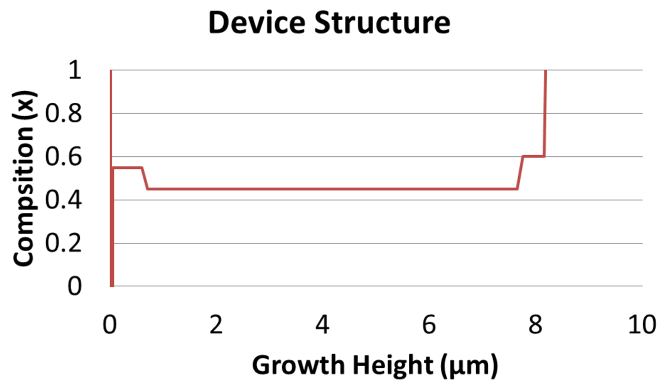


Figure 33. As Grown Device Structure. Growth Height of 0 corresponds to substrate surface.

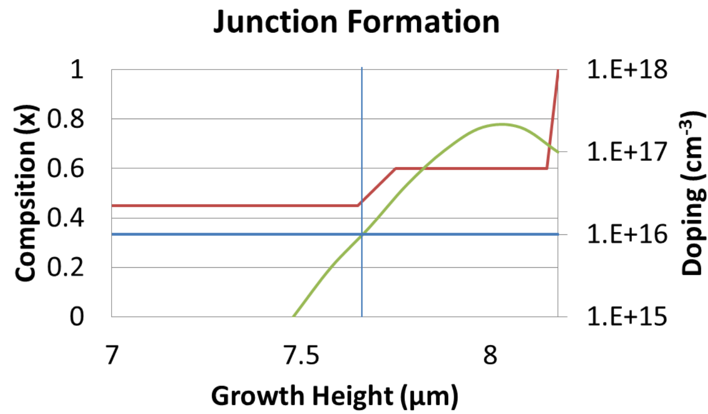


Figure 34. Junction location. Blue vertical line shows center of depletion width. Red line represents device structure. Horizontal blue line is the indium doping level. Green line is the arsenic doping profile.

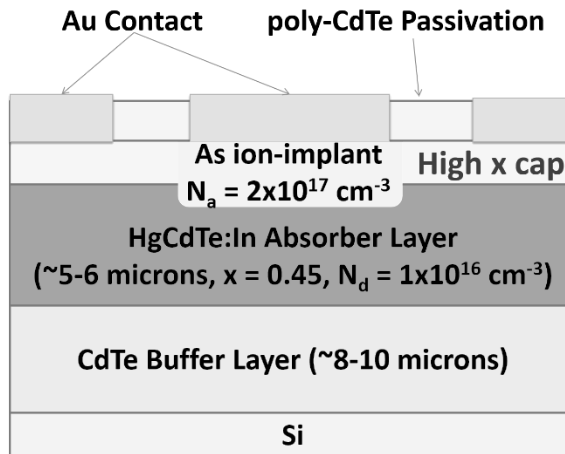


Figure 35. Device Cross Section

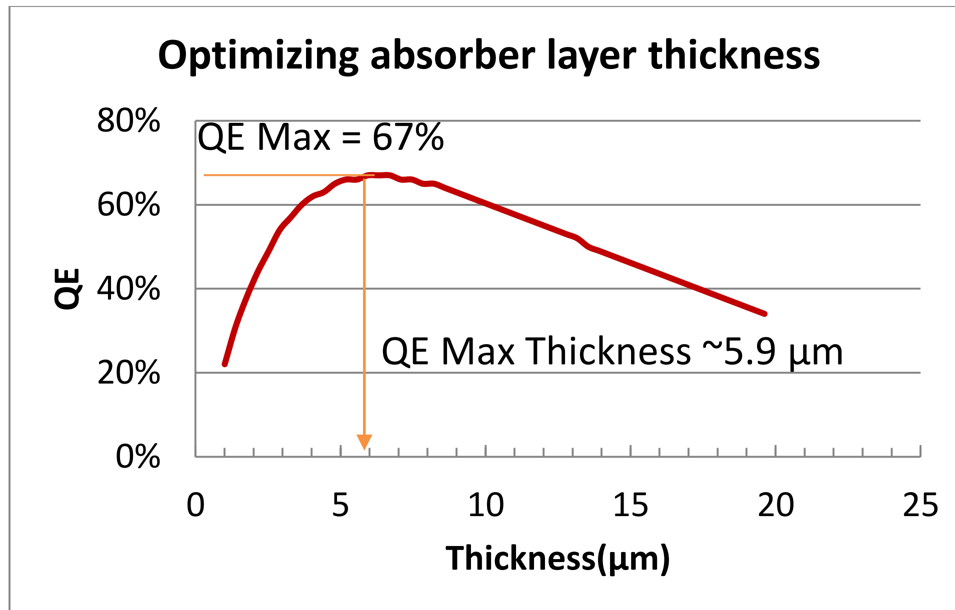


Figure 36. Quantum efficiency as a function of thickness

The absorber layer thickness mainly affects the quantum efficiency and dark current. The dark current density, $J_d$, is directly proportional to the absorber layer thickness. But, the layer also needs to be thick enough to absorb the incident light, thereby increasing the quantum efficiency. In Figure 37 and Figure 39, the effect of thickness on quantum efficiency is shown. The peak quantum efficiency is approximated as the inverse of the absorption coefficient, giving a 5.92 µm thick absorber layer. As shown in Figure 37, a thin layer has poor absorption near the cutoff while a thick layer has a sharp cutoff but lower peak quantum efficiency. The quantum efficiency increases as the thickness increases until the recombination of carriers begins to take over as the sample becomes too thick.

Doping of the semiconductor is also critical to the final device performance. The doping affects the size of the depletion width, which affects the influence of g-r and tunneling in devices as well as causing variations in device properties like minority carrier lifetime and collection length. The variation of QE with doping is shown in Figure 38. Optimal doping is shown to be in the high $10^{15}\ cm^{-3}$ range.

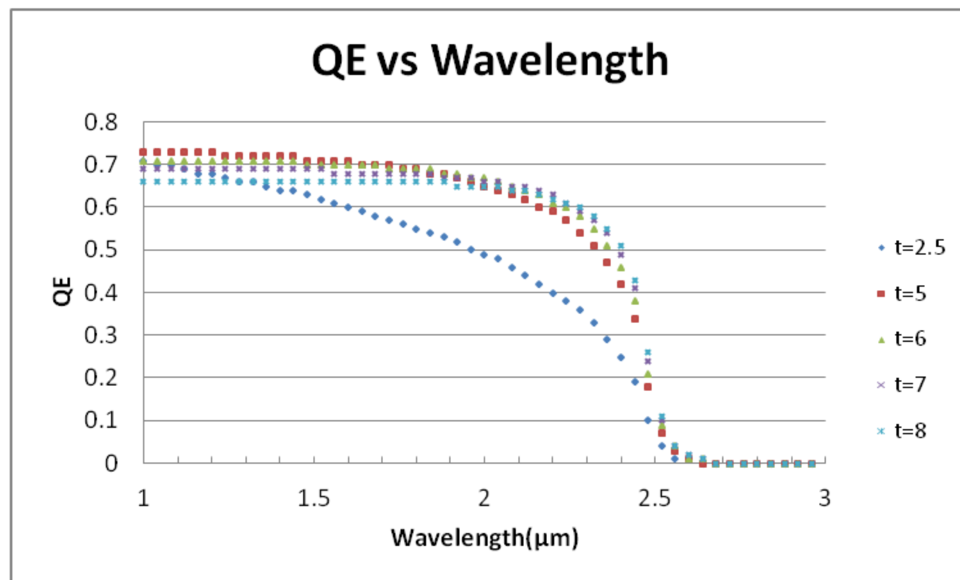


Figure 37. QE vs absorber layer thickness.

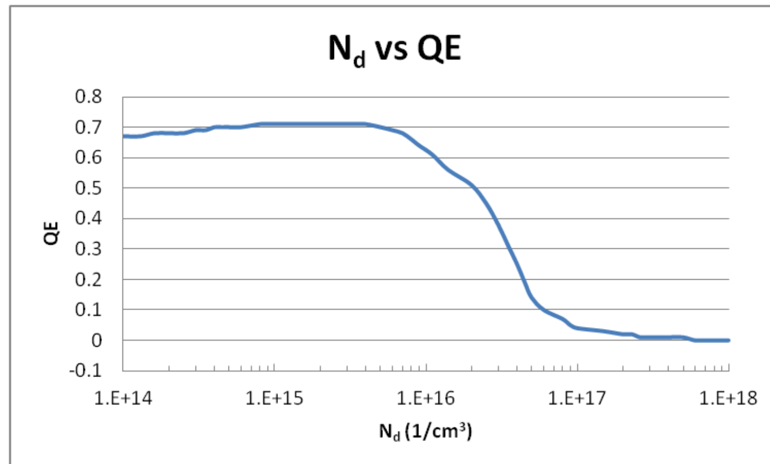


Figure 38. Variation in QE with doping density

*5. 3. Devices: Experiment*

For all of the samples tested, indium doped MCT epilayers are implanted in selective areas with arsenic at a dose of $1x10^{13}$ and intensity of 350keV to form the doping profile in Figure 34. The samples are annealed in sealed ampoules under Hg ambient conditions with the standard activation anneal at 400°C, an overnight anneal at 250°C and then slowly cooled down to room temperature. The samples are then passivated with 0.5 µm of polycrystalline CdTe. Contacts are made by selectively etching the passivation layer and metallizing with Ti/Au. Selective areas are formed with standard semiconductor processing techniques including photoresist and liftoff. The samples are then loaded into a 68-pin leadless chip carrier (LCC) and wire bonded with In balls and Au wire for device analysis.

The LCC was loaded into a continuous flow Lakeshore MTD-150B modular test dewar with individual BNC break-outs for each wire-bonded device. The spectral response measurements for the device were performed with a Nicolet 8700 Fourier transform infrared (FTIR) spectrometer in conjunction with a low-noise Keithley 428 trans-impedance preamplifier set at a gain of between $10^6$ and $10^8$ V/A and recorded with OMNIC software. A FTIR calibration technique is used to provide the accurate relative spectral shape for the device under test (DUT). QE measurements were performed by illuminating the sample through a narrow band-pass filter centered at 1.997 µm, with a full-width, half-maximum of ~24nm. This allows control of the flux density delivered by a chopped, apertured, 800K cavity blackbody mounted a fixed distance from the DUT. The chopped DUT signal is fed into a Stanford Research Systems SRS SR830 digital lock-in amplifier to determine the root-mean-square device current output based on the available chopped flux density to the DUT. This information, in addition to the form factor of the blackbody allows the calculation of the external QE, which can then be applied to the normalized per-photon spectral response to correct for the QE versus wavelength.

From measuring the QE of different radii diodes, the optical collection length that influences the effective diode area can be determined. The formula is given as [28]:

$$\eta = \eta_{1D}\left(1 + \frac{L_c}{R_j}\right)^2 \qquad 5.30$$

Where $\eta_{1D}$ is the one dimensional quantum efficiency, $L_c$ is the collection length and $R_j$ is the junction radius.

The spectral response is a measurement of response of incident infrared radiation across a waveband. The responsivity is given by the following equation:

$$R_\lambda = \frac{q\eta\phi A}{Nh\nu} = \frac{q\eta\phi A}{A\phi h\nu} = \frac{q\eta}{h\nu} = \frac{q\eta\lambda}{hc} \propto \lambda \qquad 5.31$$

Where $\phi$ is the flux, $\eta$ is the quantum efficiency, $\lambda$ is the wavelength, h is Planck's constant, and c is the speed of light. The proportionality allows for immediate qualitative judgment of good response. A linear response represents proper performance with no other internal influences. A bending response near the cut-on and cut-off wavelengths can be modeled due to front or rear surface recombination, respectively.

### *5. 4. Devices: Results*

The device characteristics of the planar device tested is shown in Table 4. In I-V measurements, the large devices are limited by diffusion and g-r current contributions. In the impedance-area ($R_0A$) vs. voltage measurements, the smaller devices have higher tunneling and g-r contributions, leading to decreasing impedance-area with increasing reverse bias. This can be seen in Figure 49 and Figure 50. These devices are fit to the several different current components. The $J_d$-V measurements of various diameter diodes is shown in Figure 39 and their corresponding impedance-area vs. voltage is shown in Figure 40.

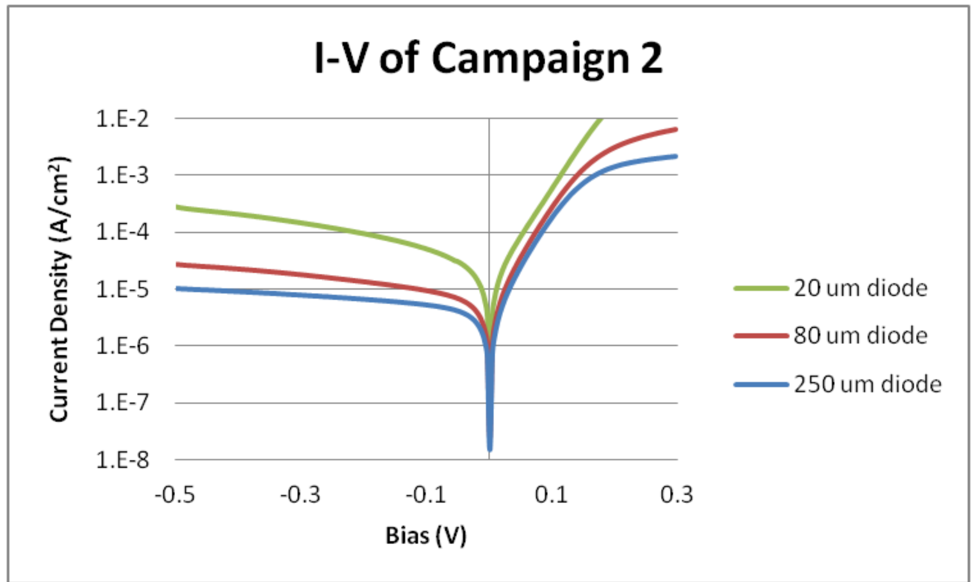


Figure 39. Current-Voltage measurements of various diameter circular diodes on MC0074

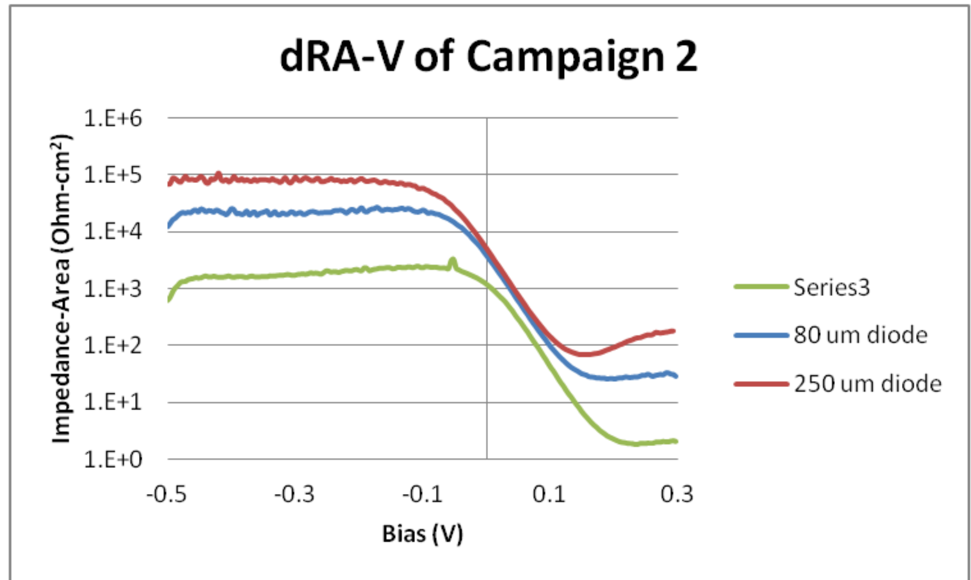


Figure 40. Impedance area-Voltage measurements of various diameter circular diodes on MC0074

Table 4. Device material characteristics

| Sample | x-value | Cutoff wavelength, λ (μm) | Absorber Thickness (μm) | Indium Carrier Concentration (300K) ($cm^{-3}$) | Mobility (300K) ($cm^2/Vs$) |
|---|---|---|---|---|---|
| MC0074 | 0.48 | 2.25 | 7.41 | $9.70x10^{15}$ | 1617 |

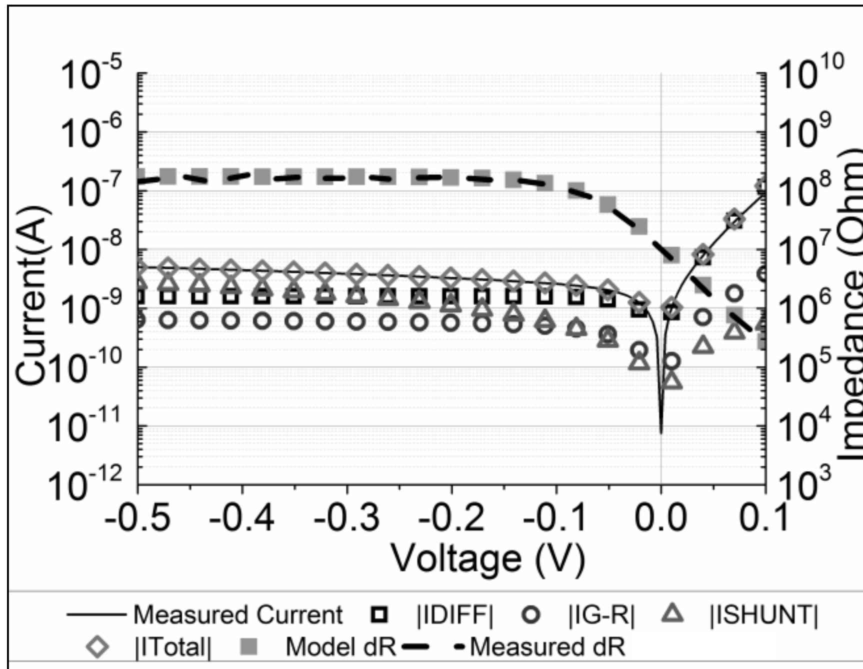


Figure 41. Modeling of current components of 250μm diameter diode

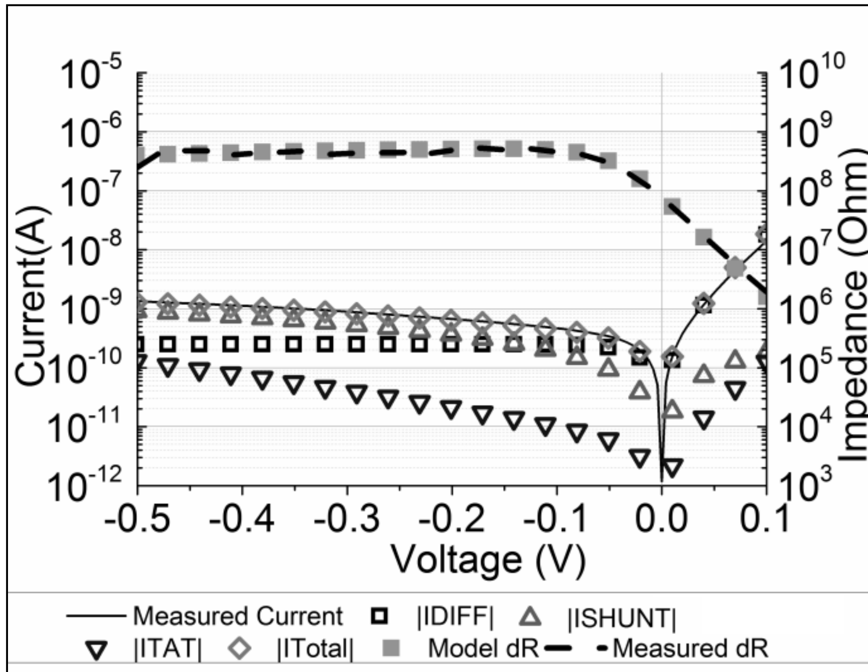


Figure 42. Modeling of current components of 80μm diameter diode

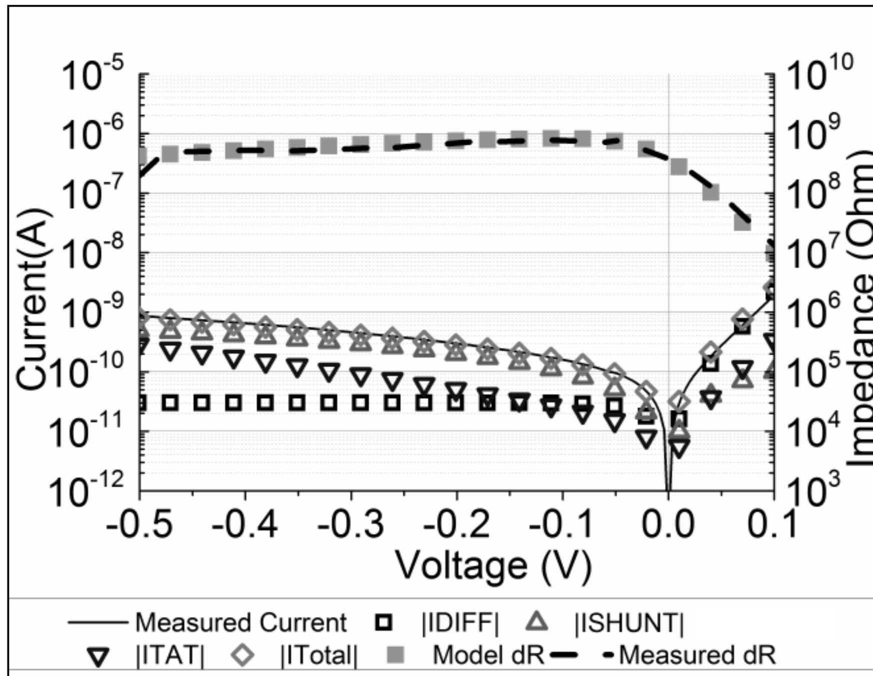


Figure 43. Modeling of current components of 20μm diameter diode

The diodes were fit with diffusion, g-r, and shunt currents and can be seen in Figure 41, Figure 42, and Figure 43. There is a significant increase in shunt current contribution to the overall measured dark current with decreasing size. Since the shunt current can occur due to passivation not tying up all of the dangling bonds at the semiconductor/passivant interface, the device can be subjected to hot plate baking to diffuse the passivant and tie up the dangling bonds. The results of heating the sample to 80°C for 3 hours are shown in Figure 44. Dark current reduces by a factor of 2 at near 108 minutes. After this time, diffusion of the gold contact through the p-type region increases the shunt current through the diode, leading to higher dark current.

The shunt current component can be analyzed with Equation 5.25. The dark current density is fairly linear and varies with a slight slope with size of diode for all but the smallest, 30 µm and 15 µm devices. Excluding the small diodes, the perimeter current contribution is $4\times 10^{-8}\ A/cm^{-2}$, which is nearly three orders of magnitude less than the area dependent current of $3 \times 10^{-5}\ A/cm^{-2}$. Adding these smaller diodes skews the data in such a way that the perimeter contribution is the main current contribution. This is further proof of the significant perimeter-dependent shunt current observed in smaller diameter diodes. After baking, as long as the gold contact does not diffuse, the device performance can improve, as seen by the post-bake results for the small diode in Figure 45.

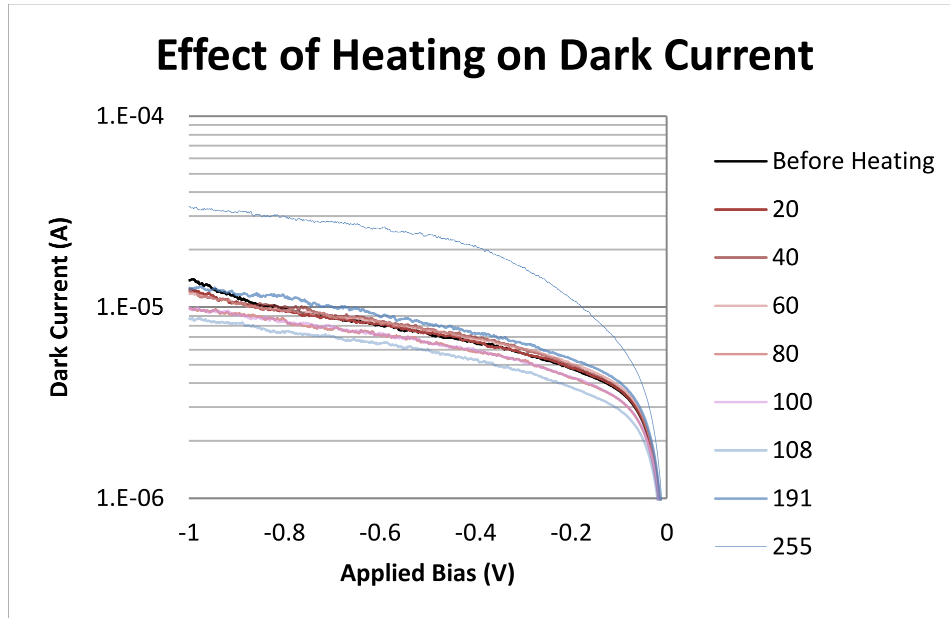


Figure 44. Dark current variation with time heated at 80°C. Minimum achieved at 108 minutes with factor of ~2 reduction.

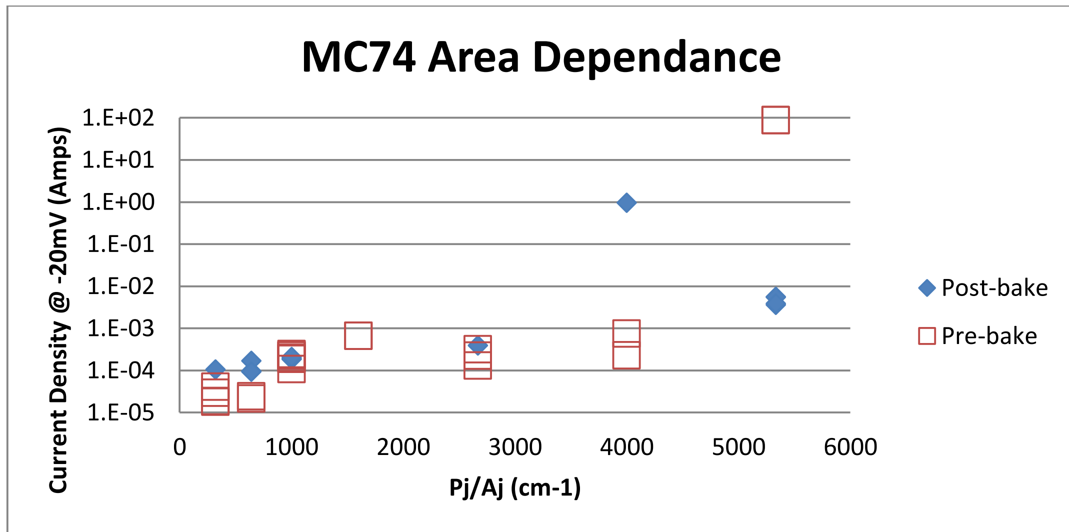


Figure 45. Perimeter over Area plot of dark current density at -0.2V and room temperature to determine shunt current contribution.

Quantum efficiency is measured with various radii diodes to determine the collection length. The square-root operation on the $\eta$ equation in the previous section results in $\sqrt{\eta} = \sqrt{\eta_{1D}}\left(1 + \frac{L_c}{R_j}\right)$. The results are shown in Figure 46. The vertical axis intercept of $\sqrt{\eta}$ vs $1/R_j$ plot gives the material quantum efficiency, $\eta_{1D}$, of 44%. An $L_c$ calculated from the slope of $\sqrt{\eta}$ vs $1/R_j$ plot is 29.4 µm. Due to this larger collection length, the measured quantum efficiency on the planar diodes is "greater" than the material quantum efficiency, as the size of the collection length is on the same order as the junction radius of the smaller devices. A representation of this can be seen in Figure 47. The measured quantum efficiency of various diodes when taking into account the optical area is 44%, as expected.

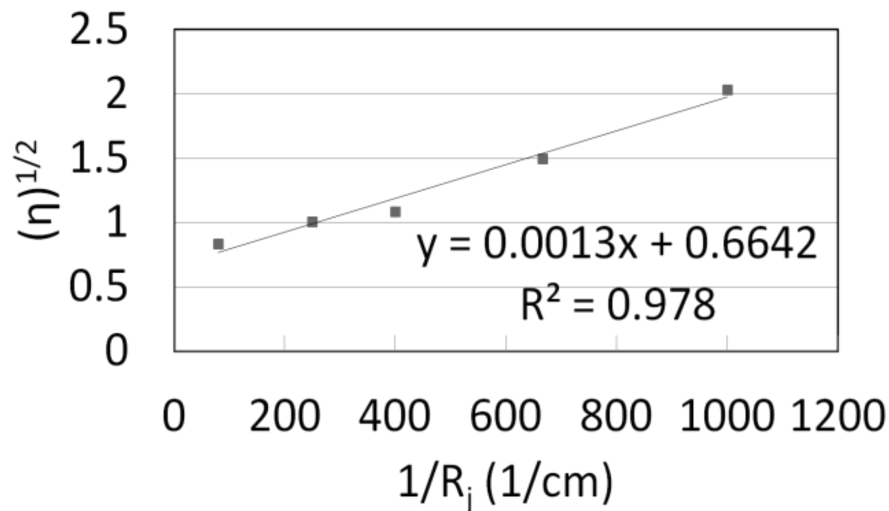


Figure 46. $\sqrt{\boldsymbol{\eta}}$ vs. $1/R_j$ to determine $\eta_{1D}$ and collection length, $L_c$.

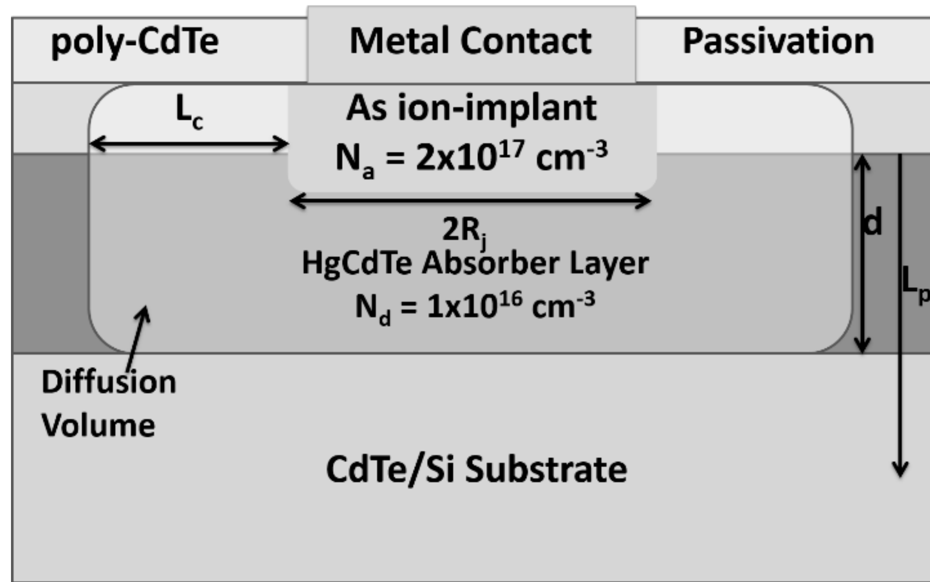


Figure 47. Device cross section displaying the influence of collection length on the active device volume.

By considering only radiative and Auger lifetimes, the model of the diode gives a QE of approximately 66% with a lifetime of 1.45 μs, as shown in Figure 37. Figure 48 shows the QE results, which are limited at 44%. By adding the SRH lifetime into modeling, the expected QE is 45% with a modeled lifetime of 630 ns. From the QE measurements, the flatness implies that there is no noticeable effect from surface recombination. It should be noted that the collection length seems relatively large. The model predicts a collection length of only about 10.6 μm, but the collection length obtained from these measurements is 29.4 μm.

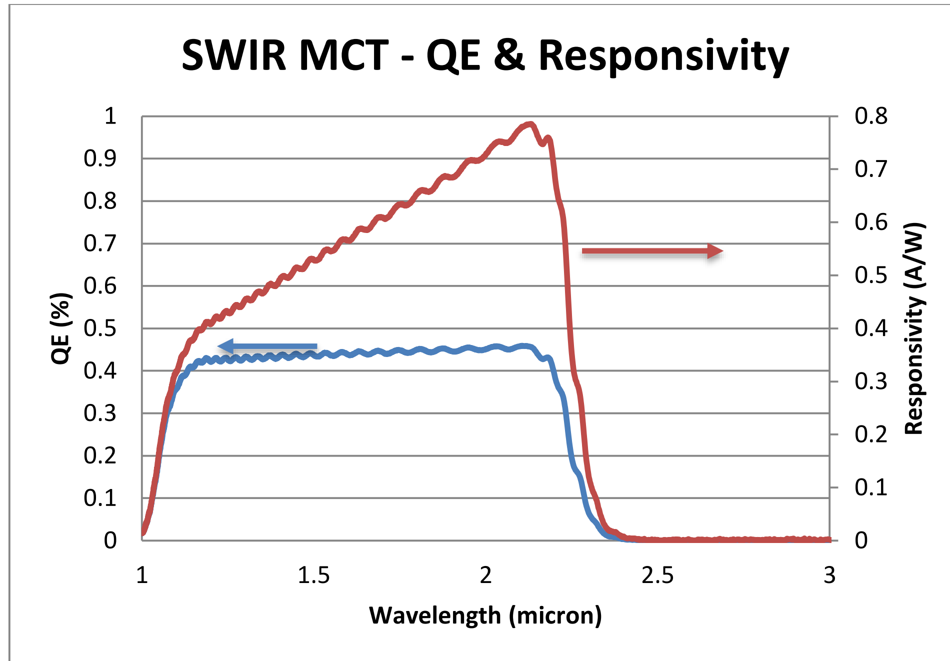


Figure 48. QE and Responsivity for 250µm diode

The zero-bias resistance-area product ($R_0A$) is another figure of merit used to determine performance of a device. There are two goals in determining the $R_0A$: i) compare to other devices, and ii) determine uniformity of the sample. In the experiments, it is found that the $R_0A$ product decreases as the size of the diode decreases due to the junction area being used in the calculation, $A = A_j$, as can be seen in Figure 49. This decrease is due to lateral collection. In large area diodes, the lateral collection length is small in relation to the junction radius, while in a small area diode, the junction radius is on the same order of magnitude as the collection length. To account for this, the optical area ($A = \pi\left(R_j + L_c\right)^2$) is used when calculating the $R_0A$ product. The addition of the collection length results in

the $R_0A$ being flat across all diode sizes. This shows good uniformity and acts as a confirmation with the collection length determined from QE, as seen in Figure 50. Also, the $R_0A$ product is near the $R_0A$ empirical value of 1,300 Ohm-cm$^2$ for SRH-limited MCT grown on CdZnTe.

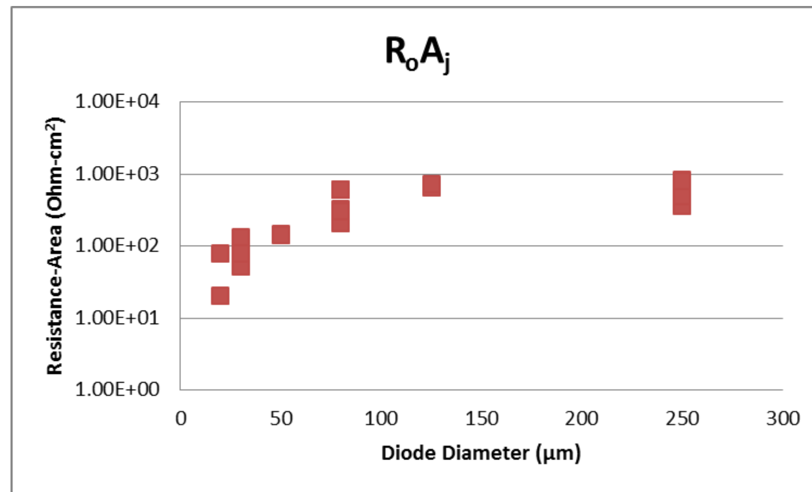


Figure 49. Zero-bias resistance-junction area product of various diameter circular diodes on MC0074

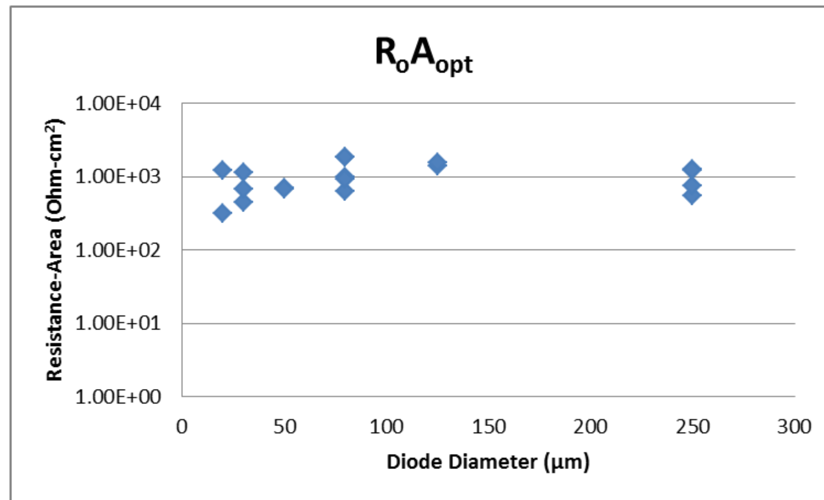


Figure 50. Zero-bias resistance-optical area product of various diameter circular diodes on MC0074

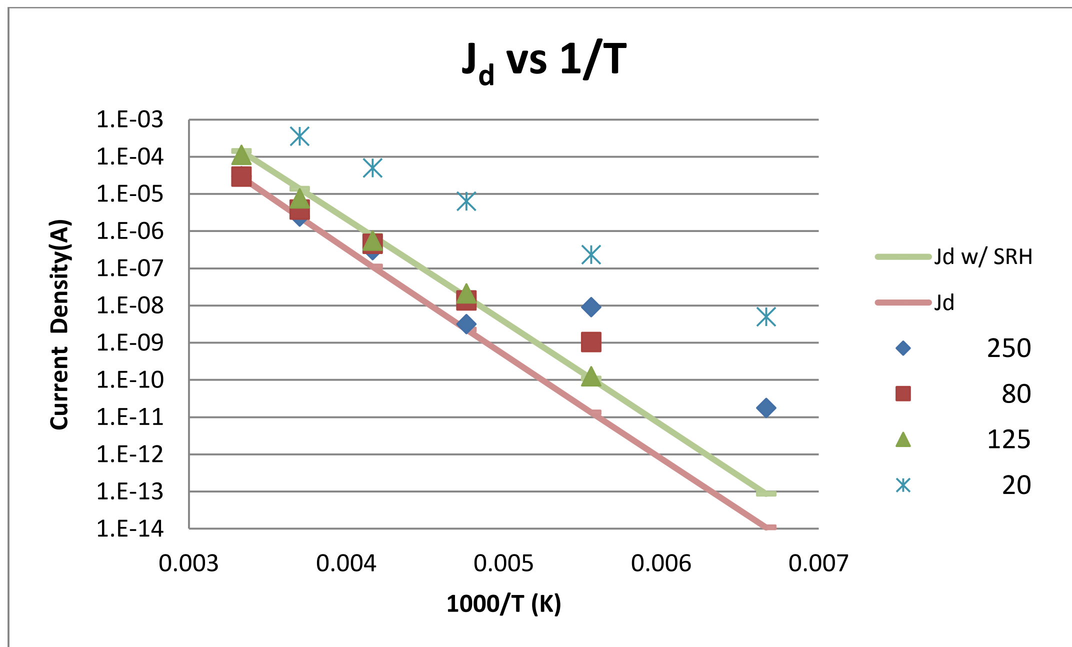


Figure 51. Dark current with representative theoretical currents of Diffusion with and without SRH affecting lifetime

The dark current density versus temperature sheds light on the limitations to optimal device performance. The current density tends to be linear with temperature down to approximately 210K where the current no longer exhibits diffusion limited performance. This shift is due to the domination of current by g-r. The other finding is that there is a significant issue when creating diodes at small diameters due to the occurrence of shunt current, as mentioned previously.

### *5. 5. Devices: Effect of TCA*

To determine the influence of TCA, samples of various compositions were subjected to TCA and fabricated alongside samples that were not treated with TCA. The TCA schedule applied was 128 60-second cycles between 350°C and 290°C. The basic analysis to determine the influence of dislocation-induced SRH centers within the bandgap involve looking at the dark current density at low reverse bias, as can be seen in Figure 52. Models with varying minority carrier lifetimes at varying temperatures are shown. Some diodes fit well with diffusion limited performance at a minority carrier lifetime of 100ns, which indicates that the devices are very much SRH limited, as the modeled non-SRH lifetime is 1.6 μs, or more than an order of magnitude lower dark current. This also indicates that, above 200K, the lifetime is limited by recombination centers in the quasi-neutral, absorber layer region. Due to loss during processing of the sister sample that was not subject to TCA processing and the unavailability of remaining material with the similar device characteristics, a direct comparison cannot be made.

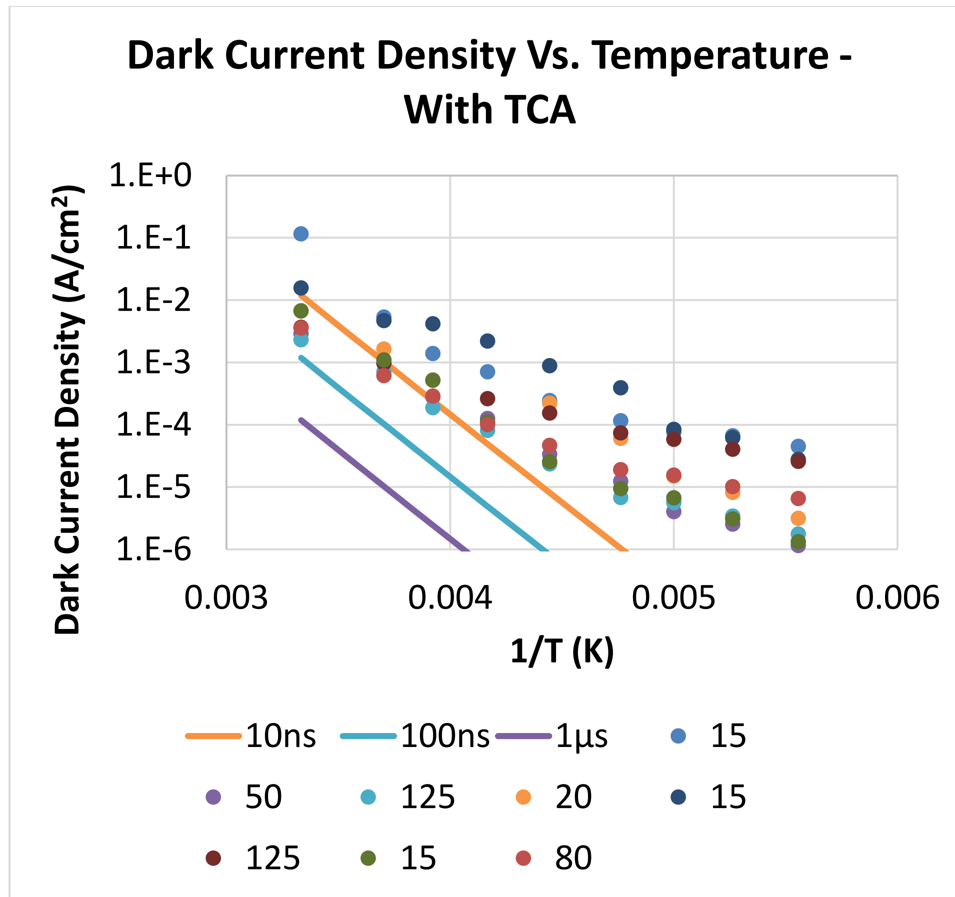


Figure 52. Dark Current Density vs. temperature for MC86, SWIR MCT layer subjected to TCA processing. Models are shown with their respective minority carrier lifetimes.

The $R_oA$ measurements, as compared to the theoretical model, are shown in Figure 53. The model $R_oA$ is 42 Ohm-cm$^2$ and the devices in this sample are quite limited. Also, QE measurements are very low, around 30%. The dislocation reduction to 1x10$^6$ cm$^{-2}$ does not sufficiently improve the device performance. It may be that the slight diffusion of the cap layer due to the TCA process may increase the depletion width, allowing greater g-r

current contributions. The limited performance may also be due to quartz contamination during the TCA process.

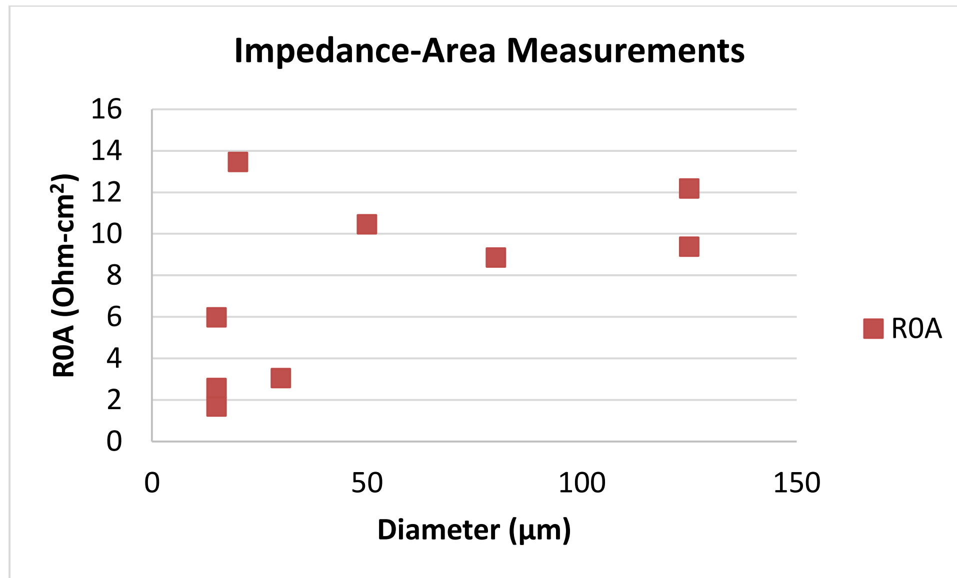


Figure 53. RoA measurements vs device diameter of MCT devices subjected to TCA.

## 5. 6. Comparison to the Competition

InGaAs is a well researched III-V material system that has similar performance to that of MCT at a 1.7 µm cutoff and is typically grown on lattice-matched InP substrates for this cutoff. The Ga composition is variable, which allows for a tunable bandgap. Increasing the cutoff is possible by modifying the molar fractions of indium and gallium to achieve up to 2.5 µm cutoff, but the significant shift away from the lattice matched substrate causes

substantial material defects that limit material quality and overall device performance. An InGaAs diode was obtained from T. Judson for comparison testing. For reference, the values obtained here are compared to published results, as well as the MCT diodes discussed previously [29].

The composition of eSWIR InGaAs for 2.59µm cutoff is x = 0.18 as determined by the bandgap given by the equation:

$$E_g(T = 300K) = 0.42 + .625x - (0.0001xT^2)\left(\left(\frac{5.8}{T + 300}\right) - \left(\frac{4.19}{T + 270}\right)\right) - \left(\frac{0.0001 * 4.19\, T^2}{T + 271}\right) + 0.475\mathrm{x}^2 \quad 5.32$$

Also, the intrinsic carrier concentration is given by:

$$n_i = \sqrt{N_c N_v} \exp\left(-\frac{E_g}{2k_B T}\right)$$
$$\cong 4.82 \cdot 10^{15}$$
$$\cdot \left[(0.41 - 0.09x)^{\frac{3}{2}} + (0.027 + 0.047x)^{\frac{3}{2}}\right]^{\frac{1}{2}}$$
$$\cdot (0.025 + 0.043x)^{\frac{3}{4}} \left[T^{\frac{3}{2}} \exp\left(-\frac{E_g}{4kT}\right)\right.$$
$$\left. \cdot \left(1 + \frac{3.75}{v} + \frac{3.28}{v^2} - \frac{2.46}{v^3}\right)^{\frac{1}{2}}\right] (cm^{-3}) \quad 5.33$$

In the fit of the g-r current density, the minority carrier lifetime is near 500ns, similar to the results previously obtained by Hoogeveen, et. al [29]. The influence of defects is quite significant in these devices as they are limited by both g-r current, at high temperature, and shunt current at lower temperatures, as seen in Figure 54. The influence of band-to-band tunneling in the diode is apparent from the bias dependent activation energy seen in Figure 55.

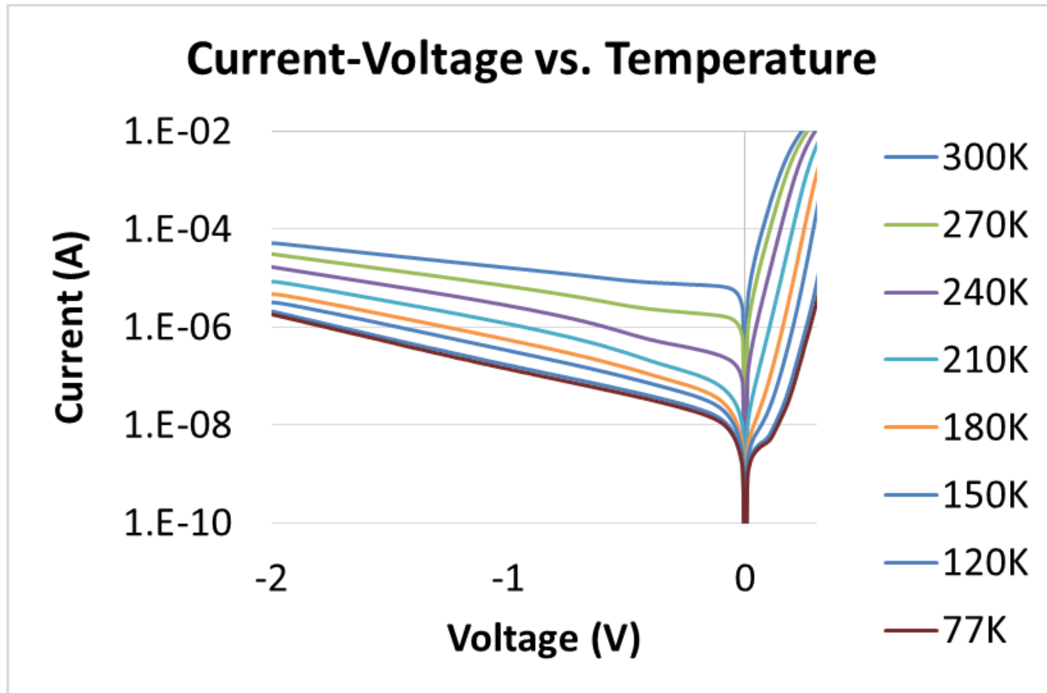


Figure 54. 1mm InGaAs diode dark current vs. temperature

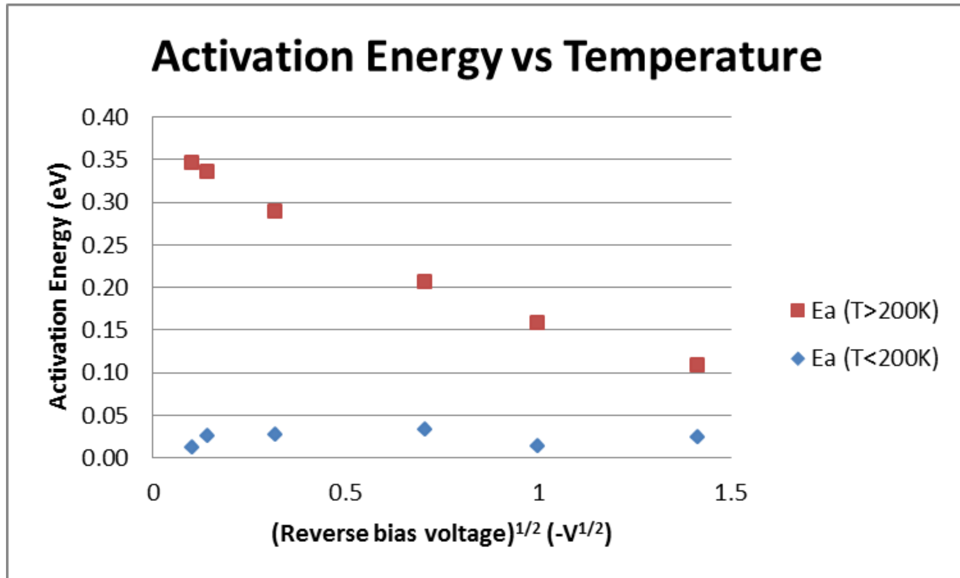


Figure 55. Activation energy for 1mm InGaAs diode above and below 200K

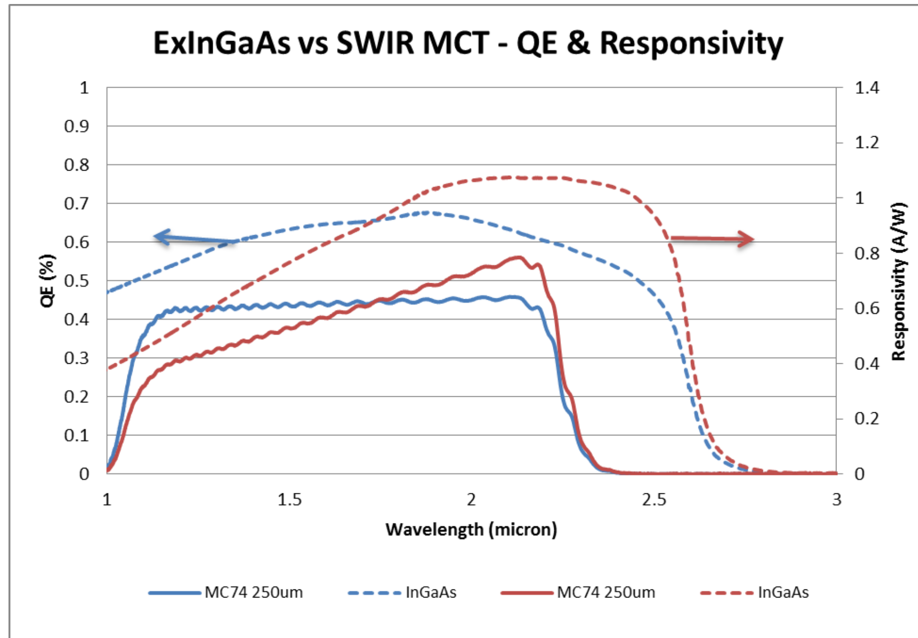


Figure 56. Comparison of extended InGaAs and MCT SWIR device QE and Responsivity

Spectral response in the 2.25 µm MCT material is limited by generation-recombination centers and measured to be only 44%. The quantum efficiency of the InGaAs sample is 66%. Figure 56 shows the spectral response with the quantum efficiency measured at 1.997 µm. The MCT sample has a very flat response vs wavelength, while the InGaAs sample has significant softening, as is expected when the cutoff is increased in InGaAs material. Softening of the peak corner is due to the sample being thin.

The maximum performance of InGaAs is limited by material defects, whereas, MCT without SRH limitations has a much higher intrinsic performance limit. The dark current of the InGaAs sensor is limited by band-to-band tunneling due to these material

defects. Without solving the material defects cause by lattice mismatch for a 2.5 μm cutoff InGaAs detector, the detector will not achieve higher performance.

## 5. 7. Application of Mesa Architecture

The impact of dislocations on device performance can be ascertained by designing a device structure whereby the mesa structure and planar structure devices can be measured on the same MCT layer. Standard device processing for planar materials uses metal pads for creating contacts to the diodes. Due to the sharp corner and high angle of the mesa bars, indium bump bonding is necessary to test mesa bar devices. New masks were fabricated to allow the simultaneous testing of planar and mesa bar devices.

The processing steps for the mesa bar devices includes the following: ICP etching, dislocation reduction annealing, arsenic ion implantation, activation and saturation annealing, passivation, metallization, and bump bonding to a fanout with indium bumps. The sample is etched to a depth of 8 microns, creating a region of 20 μm wide, long bar structures alongside a planar region. The layer is then annealed for 5 minutes at 400°C under a mercury atmosphere to induce dislocation reduction.

An example of the mesa device is shown in Figure 57. The variable temperature dark current density is shown in Figure 58. The sample fits to a dark current model with a minority carrier lifetime of 1.5 μs, or about half of the target value. Also, at lower temperatures, the dark current density of the mesa devices fits an Arrhenius equation with

an $E_g/2$ exponent. This indicates a very strong generation-recombination current at lower temperatures. Therefore the limitations to the performance of the mesa devices are not observed, as there may be other issues limiting the performance that are not observable in this sample.

The devices are tested at various temperatures to compare dark current performance, as seen in Figure 59. The notable result is the improved dark current at low reverse biases in the mesa device over the planar device. The dark current density for both planar and mesa devices is relatively equal at high temperatures, but as the temperature decreases, a shift in performance is observed. Due to minimized tunneling and shunt paths caused by dislocations, the dark current density, and thereby, the minimum noise in a sensor, is reduced by an order of magnitude at -100mV at 77K. Spectral response results are not attainable due to the formation of an internal ground loop of unknown source.

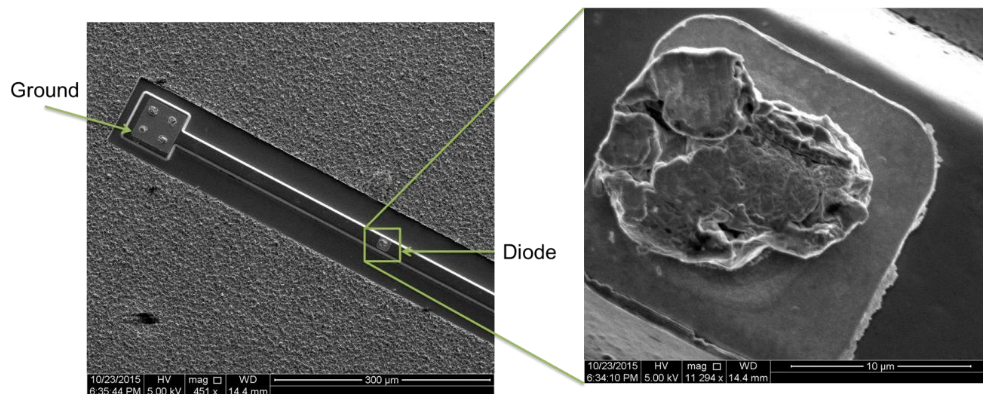


Figure 57. Left) Device structure of mesa devices. Right) Zoomed in image of mesa diode. Note that this photo was taken after bump bonding and removing the sample from the fanout.

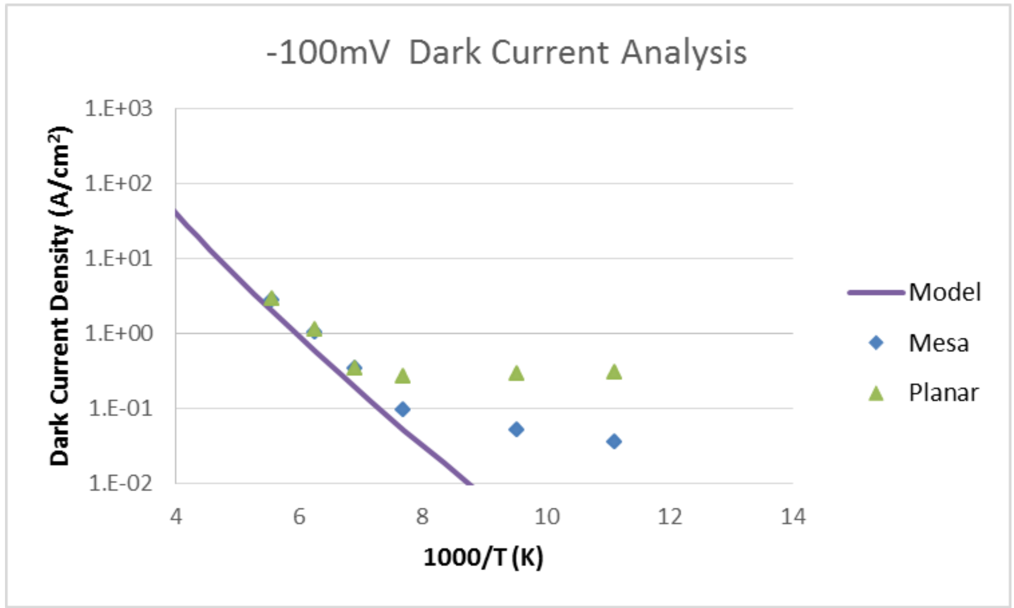


Figure 58. Dark current density comparison of mesa and planar devices under 100mV reverse bias conditions.

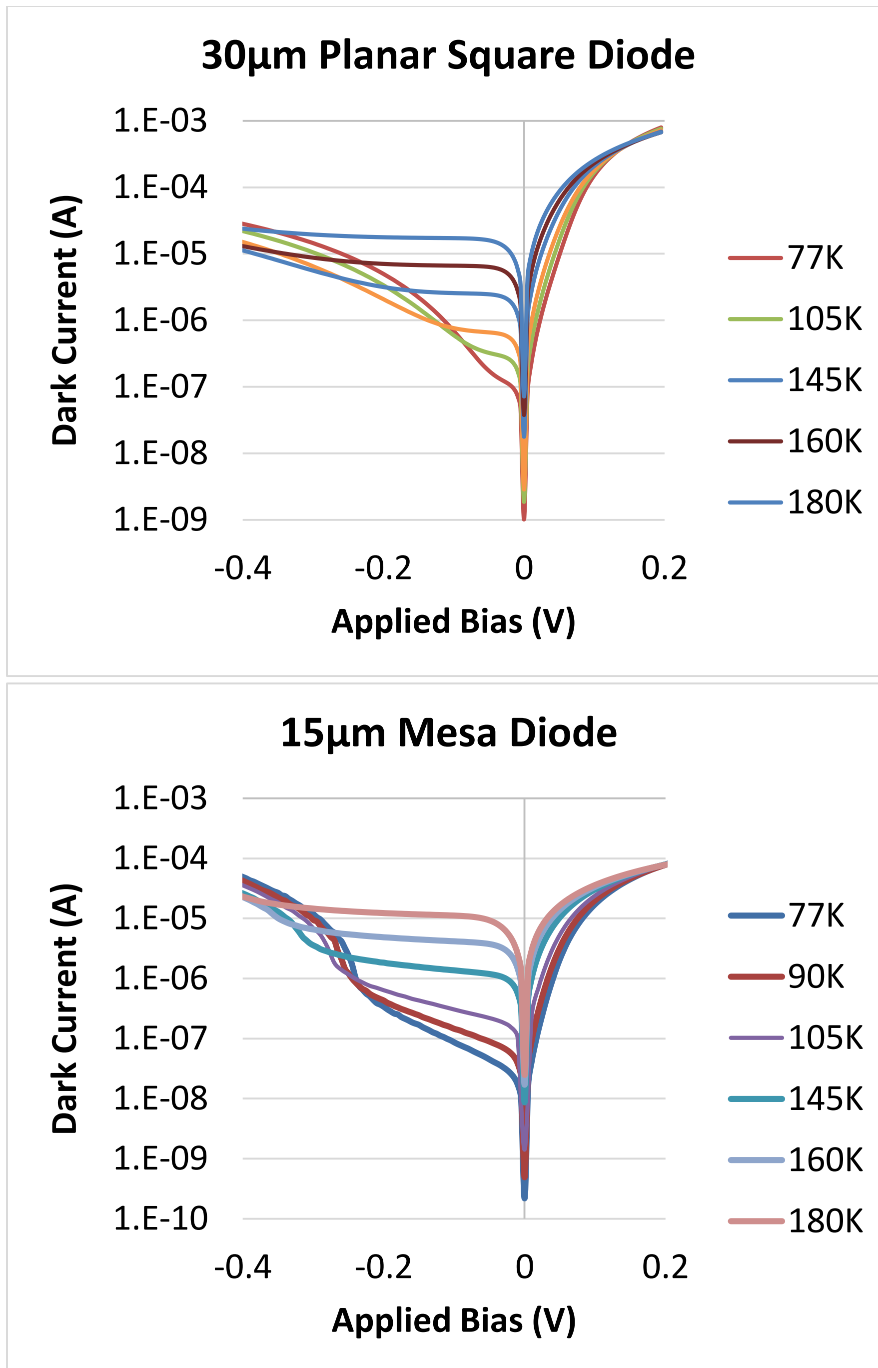


Figure 59. Dark currents of planar (top) and mesa (bottom) devices at varying temperatures.

## 5. 8. Device: Conclusion

Device performances of MCT diodes were characterized. SWIR planar MCT diodes were found to be limited by passivation interface currents. SWIR devices were limited in performance by a SRH recombination. Long wavelength, infrared MCT devices on mesa bars performed better than devices in planar areas. This can lead to the application of mesa structures for full array sensor fabrication and direct sensor performance comparison to MCT grown on the optimal CdZnTe substrates.

# Chapter 6. Conclusion & Future Work

In this work, dislocation reduction with TCA has been shown and direct application to devices has been tested. TCA was able to reduce dislocation densities in planar material down to $1 \times 10^6 \text{cm}^{-2}$ with 128 rapid cycles at the low anneal temperature of 350°C, but is unable to reduce the dislocation density further. It was also shown that diffusion after annealing at low temperatures is minimal with a less than 2% drop in Cd composition of the cap layer and minimal buffer layer diffusion.

The annealing of mesa structured MCT epilayers was able to reduce dislocation density in MCT below this limit with very short anneal time of 5 minutes and at a very low anneal temperature of 400°C. Mesa bars of 10 μm width exhibit the greatest dislocation reduction, having the lowest dislocation density of $1.5 \times 10^5\ cm^{-2}$, which is on par with MCT grown on CdZnTe substrates. The empirical model designed was accurate for the angle dependence and the mesa etched depth dependence.

SWIR MCT devices grown on Si-based substrates were fabricated using various annealing strategies. Standard processing was conducted on a SWIR sample with cutoff of 2.25 μm and resulted in shunt and generation-recombination current limited device performance. The application of mesa structures to long wavelength, infrared MCT devices

has shown significant promise. The dark current density of mesa bar devices is an order of magnitude less than planar devices at 100mV reverse bias at 77K.

Future work needs to look at many different areas. First and foremost, computer simulations of dislocation motion on atomic scales should be conducted to shed light on the mechanisms controlling dislocations in TCA and mesa structures. The device properties of SWIR MCT grown on CdTe/Si substrates are limited by SRH components. It has caused a reduced QE of 44%. Where the SRH components come from and how to remove them is necessary to advance the performance and achieve diffusion-limited performance. Finally, the work conducted on mesa bar devices should be applied to focal plane arrays and compared to MCT grown on CZT layers to determine the net effect on sensor level characteristics.

List of References

[1] G. Brill, Y. Chen, P. Wijewarnasuriya and N. Dhar, "Infrared Focal Plane Array Technology Utilizing HgCdTe/Si: Successes, Roadblocks, and Material Improvements," in *SPIE Infrared Systems and Photoelectric Technology IV*, Adelphi, MD, 2009.

[2] J. Benson, L. Bubulac, P. Smith, R. Jacobs, J. Markunaas, M. Jaime-Vasques, L. Almeida, A. Stoltz, J. Arias, G. Brill, Y. Chen, P. Wijewarnasuriya, S. Farrell and U. Lee, "Growth and analysis of HgCdTe on Alternate Substrates," *Journal of Electronic Materials,* vol. 41, no. 10, pp. 2971-2974, 2012.

[3] P. Capper, J. Garland, S. Kasap and A. Willoughby, Mercury Cadmium Telluride: Growth, Properties and Applications, Wiley Series in Materials for Electronic & Optoelectronic Applications, 2010.

[4] Y. Chen, S. Farrell, G. Brill, P. Wijewarnasuriya and N. Dhar, "Dislocation reduction in CdTe/Si by molecular beam epitaxy through in-situ annealing," *Journal of Crystal Growth,* vol. 310, no. 24, p. 5303–5307, 2008.

[5] S. Johnson, D. Rhiger, J. Rosbeck, J. Peterson, S. Taylor and M. Boyd, "Effect of dislocations on the electrical and optical properties of long-wavelength infrared HgCdTe photovoltaic detectors," *Journ. of Vac. Sci. and Tech. B,* vol. 10, no. 4, pp. 1499-1506, 1992.

[6] S. Farrell, G. Brill, Y. Chen, P. Wijewarnasuriya, M. V. Rao, N. Dhar and K. Harris, "Ex Situ Thermal Cycle Annealing of Molecular Beam Epitaxy Grown HgCdTe/Si Layers," *Journal of Electronic Materials,* 2009.

[7] S. Farrell, M. V. Rao, G. Brill, Y. Chen, P. Wijewarnasuriya, N. Dhar, D. Benson and K. Harris, "Effect of Cycle Annealing Parameters on Dislocation Density Reduction for HgCdTe on Si".

[8] A. Stoltz, J. Benson, M. Carmody, S. Farrell, P. Wijewarnasuriya, G. Brill, R. Jacobs and Y. Chen, "Reduction of Dislocation Density by Producing Novel Structures," *Journal of Electronic Materials,* vol. 41, no. 10, 2012.

[9] D. Hull and D. Bacon, Introduction to Dislocations, Woburn, MA: Butterworth and Heinemann, 1965.

[10] M. Berding, M. van Schilfgaarde and A. Sher, "First-principles calculation of native defect densities in Hg 0.8 Cd 0.2 Te," *Physical Review B,* vol. 50, no. 3, pp. 1519-1534, 1994.

[11] H. Vydyanath and C. H. Hiner, "Annealing Behavior of undoped HgCdTe epitaxial films at low temperatures," vol. 65, no. 8, 1989.

[12] D. Andrade, Artist, *Scheme of the Burgers' vector in edge and screw dislocations.* [Art]. 2008.

[13] J. Matthews and A. Blakeslee, "Defects in Epitaxial Multilayers. I. Misfit Dislocations," *Journal of Crystal Growth,* vol. 27, pp. 118-125, 1974.

[14] J. Hornstra, "Dislocations in the Diamond Lattice," *Journal of Physics and Chemistry of Solids,* vol. 5, no. 2, pp. 129-141, 1958.

[15] D. Holt, "Defects in the Sphalerite Structure," *Journal of Physics and Chemistry of Solids,* vol. 23, pp. 1353-1362, 1962.

[16] M. Carmody, D. Lee, Z. M., J. Phillips and J. Arias, "Threading and Misfit-Dislocation Motiont in Molecular-Beam-Epitaxy-Grown HgCdTe Epilayers," *Journal of Electronic Materials,* vol. 32, no. 7, 2003.

[17] M. Yamaguchi, M. Tachikawa, Y. Itoh, M. Sugo and S. Kondo, "Thermal annealing effects of defect reduction in GaAs on Si substrates," *Journal of Applied Physics,* vol. 68, no. 9, pp. 4518-4522, 1990.

[18] J. Benson, R. Smith, R. Jacobs, J. Markunas, M. Jaime-Vasquez, L. Almeida, A. Stoltz, L. Bubulac, M. Groenert, P. Wijewarnasuriya, G. Brill, Y. Chen and U. Lee, "Topography and Dislocations in (112)B HgCdTe/CdTe/Si," *Journal of Electronic Materials,* vol. 38, no. 8, pp. 1771-1775, 2009.

[19] J. Benson, S. Farrell, G. Brill, Y. Chen, P. Wijewarnasuriay, L. Bubulac, P. Smith, R. Jacobs, J. Markunas, M. Jaime-Vasquez, L. Almeida, A. Stoltz, U. Lee, M. Vilela, J. Peterson, S. Johnson, D. Lofgreen and D. Rhiger, "Dislocation Analysis in (112)B HgCdTe/CdTe/Si," vol. 40, no. 8, 2011.

[20] N. Bassim, M. E. Twigg, C. R. Eddy, J. C. Culbertson, M. A. Mastro, R. L. Henry, R. T. Holm, P. G. Neudeck, A. J. Trunek and J. A. Powell, "Lowered dislocation densities in uniform GaN layers grown on step-free (0001) 4H-SiC mesa surfaces," *Applied Physics Letters,* vol. 86, no. 2, 2005.

[21] X. Zhang, I. Rodriguez, P. Li, F. Jain and J. Ayersi, "A novel approach for the complete removal of threading dislocations from ZnSe on GaAs (001)," *Journal of Electronic Materials,* vol. 30, no. 6, pp. 667-672, 2001.

[22] T. Tezuka, N. Sugiyama and S. Takagi, "Dislocation-free relaxed SiGe-on-insulator mesa structures fabricated by high-temperature oxidation," *Journal of Applied Physics,* vol. 94, no. 12, 2003.

[23] A. Stoltz, J. Benson, M. Carmody, S. Farrell, P. Wijewarnasuriya, G. Brill, R. Jacobs and Y. Chen, "Reduction of Dislocation Density in HgCdTe on Si by Producing Highly Reticulated Structures," *Journal of Electronic Materials,* vol. 40, no. 8, pp. 1785-1789, 2011.

[24] S. Farrell, M. Rao, G. Brill, Y. Chen, P. Wijewarnasuriya, N. Dhar, J. Benson and K. Harris, "Comparison of the Schaake and Benson etches to Delineate Dislocations in HgCdTe layers," *Journal of Electronic Materials,* vol. 42, no. 11, pp. 3097-3102, 2013.

[25] M. Kinch, "Electronic Properties of HgCdTe," vol. 21, no. 215, 1982.

[26] C.-T. Sah, R. Noyce and W. Shockley, "Carrier Generation and recombination in P-N junctions and P-N junction characteristics," *Proceedings of the IRE,* vol. 45, no. 9, pp. 1228-1243, 1957.

[27] D. Rosenfeld and G. Bahir, "A model for the trap-assisted tunneling mechanism in diffused n-p and implanted n+-p HgCdTe photodiodes," *IEEE Transactions on Electron Devices,* vol. 39, no. 7, 1992.

[28] M. Reine, K. Maschhoff, S. Tobin, P. Norton, J. Mroczkowski and E. Krueger, "The impact of characterization techniques on HgCdTe infrared detector technology," vol. 8, no. 6S, 1993.

[29] R. Hoogeveen, R. J van der A and A. Goede, "Extended wavelength InGaAs infrared detector arrays on SCIAMACHY for space-based spectrometry of the Earth atmosphere," *Infrared Physics & Technology,* vol. 42, no. 1, pp. 1-16, 2001.

# Biography

Sina Simingalam graduated from Fairfax High School, Fairfax, Virginia, in 2006. He received his Bachelor of Sciences from George Mason University in 2010. He was employed as a graduate research assistant at George Mason University and received his Masters of Science from George Mason University in 2012.